Multiphoton Microscopy and Interaction of Intense Light Pulses with Polymers

by

Jean-Michel Guay

Thesis submitted to the
Faculty of Graduate and Postdoctoral Studies
In partial fulfillment of the requirements
For the M.Sc. degree in
Physics

Sciences
University of Ottawa

Abstract

The nanoscale manipulation of soft-matter, such as biological tissues, in its native environment has promising applications in medicine to correct for defects (eg. eye cataracts) or to destroy malignant regions (eg. cancerous tumours). To achieve this we need the ability to first image and then do precise ablation with sub-micron resolution with the same setup. For this purpose, we designed and built a multiphoton microscope and tested it on goldfish gills and bovine cells. We then studied light-matter interaction on a hard polymer (PMMA) because the nature of ablation of soft-matter in its native environment is complex and not well understood. Ablation and modification thresholds for successive laser shots were obtained. The ablation craters revealed 3D nanostructures and polarization dependent orientation. The interaction also induced localized porosity in PMMA that can be controlled.

Acknowledgements

Je voudrais spécialement remercier mes parents qui, pendant mes sept années passées à l'université, m'ont donnée le support dont j'avais besoin pour réussir dans mes études. Merci sincèrement pour vos encouragements. Une pensée spéciale a ma Loulou ma meilleure amie, ma confidente et ma fidèle compagne qui m'a accompagnée pendant toutes ces années.

I would like to thank Dr. Ravi Bhardwaj for giving me the opportunity to show my true potential making me grow in the field of physics and as a researcher.

I would also like to thank Mike Wong and Dr. Jean-Paul Brighta for their help and support throughout my thesis; always having the patience to answer my numerous questions.

I would also like to thank Farhana Baset, my research partner, and Dr. Ana Villafranca for their help and their valuable input throughout the dielectric studies.

The successful completion of the multiphoton microscope would not have been possible without the support of many individuals in the years of my master's. Dr. Quoc-Thang Nguyen, Kleinfield's labs, who provided the software to control the components of the multiphoton microscope and enable the 3D reconstruction of the biological tissues. Villie and Dr. Steve Perry, University of Ottawa Biology department, who provided crucial support and a constant supply of goldfish gills to test the multiphoton microscope. Dr. Andrew Pelling and Dr. Zeinab Al, University of Ottawa Physics department, for their support in providing usefull information and samples to test the microscope as well as letting me used their confocal microscope.

The study of dielectrics would not have been possible without the support of the Science machine shop who provided a constant supply of PMMA samples, and a special thanks to Dr. Arnaud Weck for letting me use his SEM to analyse the results of the experiments.

Contents

1 Introduction to Multiphoton Processes **1**

1.1 Motivation 1
1.2 Background 2
1.3 Multiphoton Excitation 3
1.4 Cross-Sections 8
1.5 Localized Energy Deposition and Pulse Duration Effects 9
1.6 N-photon Fluorescence 12
1.7 Dependence of N-photon Fluorescence on Dye Concentration 14
1.7.1 Special Case of N-photon Fluorescence: Two-Photon Microscopy . 16
1.8 Confocal Microscopy 16
1.8.1 Confocal Microscopy versus Two-Photon Microscopy 18
1.9 Photoionization 21
1.9.1 Multiphoton Ionization (MPI) 22
1.9.2 Tunnel Ionization 22
1.9.3 Impact Ionization 23
1.9.4 Shot-to-Shot Memory 24
1.10 Ablation 28
1.10.1 Laser Ablation of Soft-Matter in a Water Environment 29
1.10.2 Internal Modification 35

2 Two-Photon Microscopy:Basic Principles, Performance and Advantages 39

2.1 Introduction 39
2.2 Two-Photon Excitation Process: imaging biological specimens 39
2.3 Resolution 41
2.3.1 Point Spread Function 42
2.3.2 Optical Sectioning 46

2.3.3 Refractive Index Mismatching . . . 47
2.3.4 Effects of Group Velocity Dispersion . . . 49
2.3.5 Chromatic Aberration . . . 51
2.4 Advantages of TPM . . . 53
2.4.1 Scattering . . . 53
2.4.2 Photodamage . . . 54
2.4.3 Simultaneous Excitation of Multiple Dyes . . . 55
2.4.4 Ablation and Thermal Damage . . . 56

3 Two-Photon Microscopy:Design and Implementation 57
3.1 Introduction . . . 57
3.2 Laser System . . . 58
3.3 Experimental Setup . . . 58
3.4 Optical Design of the Multiphoton Microscope . . . 60
3.4.1 Scanning System . . . 61
3.4.2 Keplerian Telescope and Beam Expansion . . . 62
3.4.3 Microscope Objectives . . . 65
3.4.4 Dichroic Mirror . . . 67
3.4.5 Detection System . . . 68
3.5 Mechanical Design . . . 70
3.5.1 Photomultiplier Tube and Pre-Amp . . . 71
3.5.2 Scanners Servo Driver . . . 71
3.5.3 Z-stage Integration . . . 72
3.5.4 Shutter . . . 72
3.5.5 Data Acquisition and Communication . . . 72
3.6 MPScope . . . 73
3.6.1 Mirror deflection angle . . . 74
3.6.2 Image duplication and pixel offset . . . 74

4 Two-Photon Microscope: Results and Comparaison 76
4.1 Introduction . . . 76
4.2 Experimental . . . 77
4.2.1 Pulse Duration . . . 77
4.2.2 Systems evaluation and performance . . . 79
4.3 Results . . . 83
4.3.1 Goldfish (*Carassius auratus*) . . . 83

4.3.2 Bovine Pulmonary Artery Endothelial cells 96
4.4 Conclusion and Future Work 101

5 Dielectrics Studies **102**
5.1 Introduction 102
5.2 Laser System 103
5.3 Experimental Setup 104
5.3.1 Autocorrelator and pulse duration 106
5.3.2 Energy deposition and focus properties 108
5.4 Results: Polymer Studies 110
5.4.1 Line Ablation(PMMA) 110
5.4.2 Single Shot Ablation (PMMA) 112
5.5 Internal modification of PMMA 136
5.5.1 Refractive index change and waveguide creation 136
5.5.2 Intraocular lenses 138

6 Conclusion and Future Work **142**
6.1 Conclusion 142
6.2 Future Work 145

A Glossary of Terms **147**

List of Figures

1.1 Schematic of multiphoton excitation processes. In atoms, (top, left) via intermediate states (unallowed 1-photon transitions) exciting the system from i (the ground state) to f (the excited state). In molecules, (top, right) via real-resonance (allowed 1-photon transitions) through different electronic states and vibrational levels of the molecule. (bottom) Dressed states of a molecule showing different potential energy curves shifted up and down in energy by 1 photon leading to curve crossing. The dashed lines represent the diabatic potential curve and the solid lines the adiabatic potential curves. 4

1.2 Schematic of multiphoton excitation and subsequent release of a lower energy photon due to thermal relaxation 8

1.3 Excitation volume of confocal versus two-photon microscopy 11

1.4 Principle of Confocal Imaging 17

1.5 Optical sectioning and 3D reconstruction of a sphere 18

1.6 Photobleaching 19

1.7 Multiphoton ionization via the absorption of n-photons 22

1.8 Schematic of tunnel ionization and ionization of Xenon in the presence of an intense laser field. 23

1.9 Shot-to-shot memory inside fused silica glass 25

1.10 Comparing the transmission of a fresh fused silica sample to a previously exposed sample as a function of laser shots 26

1.11 Determining the cross-section and ionization threshold of previously exposed sample of fused silica glass compared to a fresh one 27

1.12 Observation of green fluorescence from the laser-modified regions in PMMA due to bond scissions 28

1.13 Ablation of steel using nanosecond and femtosecond pulses 29

1.14 Optical breakdown in distilled water for different pulse durations 33

1.15 Optical breakdown in water; the dependence of plasma transmission on pulse duration . . . 34
1.16 The conversion of energy into cavitation energy for different pulse durations 35
1.17 Fluorescent emissions from the modified regions inside PMMA . . . 36
1.18 Refractive index modification inside PMMA . . . 37
1.19 Formation of periodic nano-planes inside fused silica glass . . . 38

2.1 Schematic of a two-photon excitation and the release of a Stokes-shifted photon due to thermal relaxation . . . 40
2.2 The confinement of the interaction region, in TPM, due to the quadratic dependance on intensity. . . . 41
2.3 (left) Rayleigh criterion where two points are still distinguishable; (center,right) cases where points are no longer distinguishable. . . . 42
2.4 Intensity distribution for both the lateral and axial direction in conventional, two-photon, and confocal microscopy. . . . 43
2.5 Single optical section and 3D reconstruction of a tissue sample . . . 47
2.6 Effects of refractive index mismatch . . . 48
2.7 Comparing the broadening of the intensity distribution of an oil and water-dip objective when imaging thick biological tissues . . . 49
2.8 Image quality and performance of a two-photon microscope with and without pre-chirping the pulse . . . 51
2.9 Chromatic Aberrations . . . 52
2.10 Vignetting . . . 52
2.11 Photodamage per scan in function of laser power and pulse width . . . 55

3.1 Multiphoton microscope: breadboard setup . . . 58
3.2 The Multiphoton Microscope . . . 60
3.3 The Keplerian Telescope . . . 63
3.4 Design parameters of the Keplerian Telescope . . . 63
3.5 Lens distance selection for the Keplerian Telescope . . . 65
3.6 Optical setup to correct for chromatic aberration and vignetting . . . 69
3.7 Mechanical schematic of the multiphoton microscope setup . . . 70
3.8 MPScope: image duplication . . . 74
3.9 MPScope: lag Correction . . . 75

4.1 Images of filamental nerve fibres of a goldfish gill obtained with the multiphoton microscope . . . 83
4.2 Images of goldfish gills acclimated to 7°C; projection of multiple optical layers of the gill with a combined thickness of 235 μ m . . . 84
4.3 Images of goldfish gills acclimated to 7°C; view of the physiology of the gill and close up view of the lamellar neuroepithelial cells . . . 85
4.4 Images of goldfish gills acclimated to 7°C positioned on its side . . . 86
4.5 Images of goldfish gills acclimated to 7°C; close up view of the neuroepithelial cells . . . 87
4.6 Images of goldfish gills acclimated to 7°C . . . 88
4.7 Images of goldfish gills acclimated to 7°C . . . 89
4.8 Simultaneous excitation of multiple dyes tagged to a goldfish gill . . . 91
4.9 Images of goldfish gills acclimated to 7°C; projected and filtered using ImageJ . . . 92
4.10 Confocal microscope images of a goldfill gill acclimated to 7°C . . . 93
4.11 Comparing images of a goldfish gill acclimated to 7°C obtained by a confocal microscope to those obtained by our multiphoton microscope design 95
4.12 Bovine Pulmonary Artery Endothelial cells . . . 96
4.13 Bovine Pulmonary Artery Endothelial cells . . . 97
4.14 Images of Bovine Pulmonary Artery Endothelial cells . . . 98
4.15 Bovine Pulmonary Artery Endothelial cells network . . . 99
4.16 Images of Bovine Pulmonary Artery Endothelial cells . . . 100

5.1 Experimental Setup: optical table and dielectric setups . . . 104
5.2 Photodiode calibration . . . 105
5.3 PMMA polymer structure . . . 110
5.4 Surface line ablation of PMMA . . . 111
5.5 Graph: Threshold fluence versus number of shots per micron . . . 112
5.6 Measurement of the modified regions . . . 114
5.7 Ablation craters resulting from two and five laser shots . . . 114
5.8 Graphs: D^2 versus $\ln(E_{pulse})$ for 2 and 5 laser shots . . . 115
5.9 Size of ablation craters depending on pulse energy with respect to ablation threshold . . . 116
5.10 Size of ablation craters depending on pulse energy with respect to ablation threshold . . . 117

5.11 Graph: Fluence at threshold versus the number of shots 118
5.12 SEM pictures of the ablation craters at thershold for 1, 2, and 5 laser shot ablation of PMMA 118
5.13 1 shot experiment; ablation craters caused by the use of different light polarizations. With energy of 1.33 μJ 120
5.14 1 shot experiment; ablation craters caused by the use of different light polarizations. With energy of 4.35 μJ 121
5.15 1 shot experiment; ablation craters caused by the use of different light polarizations. With energy of 7.25 μJ 122
5.16 5 shot experiment; ablation craters caused by the use of different light polarizations. With energy of 1.33 μJ 123
5.17 5 shot experiment; ablation craters caused by the use of different light polarizations. With energy of 4.35 μJ 124
5.18 5 shot experiment; ablation craters caused by the use of different light polarizations. With energy of 7.25 μJ 125
5.19 Dependence of structures on the number of laser shots delivered (using linearly polarized light) 126
5.20 Dependence of structures on the number of laser shots delivered (using circularly polarized light) 127
5.21 Dependence of structures on the number of shots delivered (using elliptically polarized light) 128
5.22 Side view of an ablation crater caused by linearly polarized light 129
5.23 Results suggesting a prefered direction to the photoionization of PMMA along the electric field of the laser 130
5.24 Wave-patterns due to preferred direction of photoionization 132
5.25 Formation of periodic structures 133
5.26 Periodic structures found within the ablation craters. Seperated by an average distance of 1 μm. 134
5.27 Ablation craters made by linearly polarized light rotated to make a 45° angle with the motion of the stage 135
5.28 Periodic structures found within the ablation craters, using the same orientation but different stage speed, intensity and pulse duration. 136
5.29 Waveguides formed within a PMMA sample 137
5.30 Graph: Threshold energy versus number of shots per micron 138
5.31 Surface line ablation of contact lenses 140

5.32 Surface line ablation; melting of the contact lens 140

6.1 Graph: (Surface line ablation) Threshold fluence versus number of shots per micron 142
6.2 Graph: (Single shot ablation) Threshold fluence versus number of shots . 143
6.3 Graph: (Waveguides) Threshold energy versus number of shots per micron 143
6.4 Graph of threshold values for single shot and surface line ablation of PMMA versus number of shots delivered to the region 145

Chapter 1

Introduction to Multiphoton Processes

1.1 Motivation

Cancer and other degenerative diseases are causing high mortality rates around the world and statistics show an augmentation every year in newly affected individuals. Therefore, finding new ways of curing cancer and treating these diseases is of crucial importance. The key to understanding and treating these ailments could lie in an imaging tool capable of studying live cells within their native environment (*In vivo*) and permitting the manipulation of biological systems on nanometer dimensions by light-matter interactions. One such tool is the multiphoton microscope which employs ultrashort laser pulses to give it the ability to do both imaging and nano-ablation with minimal collateral damage to the surrounding regions.

For this reason, I have designed, built and tested a multiphoton microscope capable of imaging biological tissues with sub-cellular resolution and with the ability to perform precise ablation with micron precision. However, howing to the complex nature of light-matter interaction and the optical breakdown of soft-matter in its native environment. The study of light-matter interaction (i.e. ablation and refractive index change) was first conducted on harder polymers (PMMA) with the vision of gradually making the transition towards softer polymers (intraocular lenses) in their native environment.

1.2 Background

Today's understanding of light-matter interactions was pioneered by Albert Einstein in 1905, whose explanation of the photoelectric effect [1] merited him the Nobel Prize in 1921. The photoelectric effect was first discovered by studying the interaction of light with metals. It was observed that when light was incident upon a metal, there was a transfer of energy to the metal's electrons, thus inducing a current. This current was observed to only be present for certain colors of light, indicating the presence of an energy threshold (or angular frequency) needed for the release of electrons. This led to the conclusion that the electrons would not be released unless the energy transferred ($\hbar\omega$) to them from the incoming photons exceeded that of a work function, ϕ_w (bandgap width), which bided the electrons to the metal ($\hbar\omega > e\phi_w$). In the same paper, Einstein explained that the energy transferred to the electrons would remain the same (keeping the same frequency) even with increasing light intensity. This concept introduced the particle-wave properties of light and the release of photoelectrons by the interaction of light with matter. Einstein's proposal held true for the next 60 years until the introduction of lasers capable of producing ultrashort pulses, giving birth to the field of nonlinear optics. In nonlinear optics, the response of the material to light depends in a nonlinear manner on the strength of the light's electric field. Laser pulses whose photons had considerably less energy than the bandgap were observed to promote electrons into the conduction band, inducing a current. The interaction of a single photon would be inadequate to exceed the material's work function but it was the simultanous interaction of multiple photons with the material that challenged Einstein's theory. This led to the theory of multiphoton ionization.

Multiphoton ionization (or excitation), is a consequence of a quasi-simultaneous absorption of multiple photons in a single event. The concept that more than one photon could be absorbed in a single quantum event was first introduced in the doctoral dissertation of Nobel recipient, Maria Goppert-Mayer [2], in 1931. It was hypothesized that an atom or a molecule could simultaneously absorb two photons in the same quantum event if both photons arrived within a certain time window. This statement could not be verified until the invention of the first pulsed laser by Maiman in 1960 [3]. Kaiser and Garrett confirmed Goppert-Mayer's hypothesis experimentally in 1961 when they reported a 2-photon excitation and fluorescence from $CaF_2 : Eu^{2+}$ [4]. The concept was later generalized into an n-photon excitation (or ionization) of atoms or molecules. The time window in which two photons must interact with a molecule in order to achieve

simultaneous absorption was found to be 10^{-16} s [5], which is the timescale of molecular energy fluctuations determined by Heisenberg's uncertainty principle.

1.3 Multiphoton Excitation

Multiphoton excitation of an atom or a molecule is achieved by exciting the system from the ground state to the excited state by the absorption of more than 1 photon [6]. In the case of atoms, the multiphoton excitation process (i.e. using sub-bandgap photons) is done via a series of intermediate states (see figure 1.1). As in most atoms, the energy gap between the ground and excited state is generally greater than the typical photon energy emitted by ultrafast lasers. Hence, the intermediate states, through which the multiphoton interaction occurs, are not eigenstates of the system and are therefore called virtual states. For molecules, the multiphoton excitation process is a lot more complex. The multiphoton transitions can proceed via intermediate states that are virtual (unallowed 1-photon transitions) or through a superposition of molecular states that are in resonance (allowed 1-photon transitions), as shown in Figure 1.1. At higher intensities, light dressed states of the molecule results in potential surfaces shifted up and down by 1 photon energy. This Floquet picture of light-molecule interaction gives rise to curve crossings as shown in Figure 1.1.

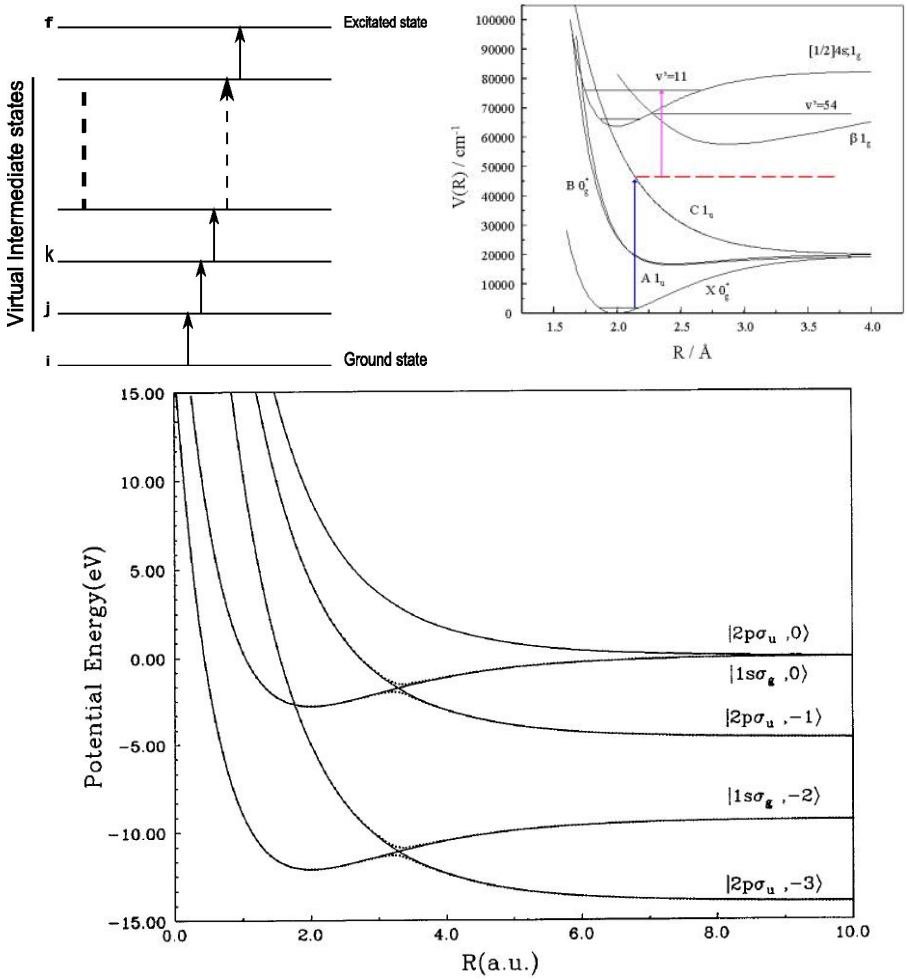

Figure 1.1: Schematic of multiphoton excitation processes. In atoms, (top, left) via intermediate states (unallowed 1-photon transitions) exciting the system from i (the ground state) to f (the excited state). In molecules, (top, right) via real-resonance (allowed 1-photon transitions) through different electronic states and vibrational levels of the molecule. (bottom) Dressed states of a molecule showing different potential energy curves shifted up and down in energy by 1 photon leading to curve crossing. The dashed lines represent the diabatic potential curve and the solid lines the adiabatic potential curves.

The Floquet picture is based on Floquet theorem in differential equations with periodic coefficients. The Hamiltonian of a system interacting with the light can be written

as

$$H = \sum_i \frac{1}{2m_i}(p_i - \frac{z_i}{c}A(r_i,t))^2 + V(r_i) \tag{1.1}$$

Where A is the vector potential of the electro-magnetic field, r_i is the position of the ith particle, m_i is the mass, p_i is the momentum of the ith particle and, z_i is the charge. With A periodic in time as $A(\mathrm{t} + \mathrm{T}) = A(\mathrm{t})$.

Because the laser field is periodic in time

$$H(t+T) = H(t) \tag{1.2}$$

Floquet theorem guarantees that any solution $\Psi(r,t)$ of the Shrödinger equation with above periodic Hamiltonian

$$i\hbar\frac{\partial}{\partial t}\Psi_i(r_i,t) = H(t)\Psi(r_i,t) \tag{1.3}$$

can be written as

$$\Psi(r_i,t) = e^{\frac{-iEt}{\hbar}}\phi(r_i,t) \tag{1.4}$$

Where ϕ has the same time periodicity as H (i.e. $\phi(r_i, t+T) = \phi(r_i,t)$). Therefore equation 1.4 can be expressed in a Fourier series

$$\Psi(r_i,t) = e^{\frac{-iEt}{\hbar}} \sum_{n=-\infty}^{\infty} e^{in\omega t}\phi_n(r_i) \tag{1.5}$$

Where ω is the laser frequency and integer n can be regarded as the number of photons absorbed from (or emitted in) the laser field.

For the excitation of atoms (or molecules) via virtual states, the number of virtual states accessed during the excitation depends on numerous factors such as: the bandgap energy, the intensity of the laser delivered to the interaction region, the material's **cross-section**, and the incident photon energy [6]. It is to be mentioned that the multiphoton process of exciting atoms and molecules through such states is not trivial and can not be obtained with all light sources.

In traditional quantum mechanics the treatment of such a multiphoton process dictates that the photons must be simultaneously absorbed since the virtual states are not proper eigenstates of the states, hence can not exist, and therefore have no lifetime associated to them. However, the time-energy uncertainty relation allows such states, that are not

properly energy conserving, to exist for a short period of time [7]. Hence, from the Heisenberg uncertainty principle and with a photon energy of 1.55 eV, the lifetime of the virtual states are approximated to be of $\approx 2.67\times10^{-15}$ s. Obtained from the time-energy uncertainty relation

$$\Delta E \Delta t \approx \hbar \tag{1.6}$$

Where ΔE is the energy fluctuation associated to the virtual state, Δt is the lifetime of the virtual state and $\hbar$ Planck's constant.

It is during the lifetime of the virtual state that another photon must arrive and be absorbed in order to push the electron into the excited state or to photoionize or to simply access another virtual state (where other photons will have to be absorbed in order to complete the process). Otherwise, the system falls back to the ground state and releases the excess energy through heat or other mechanisms. For this reason, multiphoton processes requires high intensities, within the interaction region, that are only achievable using pulsed lasers. The intensity required for multiphoton excitation of an hydrogon atom can be easily estimated. The lifetime associated to a virtual intermediate state, using a sub-bandgap photon energy of 1.55 eV, of $\approx 2.67\times10^{-15}$ s. For successive absorption of photons within this time, there should be more than 10^{15} photons per second incident on the atom with dimensions of an angstrom (10^{-8} cm). Therefore, the flux necessary for a multiphoton excitation is approximated to be of 10^{31} eV/s/cm^2. For a photon energy of 1.55 eV this corresponds to an intensity of 10^{13} W/cm^2. More rigorous calculation and experiments suggest an intensity of 6×10^{13} W/cm^2 to ionize hydrogen [8].

The process of multiphoton excitation can therefore be visualized as the absorption of n photons with frequency ω, resulting in either the release of a $\approx n\hbar\omega$ photon (fluorescence) (see Figure 1.2), or an electron into the continuum (photoionization) (see Figure 1.7) or to an excited state.

In my research, both multiphoton excitation and multiphoton ionization processes are used. The former is linked to the excitation of dye molecules and their subsequent emission of light as the system returns to the ground state (see Figure 1.2). The latter occurs when the total energy from the multiphoton interaction is greater than that of the bandgap energy, leading to photoionization (see Figure 1.7 and Section 1.9).

In the first case (i.e. multiphoton excitation, Figure 1.2), n photons of frequency ω are absorbed to meet the energy bandgap between the ground state and the excited state. The intensity is low enough to prevent the photoionization of the electron. This is shown by

$$(E_1 - E_0) \geq hc(1/\lambda_1 + 1/\lambda_2 + ... + 1/\lambda_n) \tag{1.7}$$

where E_1 is the excited state, E_0 is the ground state, c is the speed of light, h is Planck's constant, and $\lambda_1 ... \lambda_n$ are the wavelengths of light taking part in the multiphoton excitation process. Since pulsed lasers produce, by definition, pulses of light with a certain bandwidth of frequencies, the photons, in principle, do not necessarily have to be identical. For practical reasons, the wavelengths taking part in the excitation process will be taken as equal.
Hence equation 1.7 becomes

$$(E_1 - E_0) \geq \frac{nhc}{\lambda} \tag{1.8}$$

where λ is the central wavelength of the laser.

It is important to mention here that the excited state in which the electron is located (refer to Figure 1.2) prior to releasing a photon is an eigenstate of the molecule (or atom). The emitted photons may not have exactly an energy equal to nω due to the thermal relaxation of the system when in the excited state, as shown in Figure 1.2 [6, 9, 10].
Thermal relaxation, in molecules, occurs when the excess vibrational energy is transferred to the surrounding molecules by the means of collisions. In other words, following the excitation of the molecule there is a process of vibrational relaxation, within the electronic state of the molecule, from an higher vibrational level towards the lowest vibrational level (see Figure 1.2). Resulting in the release of a Stokes shifted photon (i.e. a photon of lower energy).

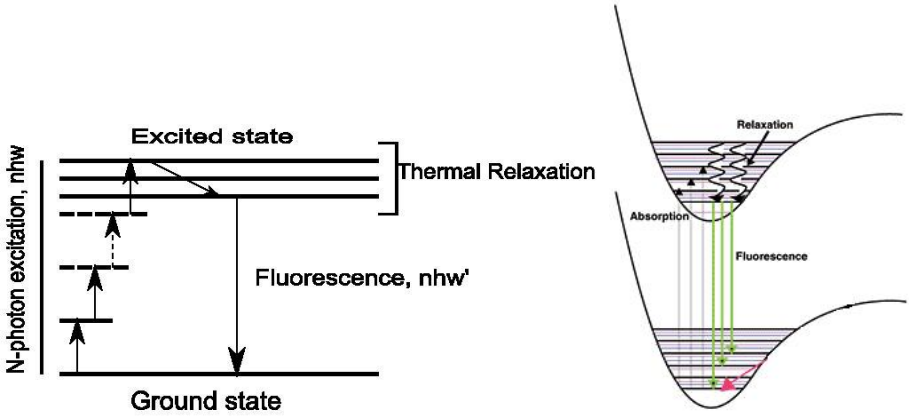

Figure 1.2: Schematic of multiphoton excitation via (left) intermediate states and (right) real-resonance resulting in the release of a photon of lower energy that may not be equal to nω due to the thermal relaxation.

In the second case (i.e. multiphoton ionization), n photons of frequency ω are simulaneously absorbed but with a total energy higher then the ionization potential (IP), resulting in the ejection of the electron into the continuum (see Figure 1.7).

$$(E_1 - E_0) < \frac{nhc}{\lambda} \tag{1.9}$$

The difference between these two scenarios is the intensity. With higher intensities, there is a much higher photon flux delivered to the region and more photons can be absorbed quasi-simultaneously so that the total combined energy can exceed that of the IP. The absorption of multiple photons in a single quantum event is not only intensity dependant but also strongly depends on the cross-sections of the molecule or atom interacting with the field [6].

1.4 Cross-Sections

The cross-section for a 2-photon excitation was estimated by Chris Xu [6, 11, 12] using a time-dependent semiclassical interaction approach. He estimated this excitation cross-section using only the lowest-order dipole transition.
The 2-photon cross-section, σ_2, can be estimated by:

$$\sigma_2 = \sigma_{ij}\sigma_{jk}\tau_j \tag{1.10}$$

Where σ_{ij} and σ_{jk} are the 1-photon absorption cross-sections and τ_j is the lifetime of the virtual intermediate state. Xu estimated τ_j to be of about $10^{-15} - 10^{-16}$ s using the transition frequency to the intermediate state and the frequency of the absorbed photon. σ_{ij} and σ_{jk} were estimated to be in the order of 10^{-16} cm^2 to 10^{-17} cm^2 using the typical dipole transition length for a molecule. Thus, the estimated 2-photon cross-section was found to be of about 10^{-49}cm^4 s/photon.

This approach can be further generalized for an n-photon absorption

$$\sigma_n = \sigma_{ij}\sigma_{jk}\sigma_{kl}\sigma_{lm}...\tau_j\tau_k\tau_l.... \tag{1.11}$$

and further simplified to

$$\sigma_n = \sigma_{ij}^n \tau_j^{n-1} \tag{1.12}$$

where σ_n is the n-photon absorption cross-section. This relation is correct if we assume that all 1-photon absoption cross-sections and the lifetimes of all intermediate states are the same.

From the relation above, the probability of observing an n-photon excitation, σ, should be equal to the molecule's capability of absorbing n-photons in a single event (molecular n-photon absorption cross-section), σ_n, and the incident photon flux (or intensity), I. The n-photon excitation process has an n-th order dependence on the intensity, I^n [5]. The probability of having a multiphoton excitation is given by

$$\sigma = \sigma_n I^n \tag{1.13}$$

The probability of observing an n-photon transition increases with intensity but the absorption cross-sections of the molecule decrease with each intermediate level added.

1.5 Localized Energy Deposition and Pulse Duration Effects

Multiphoton processes require very high intensities because of very low cross-sections. Thus, when a laser is tightly focused the multiphoton process only occurs at the focal volume. Therefore, in an n-photon (n>1) interaction process, the energy deposition is localized in the immediate region of the laser focus since it is where the photon density

is the highest (refer to figure 1.3). It is at the focus that the probability of having an n-photon absorption is more likely to occur due to the I^n dependance of the excitation process. With the nth-order dependance on the intensity, the interaction region is ever more confined with each successive photon added. This gives a nearly zero probability of an n-photon absorption outside the focal volume, as shown in Figure 1.3. This is a unique property of multiphoton interaction which gives the 3-D capability to a multiphoton microscope. Combined with ultrashort pulse durations that minimize thermal diffusion (discussed below), focused ultrashort pulses lead to localized energy deposition on a micron-scale.

The intensity requirement of a multiphoton process gives rise to localized interaction. However, high intensities are necessary in order to obtain multiphoton interactions. Such intensities can be easily generated by using ultrashort pulses with moderately low average powers. The intensity given by

$$I = \frac{E}{A\tau} \tag{1.14}$$

and the average power given by

$$P_{average} = Ef \tag{1.15}$$

where E is the pulse energy, A is the area of interaction, τ is the pulse duration, and f the repetition rate of the laser. The use of low average powers minimizes damages to biological systems by avoiding photodamage [13] (discussed later in this Chapter).

In addition, the use of ultrashort pulses with durations ($\tau = 10^{-15}$-10^{-12} s) shorter than the thermal expansion time (a few ps [14]) also ensures that no energy is transferred outside the interaction region which eliminates thermal damage and confines the interaction to the focal volume.

These are the unique features of ultrashort pulse lasers that are often exploited in multiphoton microscopy, micromachining and 3D photonic device fabrication.

Figure 1.3: This Figure compares the excitation volume of a fluorescent dye (located in a vial) by a multiphoton process (pointed by an arrow, using a multiphoton microscope) to that of a 1-photon excitation process (top, using a confocal microscope). The difference between the interaction volumes associated with the 2 process is clearly significant. For a multiphoton interaction, the excitation of the dye molecules only occurs where the intensity is at the highest and that is at the laser focus, as seen in the picture. This confined interaction is called energy localization, which is a unique property of multiphoton microscopy and gives it its 3D capability. (courtesy of Brad Amos MRC, Cambridge).

1.6 N-photon Fluorescence

The imaging of biological tissues is often accomplished by doping them with dye molecules which adhere to specific sites. In multiphoton microscopy, the dye is excited by the simultaneous absorption of photons. The fluorescence from the dye is within a frequency range of approximately n($\omega^{'} \pm \Delta\omega^{'}$), where $\omega^{'}$ is the central frequency of the emitted photons (maxima in the emission spectra of the molecule) and shifted by frequency $\Delta\omega^{'}$ by the radiationless decay from the excited state to sub-bandgap levels (see Figure 1.2) [9]. For this reason, all fluorescence emissions from a dye will have a certain bandwidth that is determined by the energy levels associated to the dye molecule. Fluorescence is, by definition, a sub-bandgap process but still requires the system to be brought to the excited state by providing the right amount of energy. In that state, the system goes through radiationless relaxation either by energy loss through vibrational or electronic states and shifts the system into a sub-bandgap energy level. This results in the release of lower energy photons. Undershooting the bandgap by failing to provide enough energy to excite the molecules from the ground state to the excited state produces no fluorescence. The excess energy is distributed to the lattice in the form of heat and other processes. On the other hand, exceeding the bandgap energy will release the electron into the conduction band by the process of photoionization which, again, produces no fluorescence.

In the previous section, the probability of observing an n-photon excitation was given by

$$\sigma = \sigma_n I^n(t) \tag{1.16}$$

Since fluorescence for low energy photons occurs via multiphotons processes, the observed fluorescence intensity for a n-photon excitation should be approximately equal to the probability of observing an n-photon transition [5, 6, 15].

$$I_{fluorescence}(t) \approx \sigma_n I^n(t) \tag{1.17}$$

where I(t) is the intensity at the focal volume and σ_n is the molecular cross-section.

From the relationship obtained in equation 1.17 and with the use of a microscope objective for light delivery, further approximation of the fluorescence intensity can be made as a function of power [6].

$$I_{fluorescence}(t) \approx \sigma_n P_t^n [\frac{\pi(NA)^2}{hc\lambda}]^n \tag{1.18}$$

Where NA is the numerical aperture of the objective, λ is the wavelength of light, h is Planck's constant, and P(t) is the laser power.
A more generalized relation can be made for the time-averaged fluorescence intensity for n-photon absorption per molecule.

$$\langle I_{fluorescence}(t)\rangle = \frac{1}{T}\sigma_n [\frac{\pi(NA)^2}{hc\lambda}]^n \int P(t)dt \tag{1.19}$$

CW lasers versus Pulsed lasers

In the case of a continuous wave (CW) laser, *P(t)* is equal to the average power and equation 1.19 becomes [6]

$$\langle I_{fluorescence,CW}(t)\rangle = \sigma_n [\frac{\pi(NA)^2}{hc\lambda}]^n P_{ave}^n \tag{1.20}$$

In the case of a pulsed laser, $T = 1/f_p$ and $P(t) = P_{ave}^n / f_p \tau_p$, and equation 1.20 becomes [6]

$$\langle I_{fluorescence,pulsed}(t)\rangle = f_p \sigma_n [\frac{\pi(NA)^2}{hc\lambda}]^n \frac{P_{ave}^n}{f_p^n \tau_p^n} \int_0^{\tau_p} dt \tag{1.21}$$

where f_p is the repetition rate of the laser and τ_p is the pulse duration.

In order to compare the efficiency of both lasers in producing fluorescence, the fluorescence intensities are made equal.

$$\langle I_{fluorescence,CW}(t)\rangle = \langle I_{fluorescence,pulsed}(t)\rangle \tag{1.22}$$

We then have

$$P_{ave,CW}^n = \frac{P_{ave,pulsed}^n}{\tau_p^{n-1} f_p^{n-1}} \tag{1.23}$$

As an example, consider a 3-photon excitation where $P_{ave,pulsed} = 0.1$ mW with a repetition rate of 5 kHz and pulse duration of 100 fs. $P_{ave,CW}$ would have to be 1.3×10^7 W to obtain the same fluorescence intensity as that of a pulsed laser. The use of such high power with a CW laser would destroy any sample situated at the focus.

This demonstrates the advantage of pulsed lasers over CW lasers. That is unless the

wavelength of light is made to be in resonance with the different energy levels of the molecules, CW lasers can not be used for the multiphoton excitation of dyes (or multiphoton ionization) due to the high power required and the damage that would occur to the sample. Conversely, pulsed laser would not be the choice for single photon excitation as it restricts the detection of the signal to that of the repetition rate of the laser. Furthermore, the use of short pulses lessens the collateral damage caused by thermal diffusion. For pulses shorter than the heat diffusion time (a few ps), the deposited energy is confined to the focus (or interaction region) without affecting the surrounding regions. In the case of a CW laser, the material is continuously exposed to the laser beam causing severe heat related damages to the surrounding regions over an extensive length.

1.7 Dependence of N-photon Fluorescence on Dye Concentration

In the previous section, the probability of an n-photon absorption was given by equation 1.16. However, an important factor that wasn't introduced but plays a critical role on the amount of fluorescence being produced at the focal volume is the dye concentration, C(r,t). To calculate the true amount of fluorescence emitted from the focus (or the amount of n photons absorbed), the concentration of the dye tagged to the sample must be added into equation 1.16 in order to calculate the rate of emission.

The total amount of absorbed photons per unit time, N_{abs}, is thus given by the relation [16, 17]

$$N_{abs} = \int_V dr \sigma_n C(r,t) I^n(r,t) \tag{1.24}$$

where n is the number of photons, σ_n is the n-photon absorption cross-section, I is the incident intensity, and V is the illuminated volume.

Another factor that is ignored is the dependence of the n-photon absorption process on the laser's temporal coherence (how well the waves can interfere). The nth-order temporal coherence of the excitation source is important since each photon participating in the n-photon excitation imparts its angular momentum and phase transfer to the electron. This can lead to constructive interference bringing the electron into the excited state, producing fluorescence, or destructive interference leaving the system in the ground state (no fluorescence). For this reason, temporal coherence for an nth-order

interaction is an important factor when determining the cross-section for a multiphoton excitation. Maclain and Harris [17] included this factor to give an approximation of the amount of photons emitted per unit time, F, from the focal volume. They assumed the absence of photobleaching and ground state depletion from their calculation which gives the following relation.

$$F(t) = \frac{1}{n}\phi\eta N_{abs} \tag{1.25}$$

where η is the quantum efficiency of the fluorescent dye and ϕ is the collection efficiency of the detection system.

The value of the parameter ϕ is an evaluation of the performance of the system in detecting fluorescence emissions and is determined by the collection efficiency of the detection system, the transmission of the optical elements within the beam path, and the quantum efficiency of the detector. The quantum efficiency of the dye, η, is determined by the ratio of the number of photons emitted to the number of photon absorbed. Consequently, η can have a value ranging from 0 to a maximum of 1 (100% efficiency).

The average photon flux in the focal volume is given by [18]

$$F(t) = \frac{1}{n}g^{(n)}\phi\eta N_{abs}C(r,t)\sigma_n\langle I_o(t)\rangle^n \int_V drS^n(r) \tag{1.26}$$

where C is the concentration of the dye within the focal volume, $g^{(n)}$ is the measurement of the nth-order temporal coherence of the laser, and S(r) describes the spatial distribution of the incident light. The parameter $g^{(n)}$ is given by

$$g^{(n)} = \frac{\langle I_o^n(t)\rangle}{\langle I_o(t)\rangle^n} \tag{1.27}$$

where I_0 describes the temporal distribution of the excitation source and I_0^n is proportional to the total emitted fluorescence.

Assuming a Gaussian-Lorentzian beam profile for the excitation beam and a sample thickness larger then the Rayleigh length, (for n $\geq$ 2) we have [18].

$$\int_{V\to\infty} S^n(r)dr = \frac{(2n-5)!!n_o\pi^3\omega_o^4}{2n(2n-4)!!\lambda} \tag{1.28}$$

with the convention that $2n!!$ = 2·4·6· · ·2n, (2n-1)!! = 1·3·5· · ·2n-1, (-1)!! = 1 and (0)!! = 1 [18]. n is the number of photons absorbed during the excitation process, n_o is

the refractive index of the medium, ω_o is the beam radius, and λ is the wavelength of light.

Therefore, the time-average photon flux coming from the focal volume is given by

$$F(t) = \frac{1}{n} g^{(n)} \phi \eta N_{abs} C(r,t) \sigma_n < I_o(t) >^n \frac{(2n-5)!! n_o \pi^3 \omega^4}{2n(2n-4)!! \lambda} \tag{1.29}$$

1.7.1 Special Case of N-photon Fluorescence: Two-Photon Microscopy

In the case of a 2-photon excitation, equation 1.26 becomes

$$F(t) = \frac{1}{2} g^{(2)} \phi \eta N_{abs} C(r,t) \sigma_n \langle I_o(t) \rangle^2 \int_V dr S^2(r) \tag{1.30}$$

Assuming a Gaussian-Lorentzian beam profile and a thick sample (refer to previous section),

$$F(t) = \frac{1}{2} g^{(2)} \phi \eta C(r,t) \sigma_2 \frac{4}{\pi^2 \omega_o^4} \langle P(t) \rangle^2 \frac{n_o \pi^3 \omega_o^4}{4\lambda} \tag{1.31}$$

$$F(t) = \frac{1}{2} g^{(2)} \phi \eta C(r,t) \sigma_2 \langle P(t) \rangle^2 \frac{n_o \pi}{\lambda} \tag{1.32}$$

From equation 1.32, it can be observed that the fluorescence intensity is insensitive to the spot size. Thus, the total amount of fluorescence remains unchanged over the entire focal volume, ignoring the possibility of aberration [16, 19]. This property of the 2-photon process is exploited in 3-dimensional imaging of biological systems (like tissues). In two-photon microscopy (TPM), the excitation volume is limited to the focal spot due to the spatial and temporal intensity requirements that are only met at the focus (refer to Figure 1.3). This confinement of the excitation volume eliminates the need for pinholes in front of the detector and the excitation source to discriminate against out-of-focus information (often used in confocal microscopy, see following section) [20, 21, 22].

1.8 Confocal Microscopy

In conventional light microscopy, the object is instantaneously recreated in the image plane by the simultaneous imaging of each individual point of the original object. In Confocal microscopy (CM), the object is reconstructed point-by-point by raster scanning the focal plane of the objective with the laser beam using a pair a galvanometric mirrors and by collecting and measuring the fluorescence emissions produced from each individual

point by the interaction of the laser beam with the dye molecules. What differentiates both microscopes is that in CM, the object's information is collected using a pinhole aperture through a process known as the confocal principle. It is achieved by placing a pinhole in front of the detector that is in a conjugated plane with that of the focal plane of the objective. The pinhole's purpose is to eliminate out-of-focus information by blocking information from above and below the plane of interest (see Figure 1.4), enabling optical sectioning (see Figure 1.5) and thereby permitting 3-dimensional imaging [23, 24, 25].

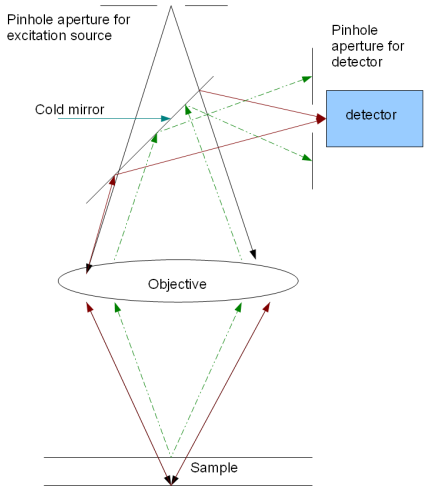

Figure 1.4: Principle of Confocal Imaging: the efficiency of cutting out-of-focus information is limited by the physical size of the pinhole aperture.

The buildup of a 3D replica of the original object is achieved by displacing the objective's focus along the z-direction. The thickness of the optical slices is determined by the physical size of the pinhole aperture; the smaller the pinhole aperture, the smaller the optical slices are and the better the resolution [26]. Information collected from each individual point from all the optical slices are stored on the computer's memory. The optical slices are then stacked on top of each other to recreate a 3D replica of the object without having to physically cut the sample one layer at a time (see Figure 1.5).
On an important note, it is to be said that the confocal property is not violated by the introduction of the mirrors along the beam path since the mirrors move slowly compared to the speed of light (i.e. the information collected can be precisely associated to a po-

sition in the focal plane). Hence, the emissions follow the path along the optical axis which is identical to the original path used by the excitation beam [26].

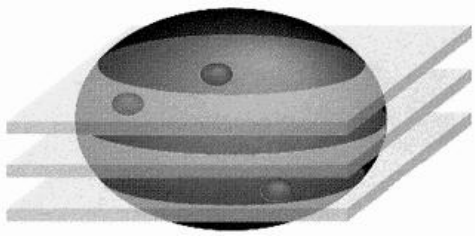

Figure 1.5: Optical sectioning and creating a 3D replica of a sphere by projecting each optical slice on top of one another.

The main weakness of conventional CM comes from its use of a CW laser to illuminate the sample in order to excite dye molecules. This use of a CW source to image is a large disadvantage as the CW laser is more likely to cause significant damage to the sample, affecting the physical integrity of the tissues and the viability of the cells. The damage is not localized and affects regions in all directions over a significant distance. Furthermore, the use of a CW laser blazing through the sample excites a large volume due to the cross-section of a 1-photon excitation being relatively high, resulting in the excitation of regions located outside the focus of the microscope objective (large background noise). This necessitates the use of a pinhole to block out-of-focus information. On this note, the goal of this thesis is to build a system that will have both the ability to image biological tissues as well as do precise ablation, which is simply not achievable when using a CW laser.

1.8.1 Confocal Microscopy versus Two-Photon Microscopy

The two-photon microscope has the same capability as the confocal microscope to image in 3-D. However, TPM is much more promising when it comes to the care and imaging of soft tissues since it is not as detrimental to the viability of the cells. These advantages come from the excitation source used for imaging.

In conventional CM, which is a 1-photon excitation process, the wavelength of the laser must match the excitation wavelength of the dye in order to have an efficient means of producing fluorescence, restricting the light source to a CW laser. (Pulsed lasers can

be used but like previously mentioned when it comes to signal detection it is not very logical to use one)

The use of a CW laser, in CM, comes at the cost of inducing damage and affecting the physical integrity of the sample being imaged [27, 28]. Damage to tissues such as photobleaching, photochemical damage, and photoxicity are pre-dominant when using shorter wavelengths to excite dye molecules. Since most dyes fluoresce in the near-ultraviolet (UV) and visible light regimes, such damages are unavoidable when using an excitation source with the same wavelength and results in severe degradation of the samples. These damage types are described below.

- **Photobleaching**
  Photobleaching (see Figure 1.6) is the photochemical destruction of the dye molecules when exposed to light for the process of exciting and stimulating them to fluoresce. The dye molecules are attenuated and destroyed by the exposure of the light. This process is pre-dominant when using CW lasers in the near-UV and visible spectra [29, 30, 31, 32].

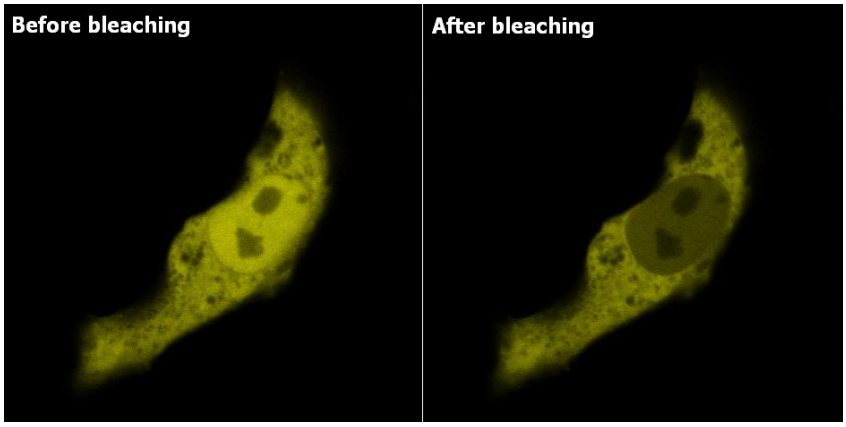

Figure 1.6: Demonstrates the ability of a dye to fluoresce before (left) and after (right) photobleaching. A clear reduction in the fluorescent intensity, coming from the same regions, can be observed and is attributed to the photochemical destruction of the dye by its exposure to the light source. [33]

- **Phototoxicity**
  Phototoxicity happens when the dye excited (by a photon or numerous photons) returns to the ground state, after thermal relaxation, emitting a photon of lower energy due to a Stokes shift. The excess photon energy is transferred to the oxygen in the cell nonradioatively, thereby killing it. This can be easily avoided by decreasing the excitation energy by using low energy photons and decreasing the exposure time of the cells to the excitation source [34, 35]. Using low energy photons reduces the transfer of excess photons energy to the biological systems minimizing the generation of oxygen radicals.

- **Photochemical**
  Photochemical damage occurs when light triggers a reaction by exciting endogenous and exogenous absorbers located within the biological sample. This is followed by a phototoxic reaction such as the formation of free radicals, resulting in oxidative stress, or the excitation of amino acids inducing severe irreversible DNA damage [13]. Peak absorption of these absorbers are mostly located in the UV and visible range. Photochemical damage can be avoided by using longer wavelengths, reducing power, and by decreasing the exposure time of the biological sample to the excitation source.

The strength of TPM comes from the use of an ultrafast laser as the excitation source. For maximal performance, lasers used in TPM are centered in the near-IR spectral region and emit intense pulses of only a few femtoseconds in duration. The use of low energy photons for excitation significantly reduces the probability of photodamage, which is typically wavelength dependent and generally more severe with shorter wavelengths. Since the probability of photodamage to biological tissues depends also on the exposure time of the sample to the excitation source, pulsed lasers (depending in the repetition rate and pulse duration) greatly reduce the exposure time of the sample to the excitation source. Moreover, the use of longer wavelengths to image biological tissues enables access to information located deeper within the sample due to the reduction in scattering [36, 37].

1.9 Photoionization

In atoms or molecules, photoionization occurs when the incident photon energy (or sum of the total energy of the photons simultaneously absorbed) transferred to the electron is greater than the binding energy of the electron, releasing the electron into the continuum. In solids, the energy should be greater than the bandgap in order to excite the electron from the valence band into the conduction band. For sub-bandgap photons, ionization can still occur by multiphoton processes where n-photons are simultaneously absorbed. The multiphoton process depends on the intensity delivered to the interaction region. There are two regimes in which ionization can occur: either by n-photon absorption or tunnel ionization. The regimes are distinguished by the Keldysh parameter [38, 39, 40, 41].

The Keldysh parameter, γ, is calculated using

$$\gamma = \frac{\omega}{F}\sqrt{2E_0} \tag{1.33}$$

where ω is the laser frequency, F is the electric field strenth, and E_0 is the ionization potential of the atom or molecule. Keldysh concluded that for the value of $\gamma \gg 1$, tunnel ionization would prevail over multiphoton ionization and that for the value of $\gamma \ll 1$ the inverse would be true. In the case where $\gamma \approx 1$, both regimes play a role in the ionization process.

1.9.1 Multiphoton Ionization (MPI)

Multiphoton ionization can be visualized as the simultaneous absorption of n-photons whose total combined energy exceeds that of the bandgap in a solid or the ionization potential (IP) in an atom. The energy transfered to the electron promotes it from the valence band into the conduction band, or continuum, thus creating a free electron [42, 43]. This process can occur in 2 different ways. First, via virtual intermediate states (unallowed 1-photon transitions) and, second, through allowed 1-photon transitions via real-resonance, as shown in Figure 1.7.

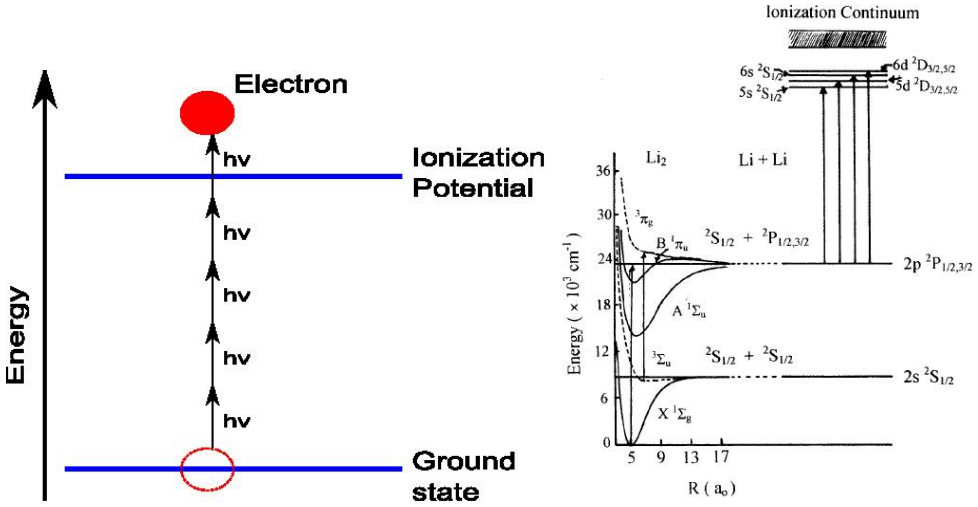

Figure 1.7: Schematic of multiphoton ionization by the absorption of n-photon of frequency v (left) via intermediate states and (right) through allowed 1-photon transitions via real-resonance (for a Li^2 molecule).

1.9.2 Tunnel Ionization

Tunnel ionization starts to become dominant when intensities delivered to the interaction region exceed 10^{14} W/cm^2. First observed in Xenon atoms in 1985 by Chin *et al.* [44], tunnel ionization was explained as the distortion of the Coulomb potential in the presence of an intense electric field. During the short time that the Coulomb potential is bent, there is a finite probability that the electron may tunnel through the barrier into the conduction band or continuum creating a free electron (figure 1.8).

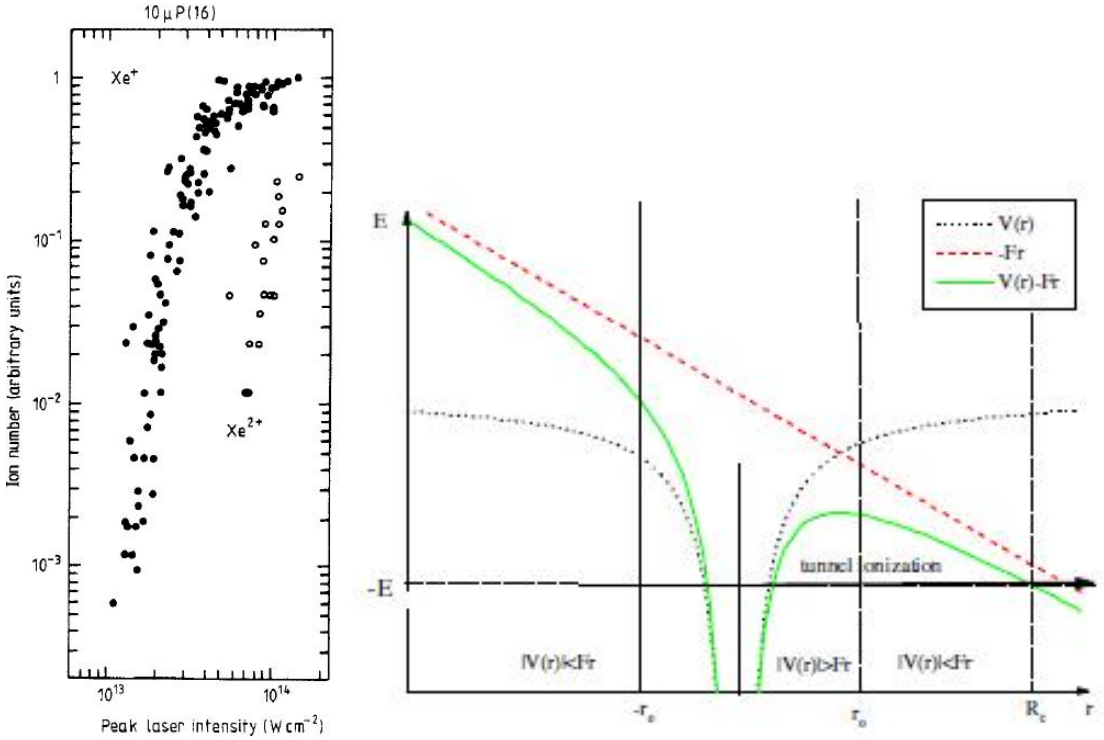

Figure 1.8: (left) Result obtained by Chin *et al.* experimentally confirming the process of tunnel ionization by unexpectedly detecting doubly ionized Xenon in the presence of a strong electric field [44]. Reprinted with permission from the Institute of Physics(IOP). (right) Schematic of tunnel ionization, demonstrating the bending of the Coulomb Potential in the presence of a strong electric field and the tunneling of the electron into the continuum.

In solids, additional ionization mechanisms exist and are described below.

1.9.3 Impact Ionization

Impact ionization starts to play an important role for pulses longer then 50 fs [39, 45]. From a long pulse, a high density of free electrons is reached by the process of multiphoton and/or tunnel ionization. This high density of electrons in the conduction band enhances collisions between electrons in the presence of an electic field. The impact of the high energy electrons in the conduction band and the surrounding bound electrons knocks out the bound electrons from the valence band, producing more free electons. The longer the pulse is, the higher is the density of free electrons as well as the probability of collisions

which grows into an avalanche process with longer pulse durations [41, 46, 47].

1.9.4 Shot-to-Shot Memory

In linear optics, the bandgap is fixed so the energy deposited into the region must be greater then the bandgap in order to photoionize. The introduction of ultrafast lasers to photoionize a material introduces a nonlinear component to the photoionization process; a phenomenon known as shot-to-shot memory [39, 48, 49]. Shot-to-shot memory is a nonlinear interaction with the material where each laser shot induces a change within the region which lowers the bandgap energy required for photoionization. This process continues for each laser shot delivered to the region until the change in the bandgap reaches a saturation where the bandgap can no longer be lowered.

The existence of such a nonlinearity was first demonstrated experimentally by P.P. Rajeev et al. [49] while conducting experiments inside fused silica glass. They showed, by monitoring the transmission and by keeping the light focused unto a fixed position, that the transmission as a function of pulse energy did not retrace itself when ramping up and down the energy delivered to the interaction region (see Figure 1.9). The number of shots delivered to the interaction region, increased throughout the experiment. The hysteresis like effect is an indication of a memory in the nonlinear ionization of fused silica. This memory effect is explained as the accumulation of laser-induced chemical changes in the modified regions constituting a feedback mechanism.

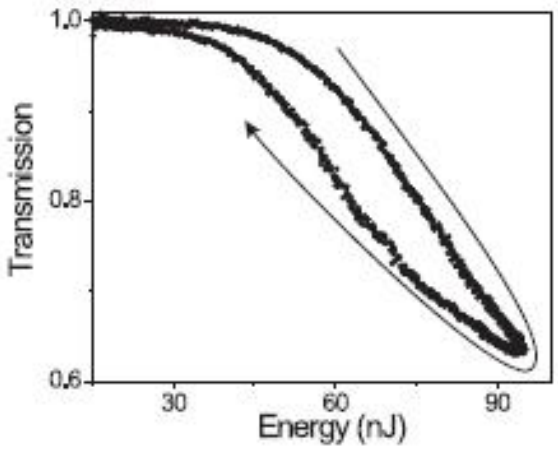

Figure 1.9: Demonstration of nonlinear absorption inside fused silica. The graph is plotted for transmission as a function of pulse energy. The laser focus is fixed and the pulse energy is gradually increased from shot-to-shot and then reduced. The transmission curve didn't retrace itself. The hysteresis like curve indicates memory in nonlinear ionization. The full cycle consisted of 17 000 shots. The arrow follows the path of increasing number of shots. Reprinted with permission from [49]. ©2006 by The American Physical Society.

Further insight into the memory effect is obtained by measuring the transmission as a function of number of laser shots at a fixed pulse energy. Figure 1.10 shows the transmission of an ionizing pulse as a function of number of shots in fused silica [49], using a pulse energy of 160 nJ which is 3 times the ionization threshold of a fresh sample. The transmission of a fresh sample (solid circles) is compared to a previously exposed one (open circles) as a function of laser shots. From Figure 1.11, following the first laser shot, it is observed that as the number of laser shots increases, the transmission decreases until it reaches a saturation (after a few thousand shots). This observation confirms the existence of a memory in the nonlinear ionization process. In addition, it indicates a saturation to the mechanism where the ionization threshold can no longer be lowered by a cummulative effect.

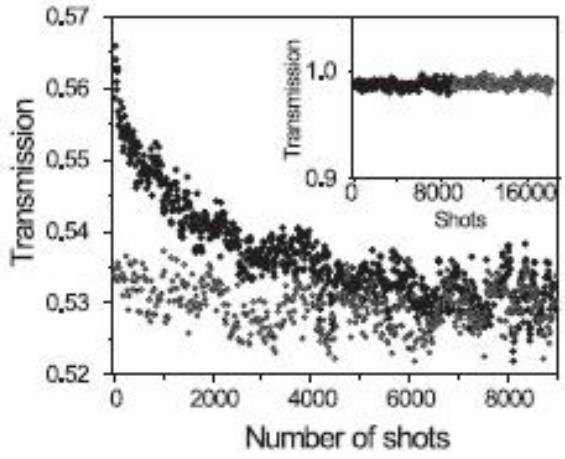

Figure 1.10: Demonstates the nonlinear absorption as a function of exposure at the fixed pulse energy of 160 nJ. The transmission is plotted as a function of the number of laser shots. Comparing the transmission of a fresh sample (solid circles) to a previously exposed one (open circles) as a function of the number of laser shots. The open circles show the transmission through the same spot having left the laser off for 1 hour. Demonstrating that the memory operates only in a nonlinear regime. Reprinted with permission from [49]. ©2006 by The American Physical Society.

The changes induced by the nonlinear memory were quantified by modeling the transmission. Figure 1.11, compared the transmission of a fresh sample of fused silica glass (moved between laser shots) and a sample previously exposed to 10 000 shots at a pulse energy of 160 nJ. The solid lines in the figure were obtained by solving the self-limiting model numerically that included avalanche ionization. Using the following relation

$$\frac{dn}{dt} = \alpha I n + W(I) \tag{1.34}$$

Where dn/dt is the carrier generation rate, I is the laser intensity, α is the avalanche coefficient, and W(I) is the nonlinear ionization rate. In [49] the absorption rate is approximate as $W(I) = \sigma_k I^k$, where n is the number of photon participating in the interaction (6 for the ionization of fused silica) and σ_k is the nth-order cross-section.

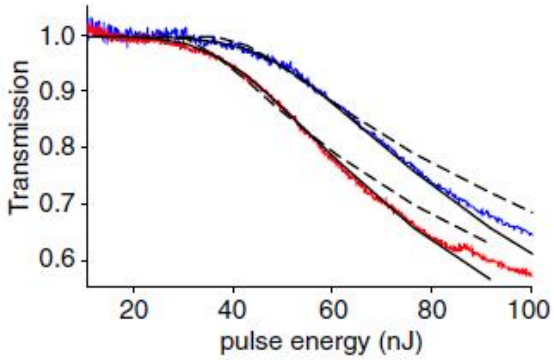

Figure 1.11: Transmission is plotted as a function of laser pulse energy. Used by [49] to model the nonlinear absorption in order to characterize the memory. The blue curve is obtained by moving the sample so that fresh material is irradiated on each shot. This curve is used as a baseline for assessing the memory effect. The red line is obtained at single spot after exposure to 10 000 shots at 160 nJ. The solid lines are fits from the numerical modeling that includes the nonlinear absorption using equation 1.34. The dashed lines show fits of simple sudden onset analytical model, that neglects avalanche, to the early portions of the transmission curves. It is from this fit that the threshold intensities are obtained. [49]. ©2006 by The American Physical Society.

From the fits (solid lines) in Figure 1.11, the value of the avalanche coefficient, α, was set at 4 $J^{-1}cm^2$. They calculated, from equation 1.45 and Figure 1.11, a cross-section of $\sigma_6 = 4\times10^{13}(\text{TW cm}^{-2})^{-6}$ cm^{-3} ps^{-1} for the fresh sample and a cross-section of $\sigma_6 = 1.6\times10^{14}(\text{TW cm}^{-2})^{-6}$ cm^{-3} ps^{-1} for the memory satured glass, revealing an increase by a factor of 4. This increase in the cross-section indicates a permanent change in the material that effectively reduces the bandgap. From the dashed lines, in the early part of the transmission curves, the ionization threshold for the fresh sample was determined to be of 1.2×10^{13}W cm^{-2} whereas the ionization threshold for the material previously exposed was determined to be of 9.5×10^{12}W cm^{-2}, where the memory effect had been saturated, indicating lower ionization threshold for previously exposed samples. Interestingly, it was also showed that for different pulse energies, the memory effect in fused silica always saturated at a drop in threshold of $\approx 20\%$. The only difference was the rate at which the memory was established.

This phenomenon is general and should also occur in PMMA. However, the chemical

changes are different. In fused silica, Raman experiments have indicated that there is a chemical change in which the five and six membered rings shrink to form three to four membered rings [49]. Where as in PMMA, the chemical change is due to the combination of depolymerization (i.e. dissociation of the PMMA polymer chains) and cross-linking (i.e. re-connection of the dissociated polymer chains) [50]. This chemical change, in PMMA, can be observed visually by the emission of green fluorescence from the laser-modified regions when exposed to a specific wavelength of light due to bond scissions, see Figure 1.12.

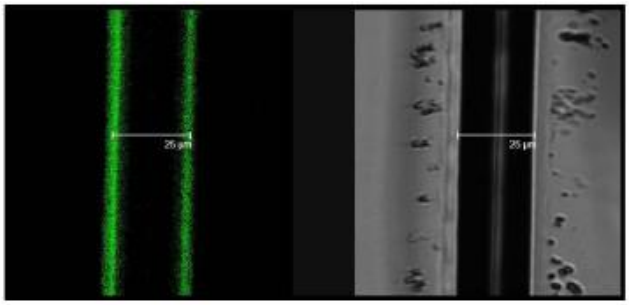

Figure 1.12: Picture taken of an ablation crater at the surface of a PMMA sample. The green fluorescence indicates a chemical reorganization (bond scissions). Causing fluorescent emissions ($\approx$ 540 nm) when exposed to a wavelength of $\approx$ 480 nm. The absence of emissions from the central part of the crater is due to the removal of the material by the ablation process. Reprinted from [50]. ©2010 with permission from the Institute of Physics(IOP).

1.10 Ablation

A consequence of the interaction of intense light pulses on a solid surface is ablation. Ablation is the systematic removal of material when exposed to intense short pulses of light. The energy deposited onto the material's surface produces a plasma due to multi-photon ionization. The expansion of the plasma results in material ejection. The plasma that is formed is radially confined in the lateral and downward direction due to the high atomic density of the medium but on the surface, it is unconfined in the upward direction and is free to expand. This results in the ejection of debris and particles in the form of a plume [14, 39, 46, 51, 52, 53]. The use of sub-picosecond pulses for laser ablation has two dominant ionization processes responsible for the formation of the plasma. The

leading edge of the pulse utilizes strong field ionization as the dominant process and the trailing edge will use mostly impact ionization [39, 46, 47]. For few-cycle pulses, impact ionization may not play a critical factor in the ionization process as free electron densities may not be large enough to initiate an avalanche process.

Pulsed lasers are widely used for ablation in the medical field and for the micromachining of materials. Ablation processes result in the vaporization of material without any substantial heating of the bulk and for sub-picosecond pulses, there is minimal thermal damage outside the interaction region since the pulse duration is shorter than the thermal diffusion time (Figure 1.13) [14].

Figure 1.13: Ablation of steel using (left) femtosecond pulses and (right) nanosecond pulses. This demonstrates the absence of thermal damage (left) using sub-picosecond pulses which are shorter than the thermal expansion time [54].

1.10.1 Laser Ablation of Soft-Matter in a Water Environment

As mentioned at the beginning of this thesis, a primary goal is to study the physical interaction of intense light pulses with soft-matter in its native environment. Experimentally the ablation of soft-matter in its native environment is extremely complex and not well understood. Hence, since most biological systems contain significant amounts of water, it is crucial to understand the theory of optical breakdown in a water environment.

The energy deposited during the ablation of any material in water can be either absorbed, transmitted, reflected, or scattered [55]. The absorbed energy is branched out into multiple optical breakdown mechanisms. These mechanisms are: evaporation energy,

plasma radiation, shock waves, and cavitation bubble formation [55]. For optimal results in laser ablation, the absorbed energy should be efficiently converted into evaporation energy since that is the process responsible for the removal of material. The conversion of absorbed energy into any other mechanism (mechanical energy) will result in a disruptive character of the ablated region [55, 56, 57]. In soft-matter, shockwave emissions are not damped by the density of the material (unlike in hard materials) resulting in the generation of cavitation bubbles which ultimately lead to a disruptive character of the breakdown process. For this reason, finding a set of parameters that maximises the conversion of the absorbed energy into evaporation energy is of the utmost importance when ablating materials in water. Such studies were carried out by A. Vogel *et al.* using pulsed lasers [55].

Vogel's studies experimentally determined the percentages of energy absorbed in the optical breakdown of water for different pulse durations as well as the percentage of conversion of absorbed energy into evaporation energy and other processes. Their values were obtained by resolving the amount of energy absorbed and how much of that energy was diverted into the formation of cavitation bubbles. Below is a brief overview of how they differentiated and calculated the amount of energy branching out into these different mechanisms (refer to [55] for more details).

- **Energy of plasma radiation (E_R)**

  The energy of plasma radiation, E_R, is determined using the observations made by Barnes and Rieckhoff [58] and Stolarski et al. [59]. They found that the spectral density of the plasma radiation was very similar to the spectral distribution of a blackbody radiator when in the wavelength range of 300-900 nm. From this observation they calculated E_R using the following relation:

  $$E_R = \sigma A \tau_R T^4 \tag{1.35}$$

  Where T is the plasma temperature, A is the plasma surface area, τ_R is the duration of the plasma and σ is the Stefan-Boltzmann constant (σ=$5.670\times10^{-8}\frac{W}{m^2K^4}$).

  From this relation and by determining experimentally the surface area of the plasma taken by plasma photographs, the duration of the plasma radiation using a fast photodiode and taking the temperature of the plasma from litterature. They were

able to determine with good accuracy the amount of energy converted into plasma radiation.

- **Evaporation energy (E_V)**

  In order to determine the evaporation energy, E_V, Vogel et al. made the assumption that all the water located within the plasma volume had been evaporated. In addition, they neglected any enlargement of the evaporated liquid volume by heat conduction since the pulse duration was extremely short compared to the thermal expansion time. From these assumptions, they calculated the amount of energy necessary to evaporate a certain volume of water. Using the following relation:

$$E_V = \rho_0 V_p (c(T_2 - T_1) + r) \tag{1.36}$$

  Where ρ_0 is the density of water ($\rho_0 = 998 \frac{kg}{m^3}$), T_1 is the room temperature ($T_1 = 20°C$), T_2 is the temperature required to transform water into vapor ($T_2 = 100°C$), V_p is the plasma volume, c the specific heat (c = $4.18 \frac{kJ}{kgK}$) and r is the isobaric evaporation enthalpy (r = $2256 \frac{kJ}{kg}$).

  From this relation and the by determining the plasma volume, V_p, from photographs of the plasma luminescence, they were able to calculate the amount of energy that was converted into evaporation energy.

- **Cavitation bubble energy (E_B)**

  The amount of energy converted into the formation of cavitation bubbles is calculated using the following relation:

$$E_B = \frac{4\pi}{3}(p_0 - p_V) R_{max}^3 \tag{1.37}$$

  where p_0 is the hydrostatic pressure, p_V is the vapor pressure inside the bubble and R_{max} the radius at time of maximum bubble expansion. The value of p_0 and p_V were already known from litterature ($p_0 = 2330$ Pa at $20°C$ and p_V =0.1 MPa) whereas R_{max} had to be determined experimentally.

  The value for R_{max} is given by the following relation:

$$R_{max} = \frac{T_B}{2 \times 0.925 \sqrt{\frac{\rho}{p_0 - p_V}}} \tag{1.38}$$

Where T_B is the oscillation period related to the bubble size and ρ_0 is the density of water.

Hence, from these relations and by determining the oscillation period of the cavitation bubble through an hydrophone measurement, Vogel et al. were able to calculate the amount of energy that was converted into cavitation bubble energy.

- **Accoustic energy** E_S

  Lastly, Vogel et al. estimated the shock wave energy using the following relation:

$$E_S = \frac{4\pi r_m^2}{\rho_0 c_0} \int p^2 dt \tag{1.39}$$

  Where r_m is the distance from the emission at which the pressure p is measured, ρ_0 is the density of water and c_0 is the velocity of sound in water.

  However, due to the complexity of measuring directly the shock wave profile, p(t), close to the plasma, Vogel et al, instead, theoritically calculated the profile of the shock wave by basing themselves on the Gilmore model of cavitation bubble evolution. This was done by entering some measured parameters into the calculations (refer to [56] for more details). Parameters such as: the plasma volume from photographs of the plasma luminescence, the pulse duration and the maximum radius of the cavitation bubble. From this approach Vogel et al. were able to estimate the amount of energy converted into shock wave energy.

From these systematic and rigorous studies, it was observed (see Figure 1.14) that the amount of absorbed energy was lower for pulses of 30 ps than for pulses of 6 ns in duration. It was also demonstrated that the amount of absorbed energy was greatly increased when using pulse durations shorter than 3 ps. This was explained by the increasing role of multiphoton ionization within the interaction region, resulting in high electron densities early in the pulse and as a consequence, increased absorption within the region.

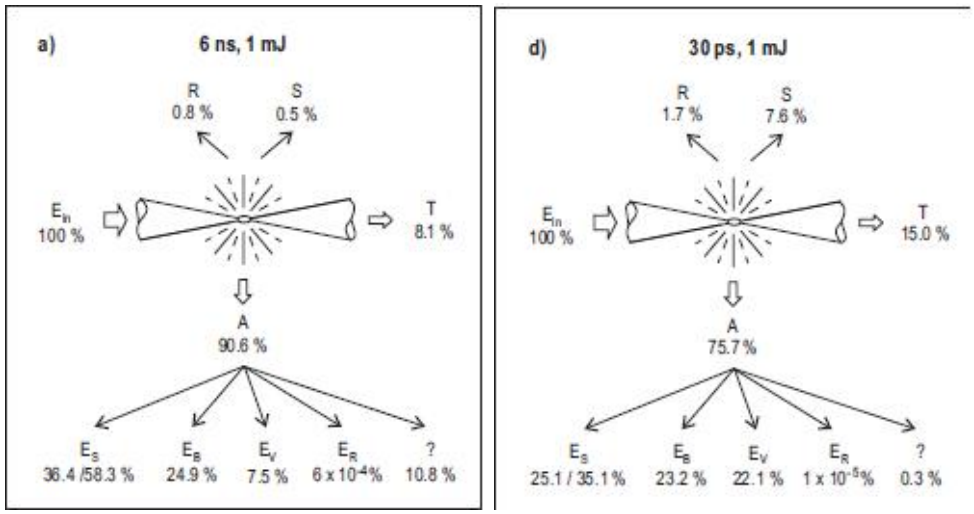

Figure 1.14: Result obtained by A. Vogel *et al.* [55]; (a) The energy distribution for a 6 ns pulse with 1 mJ of energy, (d) 30 ps pulse with 1 mJ of energy. The parameters R, S, T, and A are respectively denoted as reflection, scattering, transmission and absorption. The figure shows the percentage of energy divided into each of the parameters. The energy absorbed is then divided into multiple mechanical pathways during the breakdown process. E_s is the shockwave energy, E_B is the cavitation bubble energy, E_V is the evaporation energy, E_R is the plasma radiation and ? is the energy converted into unknown mechanisms. Reprinted with kind permission from Springer Science+Business media.

There are subtle differences between the ablation process on hard surfaces and soft matter. When ablating on hard surfaces, reflection plays a more significant role due to the electron density exceeding the plasma frequency [55, 60]. In water, such an electron density is not usually met and as a result, the plasma frequency remains smaller than the light frequency, allowing light to be transmitted [55, 61]. The reflected and transmitted light by the plasma is detrimental to the laser ablation process. The desirable outcome would be to have maximum absorption with minimum reflection and transmission. Figure 1.15 demonstrates the dependence of transmission on pulse duration.

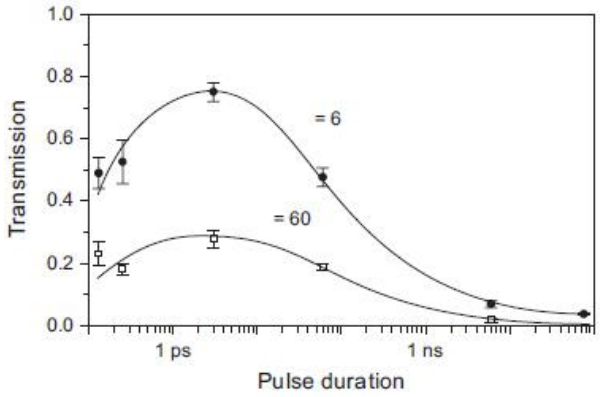

Figure 1.15: Demonstrates the dependence of plasma transmission on pulse duration. 6 and 60 are values of the dimensionless parameter β whose values are given by the ratio E/E_{th}. Where E is the pulse energy and E_{th} is the threshold energy required for the optical breakdown of water [55]. Reprinted with kind permission from Springer Science+Business media.

In this same study by A. Vogel *et al.*, the group experimentally showed that the conversion of absorbed energy into mechanical energy was less then 15% for fs pulses and $\approx 90\%$ for ns pulses (pulse duration where the absorption was maximum). Results showed that the conversion into mechanical energy increased rapidly with pulse duration (see Figure 1.16). This was explained in terms of deposition of energy during the breakdown process within the focal volume which is highly dependent on the pulse duration [55, 62]. When ionizing within the focal volume, electrons are brought into the conduction band where they collide with surrounding bound electrons, transferring their energy and eventually recombining with atoms. The time scale at which this energy transfer takes place is on the order of a few ps [14]. Hence, for pulses longer than this time scale, a large amount of energy is transfered to the surrounding regions giving a disruptive character to the breakdown process. For pulses shorter than the energy transfer time (few ps), no energy is transferred outside the focal volume resulting in a breakdown process that is spatially contained and eliminating thermal damage outside the focal volume.

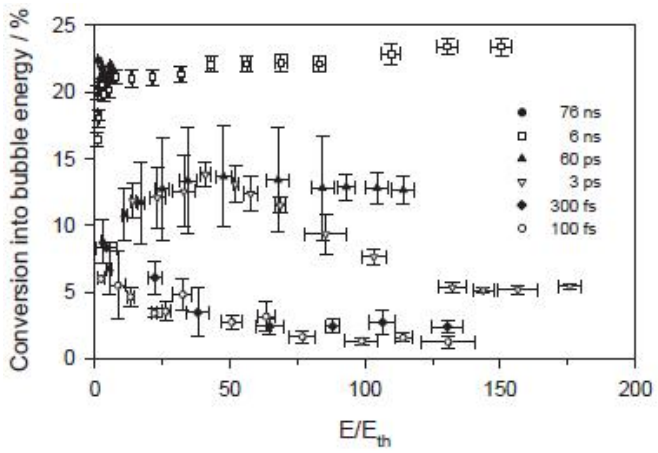

Figure 1.16: The conversion of energy into cavitation energy for different pulse durations. β is the dimensionless pulse energy ratio E/E_{th} [55]. Reprinted with kind permission from Springer Science+Business media.

The study concluded that the ratio between mechanical energy (E_{mech}), and evaporation energy, (E_V), was of 12:1 for ns, 2:1 for 30 ps and 1:2 for fs pulses [55]. The ratio of 1:2 for fs pulses demonstrated that the use of femtosecond pulses for ablating material in water significantly reduced the unwanted side effects of the breakdown process by decreasing the amount of energy converted into mechanisms responsible for the disruptive character of the ablation process. In other words, the use of fs pulses to ablate in a water environment as much better outcomes and is by far less damaging.

1.10.2 Internal Modification

Intense laser pulses focused inside a transparent material result in the creation of a plasma that, unlike surface ablation, is not free to expand and is confined to the interaction region. There is no ablation and removal of material; instead, permanent changes to the refractive index of the material are observed and are limited to the interaction region [39, 48, 51]. These changes induced in the refractive index of the material are the result of the chemical and structural reorganization that occurs within the interaction region after the cooling of the plasma. This chemical reorganization leads to the permanent refractive index change within the focal volume (see Figure 1.17). The extent of modification to the refractive index within the focal volume will depend on the change in the density made within that region which in turn, depends on the energy delivered to

the interaction region [39]. Furthermore, since the interaction is nonlinear, there exists a threshold for the changes in the refractive index that is specific to each material.

Experiments conducted by various groups on polymethyl methacrylate (PMMA) attributed the permanent refractive index change in PMMA, within the bulk, to the combination of depolymerization and cross-linking [63]. Depolymerization occurs when the light is focused inside the PMMA sample resulting in the photionization and the break of the PMMA chains. The chemical reorganization (following the plasma) is done through the cross-linking of the dissociated PMMA chains. The cross-linking increases the density within the interaction region. This increase in the density in turn relates to an increase in the refractive index. The presence of a chemical reorganization process in PMMA as been confirmed by the obervations of Deepak L.N. Kallipelli et al. [50]. They observed fluorescence emissions from the laser modified regions when exposing them to laser radiation (see Figure 1.17). The emissions were explained as bond scissions due to a chemical restructuration within the laser-modified regions which causes fluorescent emissions ($\approx$ 540 nm) when exposed to a specific wavelength of radiation ($\approx$ 480 nm). The fluorescent emissions, from the laser-modified regions, were still visible months after the deposition of energy within the bulk, suggesting that the changes within the interaction regions are permanent.

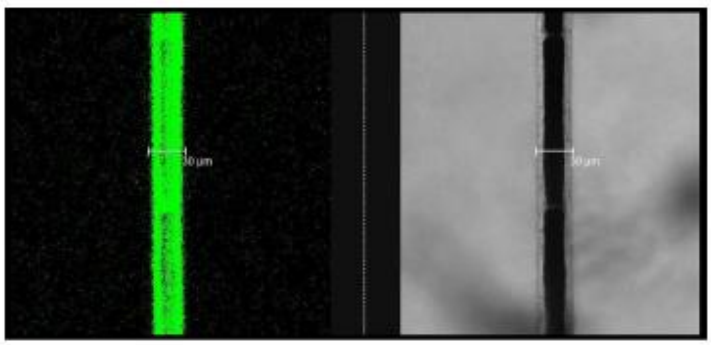

Figure 1.17: Fluorescence emissions ($\approx$ 540 nm) coming from the modified region, within the bulk of the PMMA sample, when exposed to laser radiation ($\approx$ 480 nm) The emissions are due to bond scissions (chemical reorganisation) within the laser-modified regions. These emissions were observed for months after the modication indicating a permanent change within the PMMA simple. Reprinted from [50]. ©2010 with permission from the Institute of Physics(IOP).

Waveguides

Waveguides, the basic building block of any photonic device, can be created by the displacement of the laser's focus inside transparent materials along the entire length of the sample, resulting in laser modified regions having a higher refractive index compared to the surrounding regions (see Figure 1.18). This makes them ideal to guide optical waves by total internal reflection.

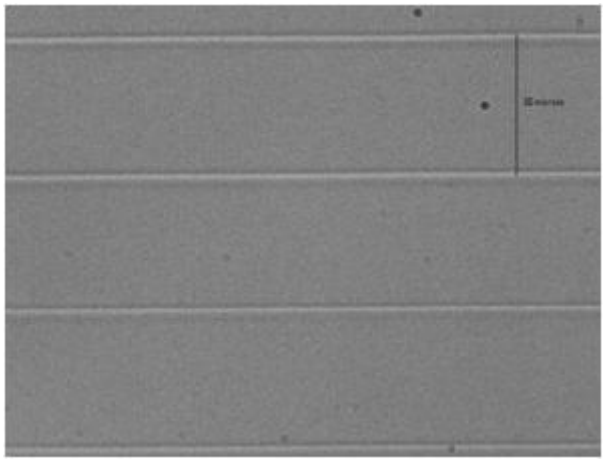

Figure 1.18: Results obtained from experiments done on PMMA. The light was focused inside the PMMA sample creating a plasma in a confined region causing a chemical restructuration within the interaction region. Each line (each done with a different pulse energy) are permanent refractive index changes within the PMMA bulk. This picture was taken by a CCD camera mounted to an optical microscope using a 20x objective.

Nano-planes

Under certain conditions, it was observed that the modifications within the focal volume would transform into multiple periodic regions with the modification confined to nanometer dimensions (see Figure 1.19) [48]. The creation of these nano-planes is the result of localized ionization and laser-plasma interaction. Ionization can become localized by the works of 2 contributing factors. First, the presence of defects within the material (such as color centres) having a lower bandgap than the surrounding region and, second, shot-to-shot memory that lowers the bandgap within the focal volume. The combination of the 2 forms an non-uniform plasma. As a result, nanoplasmas are ramdomly formed

that grow into planes due to local field enhancements. Figure 1.19 shows periodic nanostructures. The separation between the structures is ≈ 250 nm using a central wavelength of 800 nm and 50 fs pulses.

The creation of nanostructures inside a material has a wide field of applications from the building of gratings to 3D optical data storage devices.

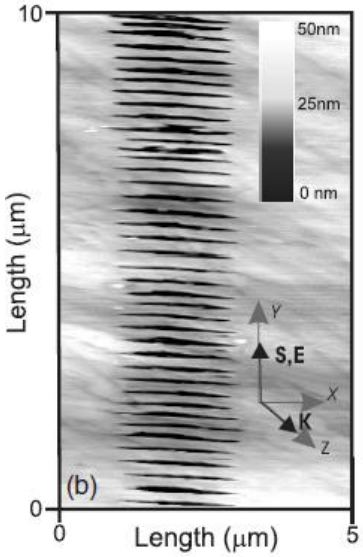

Figure 1.19: Formation of periodic nano-planes inside fused silica glass. S represents the direction the objective's focus was moved inside the fused silica glass, E is the polarization direction (linearly polarized light) and K is the wave-vector. Reprinted from [48]. ©2007 with permission from the Institute of Physics(IOP).

Chapter 2

Two-Photon Microscopy:Basic Principles, Performance and Advantages

2.1 Introduction

Two-photon microscopy (TPM) was developed by Denk *et al.* in 1990 [64] and proved to be a promising tool in imaging biological tissues. The use of short pulses and longer wavelengths, to excite and image in 3-D, gave microscopists the ability to image deeper into tissues than ever before. Furthermore, photodamage could now be kept to a minimum, within the focal volume, if not entirely eliminated. The invention of the two-photon microscope would forever open new opportunities in live imaging (*in vivo*) due to its negligible side effects on live cells.

2.2 Two-Photon Excitation Process: imaging biological specimens

To image a biological specimen in 3-dimensions, the samples are first tagged with fluorescent dyes. Each dye is chosen depending on the region of the cell to be imaged as different dyes inherently attach themselves to different regions. In conventional fluorescence microscopy, these dyes are typically excited by a 1-photon process with the excitation wavelength normally situated in the visible spectrum. For this research, the

process of excitation of the dye is dictated by the parameters of the microscope that was built. The excitation is pre-dominantly the result of a two-photon excitation process due to the characteristics of the laser used.

The process of exciting a single dye molecule with 2 photons is achieved by bringing the system from the ground state to the excited state via a virtual state [16]. As the first photon is absorbed, the system finds itself in an intermediate state which is not an allowed energy state of the molecule. At the same time, a second photon is absorbed bringing the system to the excited state. Once the dye molecule is in the excited state, it has a finite lifetime and eventually returns to the ground state releasing a photon of frequency $\approx 2\omega$ (figure 2.1) [6, 9, 10].

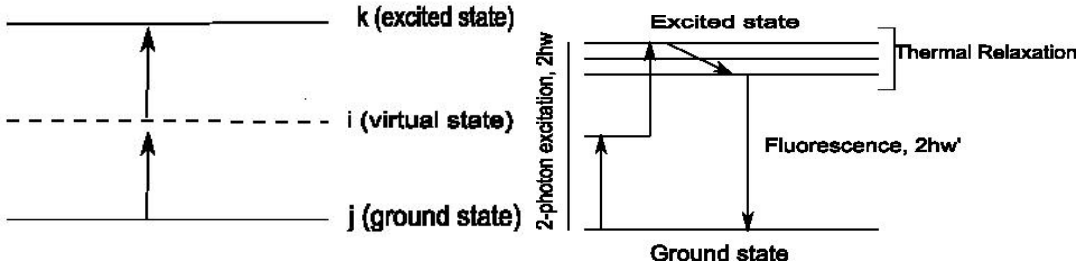

Figure 2.1: (left)2-photon excitation via an intermediate state, (right) the aborption of 2 photons of frequency ω and the release of a Stokes-shifted photon of frequency $\omega^{'} < 2$ ω due to thermal relaxation

The probability of observing such a process, σ, is determined by the molecule's cross-section for a 2-photon excitation, $\sigma_2(\lambda)$, which is in turn dependant on the wavelength and the intensity within the focal volume [5, 6].

$$\sigma = \sigma_2(\lambda)I^2 \tag{2.1}$$

From equation 2.1, we see that the probability of observing a 2-photon excitation has a quadratic dependance on intensity. It is safe to assume that the fluorescence intensity, $I_{fluorescence}$, caused by the 2-photon excitation process coming from the interaction region, is proportional to the probability of observing a 2-photon excitation.

$$I_{fluorescence} \approx \sigma_2(\lambda)I^2 \tag{2.2}$$

This relation can be expressed in terms of laser power, P.

$$I_{fluorescence} \approx \sigma_2(\lambda)(\frac{P}{A})^2 \tag{2.3}$$

where A is the area of the focus.

Equation 2.3 dictates that the emission from the 2-photon process falls off as A^{-2} (see Figure 2.2) when moving away from the focal point of the objective. This confines the interaction region to the focal volume [10, 20, 21, 65, 66] which is an analogue to the pinhole used in confocal microscopy (CM).

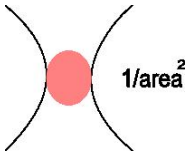

Figure 2.2: The confinement of the interaction region, in TPM, due to the quadratic dependance on intensity.

The mechanism of the two-photon microscope is identical to the confocal microscope. A pair of galvometric mirrors scans the focal plane in the xy direction by raster scanning the surface and repeats this process at different z position by moving the objective's focus to another focal plane. However, a confocal microscope uses pinholes to discriminate against out-of-focus information while the two-photon microscope takes advantage of the fact that information being collected is limited to the focal spot and hence there is no out-of-focus information from above and below the plane of interest [29, 67, 68]. Thus, the signal collected is limited to the focal spot enabling the collection of optical slices to build a 3-dimensional image.

2.3 Resolution

In microscopy, the definition of resolution is given as the minimum separation distance between two points where both can be separately distinguished. In optics, resolution is quantified in terms of contrast [69, 70].

The limit at which two points can still be distinguished is referred as the Rayleigh

criterion [71]. The Rayleigh criterion states that two points can be resolved if the first minimum of the first Airy disc (refer to the top of Figure 2.4) falls within the first central maximum of the second Airy disc (see Figure 2.3). The quantification of resolution corresponds, for the Rayleigh criterion, to a contrast of 26.4%. Two points are said to be distinguishable if their contrast is greater than 26.4% [69, 70].

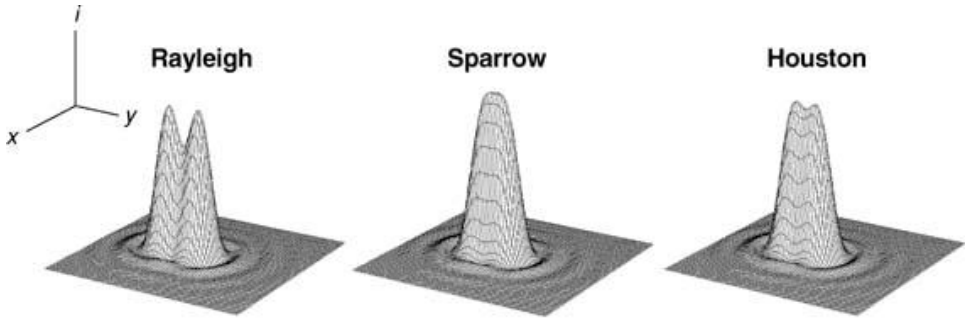

Figure 2.3: (left) Rayleigh criterion where two points are still distinguishable; (center,right) cases where points are no longer distinguishable.

Confocal and two-photon microscopes build point-by-point 3-dimensional images of the object under investigation. The selective process of rebuilding an image, point-by-point, can be achieved by different means. In the case of CM, it is achieved by the use of a pinhole to obtain information from a single point by discriminating the others. In TPM it is achieved by the confinement of the interaction region whose functionality is the same as using a pinhole. In both cases, the image quality depends on the observation and detection associated to each individual point. The detection of each individual point will not have a point at the detector but a blur or spread [26]. As a result, even the best optical system will not have the ability to image a point-like object as a point. Any detection from an optical system and the rebuilding of a point image is represented by what is called a Point Spread Function (PSF) [20, 26]. A PSF is a tool used to compare the performance of optical microscopes.

2.3.1 Point Spread Function

The mapping of the intensity distribution of a point in the image space is what characterizes the PSF (see Figure 2.4).

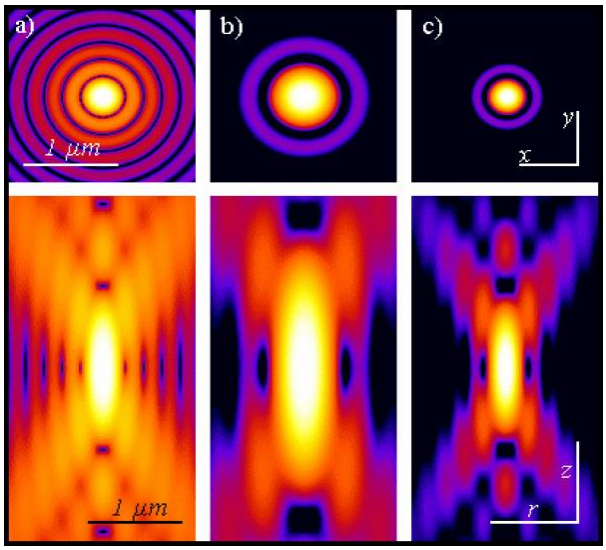

Figure 2.4: The intensity distribution along the lateral direction (top) and axial direction (bottom) of a point in (a)conventional fluorescence microscopy, (b) TPM, and (c) CM [72].

The PSF of any optical system was calculated by Born and Wolf [20] as

$$PSF = |h(u,v)|^2 = h(u,v)h^*(u,v) \tag{2.4}$$

where $h(u,v)$ is the amplitude of the PSF and describes the distribution of the light by an optical component.

This amplitude is given by [20, 69]

$$h(u,v) = -i\frac{2\pi n A \sin^2\phi}{\lambda} \exp^{\frac{iu}{\sin^2\phi}} \int_0^1 J_0(v\rho) \exp^{\frac{-iu\rho}{2}} \rho d\rho \tag{2.5}$$

The parameters v and u are the normalized optical units perpendicular and parallel to the optical axis, J_0 is the zeroth-Bessel function, n is the refractive index, $n\sin\phi$ is the numerical aperture, ρ is the normalized radial coordinate in the pupil plane, and A is the area of the aperture used in illumination or detection.

The quality of a point-like object in three dimensions is given by the total mapping intensity distribution, PSF_{total}, of each individual point at the detector. PSF_{total} is determined both by the point illumination (or illuminating beam path) in the object plane

and by the point detection (or detection beam path) [26]. This distribution is given by

$$PSF_{total}(x, y, z) = PSF_{ill}(x, y, z) \cdot PSF_{det}(x, y, z) \tag{2.6}$$

where PSF_{ill} and PSF_{det} are the intensity distributions of the point illumination and detection, respectively.

In the case of TPM, the illumination and detection beam paths are the same. PSF_{total} is thus governed only by the intensity distribution at the focal point and the confined interaction region. Focusing tighter decreases the size of the PSF_{total} and increases the resolution [22].

$$PSF_{total}(x, y, z) = (PSF_{ill}(x, y, z))^2 \tag{2.7}$$

In the case of CM the PSF_{total} is determined by the pinhole. PSF_{ill}, for CM, is extremely large due to the 1-photon excitation cross-section. The size is mainly governed by the wavelength and the NA of the objective which determines the spot size and confocal parameter. However, in contrast to TPM, CM has an advantage in the detection beam path due to the use of a pinhole. The pinhole size determines the intensity distribution of the PSF_{det} and it can be changed to achieve a better PSF_{total} [21, 26, 69, 73]. In CM, the PSF_{total} is the intensity distribution after the pinhole. Thus, the use of a pinhole to discriminate out-of-focus information makes it possible to obtain 3-dimensional images with good quality and makes PSF_{total} smaller than the PSF_{ill} illuminating the area [26].

$$PSF_{total} \leq PSF_{ill} \tag{2.8}$$

Theoretically, this makes CM superior to TPM when comparing illumination. However, the pinhole must be kept very small to compete with the resolution of TPM where the interaction is confined to a micron scale. The smaller the pinhole, the lesser the signal which results in the decrease of the signal-to-noise ratio of the system [74]. In both cases, the PSFs are strongly affected by the presence of aberrations in the illumination and detection beam paths as well as by light scattering inside the medium [36]. PSF_{ill} is strongly affected by the index mismatch between the immersion medium of the objective and that of the sample's medium (see later in the chapter). Furthermore, the effects of aberrations become worse with depth when imaging inside samples.

In TPM, the PSF_{total} is directly related to the confined interaction region since the probability of fluorescence has a quadratic dependance on intensity. This results in the

size of the PSF_{total} being extremely sensitive to aberrations [19, 69]. In CM, aberrations do not affect the PSF_{total} significantly since the pinhole limits the size of the interaction region.

For both microscopes, resolution is directly related to the full-width at half-maximum (FWHM) of the PSF_{total} in both the lateral and axial directions. Under ideal conditions with zero aberration, resolution from PSF_{total} in the lateral and axial distributions for the confocal microscope is given by [69, 70]

$$r_{xy,confocal} \approx \frac{0.4\lambda_{em}}{NA} \tag{2.9}$$

$$r_{z,confocal} \approx \frac{1.4\lambda_{em}n}{NA^2} \tag{2.10}$$

The lateral and axial resolutions obtainable by a two-photon microscope under ideal conditions are given by [20, 69]

$$r_{xy,two-photon} \approx \frac{0.7\lambda_{em}}{NA} \tag{2.11}$$

$$r_{z,two-photon} \approx \frac{2.3\lambda_{em}n}{NA^2} \tag{2.12}$$

where n is the refractive index of the medium, NA is the numerical aperture of the objective, and λ_{em} is the emission wavelength.

In principle, a confocal microscope may yield better resolution under ideal conditions but in practice, this is not the case. In CM, light scattering is pre-dominant and makes the detection of the scattered photons, from outside the plane-of-focus, a bigger issue. This causes the signal at the detector to become noisier. Decreasing the pinhole size can eliminate much of the scattered light but reduces the signal-to-noise ratio. In microscopy, noise significantly degrades the resolution of images [75, 74, 76]. To compensate for the decrease of signal-to-noise ratio, the laser power can be increased to achieve higher signal. However, this would most likely lead to photodamage of the object making it an unfeasible option. Therefore, the pinhole size must be optimized to strike a balance between high resolution and signal to noise ratio. In comparison, there is no out-of-focus fluorescence when using a two-photon microsope. Hence, all the emitted light is collected by the detector and is used to build the image. In effect, TPM achieves a better signal-to-noise ratio which is key to obtaining good resolution and depth discrimination[75, 74, 76]. Also, in TPM, the interaction region can be made even more confined by reducing the

light intensity since the probability of 2-photon fluorescence has a quadratic dependance on intensity. For these reasons, TPM yields much higher resolution in practice than CM.

Experimentally, the PSF of the two-photon microscope can be determined by placing a slab of transparent material under the microscope and focusing the light inside the bulk. Careful selection of the material is required so that the total energy needed to exceed the bandgap and photoionize the electrons is exactly a 2-photon excitation process. The light focused within the bulk creates a confined plasma that has a finite lifetime followed by a cool-down period during which permanent changes are made within the interaction volume. From the measurement of the dimensions of these modified regions, a good approximation of the axial and lateral extent of the PSF can be obtained.
Attempts have been made to indirectly determine the PSF of our two-photon microscope by ablating and internally modifying the polymer Poly(methyl methacrylate) (PMMA) which involves a 3-photon process.

2.3.2 Optical Sectioning

The construction of a 3-D image is done by first scanning the focal plane in the x-y directions with a pair of galvanometric mirrors and collecting the data, then displacing the objective's focus in the z-direction to another focal plane and repeating the procedure. This collection process is called optical sectioning (or depth-discrimination) (see Figure 2.5) [77, 69]. One can think of this as taking an onion and carefully removing one layer (one optical slice) at a time, taking a photograph, then stacking the photographs together to make a 3-dimensional image of the original onion.

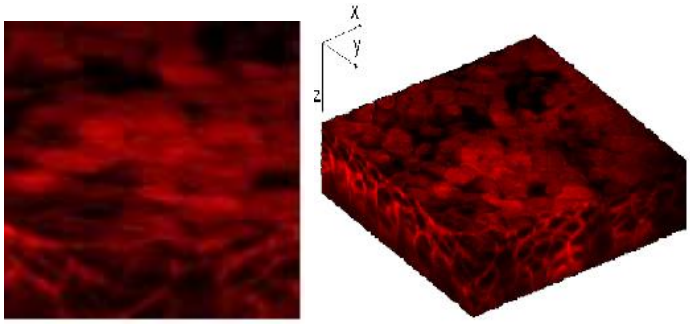

Figure 2.5: Image of (left) a single optical slice of tissue, (right) the resulting 3-D image from the projection of all individual slices. Reprinted with permisson from [78, 79]. ©2007 SPIE.

For CM, the thickness of these slices depends on the pinhole size. For TPM, is it determined by the axial dimension of the confined interaction region.

To describe optical sectioning under ideal conditions, the PSF_{total} are integrated over the lateral extent. This integral, as a function of depth, is given by [69, 77]

$$E_{(confocal)}(z) \approx \int_{r=0}^{r=\infty} PSF_{ill} PSF_{det} 2\pi r dr \tag{2.13}$$

$$E_{(two-photon)}(z) \approx \int_{r=0}^{r=\infty} PSF_{ill}^2 2\pi r dr \tag{2.14}$$

The equations demonstrate that the functions have a maximum in the focal plane. Cox *et al.* [77] explained this as the capability of the optical devices in achieving depth-discrimination. Under ideal conditions, the lateral resolution of CM is said to be better then TPM (see Figure 2.4) due to the use of shorter wavelengths and a sharper peak inside the medium. In practice, this is not true for the same reason as explained in the previous section. Due to its higher signal-to-noise ratio, TPM achieves higher performance in depth-discrimination.

2.3.3 Refractive Index Mismatching

In microscopy, biological samples are typically covered by a coverslip. The depth at which the objective is focusing is given by the separation between the coverslip and the tip of the objective. The medium within that spacing plays a critical role on the final outcome

of the image. It was shown by Hell *et al.* [19] that the refractive index mismatch between the immersion medium of the objective and that of the sample introduced a change in the actual focus position along the z-direction. The position in the absence of a mismatch is refered as the nominal focus position (NFP) and would be the expected z-position. The introduction of a mismatch between the media changes the actual focus position (AFP) of the objective by a fixed amount which is given by the ratio of the refractive indices of the immersion medium and the sample (see Figure 2.6) [19, 80].

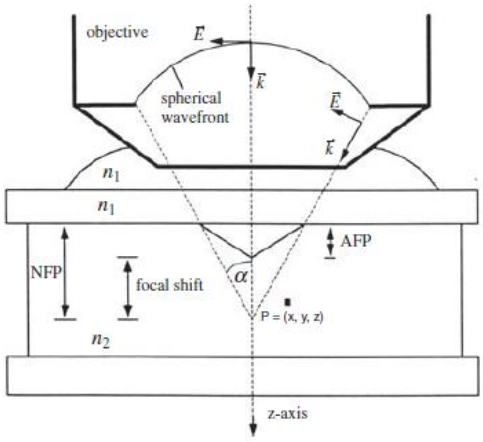

Figure 2.6: Effects of refractive index mismatch on the focus position upon entering a media with a different refractive index and the presence of spherical aberrations [19]. Reprinted with permission from John Wiley and Sons Ltd.

$$AFP = NFP\frac{n_1}{n_2} \tag{2.15}$$

where n_1 is the refractive index of the immersion medium of the objective and n_2 is the refractive index of the sample.

The mismatch of the media also introduces spherical aberrations because of the dependence of the focal length on the radial distance of the light rays (refer to figure 2.6) [19, 81, 80]. The effects of spherical aberrations, in an optical system, decrease as the ratio of indices approaches unity. The aberrations significantly broaden PSF_{ill} and lower the resolution (PSF_{total}) [26, 69]. The quadratic dependance on intensity and the absense of a pinhole in TPM makes it very sensitive to spherical aberrations [19]. The system design should be made to keep spherical aberrations to the minimum.

Figure 2.7 shows that using a water-dip objective, with its tip immersed in water, to image a water sample results in a PSF_{ill} that does not drastically change when going further down inside the sample (panels (a) and (b)). Comparatively, this is not the case when using an oil-dip objective. Due to a larger refractive index difference, PSF_{ill} is already broader at a depth of $z = 0$ (panel (c)) and broadens further with increasing depth (panel (d)). This becomes more problematic when imaging thick samples in water. The effects of PSF_{ill} broadening in CM result in the loss of signal going through the pinhole aperture. In the case of TPM, the broadening of the PSF_{ill} results in a lower local intensity and a larger interaction region which gives a lower fluorescence signal [19, 80].

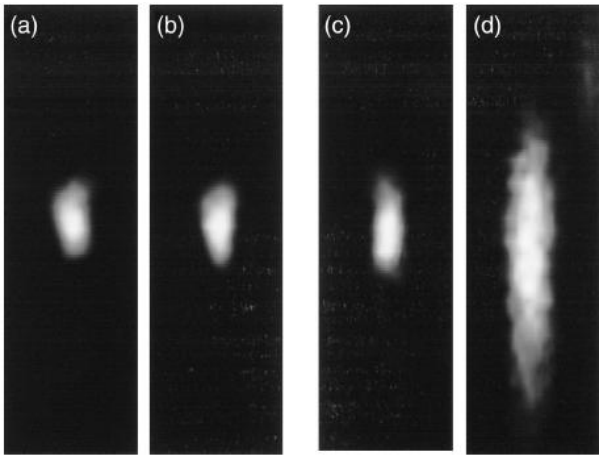

Figure 2.7: (a) and (b) are PSF measured using a water-dip objective upon imaging a water sample at (a) z = 0 and (b) z = 90 μm. (c) and (d) are PSF measured using an oil-dip objective upon imaging a water sample at (c) z = 0 and (d) z = 90 μm. Reprinted from [82]. ©1999 with permission from The Optical Society of America.

Intuitively, an oil-dip objective should provide less aberration and better resolution due to the refractive indices of oil and glass being closer than water and glass. However, experimental results demonstrated that matching the immersion medium of the objective to that of the sample yielded better results [82].

2.3.4 Effects of Group Velocity Dispersion

In multiphoton microscopy, only lasers capable of producing short, femtosecond pulses can efficiently produce multiphoton excitation in fluorescent dyes. This is simply because

the intensity delivered to the focal volume is extremely high, enabling the efficient process of 2-photon excitation of the dye molecules. The pulse duration and spectral bandwitdh of the laser are inversely proportional. Since the optical elements situated in the beam path are all made of glass (normal dispersive media), the refractive index will be slightly different for every spectral component of the pulse due to the wavelength dependence of the refractive index. As a result, the shorter wavelengths are blue-shifted and travel slower in the medium while the longer wavelengths are red-shifted and travel faster. This leads to a temporal broadening of the pulse and it is referred to as group-velocity dispersion (GVD) [13, 83, 84]. Thus, pulses travelling through optical elements are significantly broadened in time. This temporal broadening lowers the peak intensity in the focal volume which significantly reduces the multiphoton excitation efficiency, the PSF's intensities, and thus the resolution (see Figure 2.8). To counteract GVD, pulses can be pre-chirped before entering the optical elements which causes them to shorten as they propagate through the dispersive media due to negative dispersion. This method ensures the delivery of short pulses to the focal plane, resulting in higher intensities and better resolution (see Figure 2.8). In this work, no attempt has been made to pre-chirp the pulse and for 2 reasons. First, the laser oscillator in our laboratory is not used as a stand alone unit and is used to feed a regenerative amplifier. For this reason the pulses could not be chirped at the source (oscillator) without affecting the overall performance at the amplifier's output. Secondly, due to the low pulse energy at the output of the oscillator (5nJ) an exterior chirping arrangement would reduce the pulse energy delivered to the interaction region diminishing the fluorescence intensity.

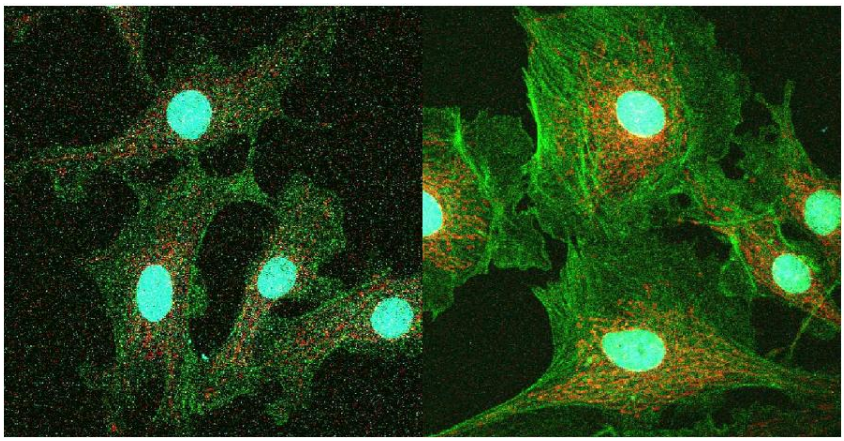

Figure 2.8: (Left) imaging of bovine endothelial cells without pre-chirping pulse; (Right) image of the same sample under the same conditions with a pre-chirped pulse (images taken from Olympus website)

2.3.5 Chromatic Aberration

Chromatic aberration, along the longitudinal direction, plays an important role in the loss of image quality. In the case of TPM, near-infrared light is used to excite the dye and the fluorescence is typically within the visible spectrum. Due to the refractive index difference of the optical elements for each frequency, the pathways to the focal spot are different for each wavelength and as a result, each wavelength arrives at a different focal plane within the focal volume. If not corrected for chromatic aberrations, the maximum collection of signal from the fluorescence is going to be located at a different focal plane than that of the central wavelength of the laser (see Figure 2.9).

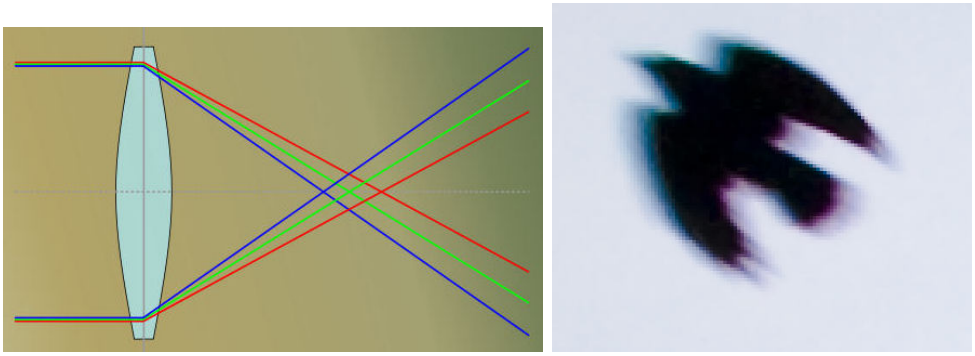

Figure 2.9: Demonstration of chromatic aberrations along the axial direction; (left) different wavelengths are focused at different focal planes within the focal volume[85]; (right) picture of a bird taken in the presence of chromatic aberrations [86].

In consequence, the collection of each emission comes from a different focal plane. This decreases the *NA* of the objective and thus, the signal collection. Furthermore, the light collected from these different focal planes will not be properly collimated at the back aperture (BA) and diverges. This introduces an aberration known as vignetting. Vignetting is the consequence of a series of optical elements shading the ones in front of them. This aberration results in gradual loss of light intensity from the center to the periphery (see Figure 2.10) [13].

Figure 2.10: Extreme case of an image quality when vignetting is introduced; the light intensity gradually diminishes from the center to the peripheries.

2.4 Advantages of TPM

Compared to other 3-dimensional microscopes, the two-photon microscope proves to have many advantages. The invention of TPM gave biologists the ability to study biological tissues *in vivo* and in their native environment without any influence to, and damage of the cell in the process. Previous fluorescence microscopes were shown to strongly affect the physical integrity of tissues. The use of longer wavelengths, in TPM, minimizes the effects of photodamage. Furthermore, the use of longer wavelengths makes TPM extremely efficient when imaging thick scattering media [87]. Moreover, the confinement of the interaction region can be used to do precise ablation inside biological samples. The combination of real-time imaging, the ability to focus onto a small region, and the use of fs light pulses that limit the thermal damage to the interaction region makes it a versatile tool [67, 88].

2.4.1 Scattering

The scattering of light inside a medium sets a limit on resolution and depth, when imaging a sample in 3-dimensions. It occurs when light enters an inhomogeneous medium and encounters impurities or other types of objects of various dimensions (eg. cells). The type of scattering is dependant on the size of the objects encountered by the light. Mie scattering occurs for objects greater or equal to the wavelength of light and Rayleigh scattering for objects smaller than the wavelength of light. The amount of light scattered from Rayleigh scattering has a fourth power dependance on the wavelength of light ($\propto 1/\lambda^4$) [13, 89, 37].

In microscopy, biological tissues are inhomogeneous and contain many scatterers of all shapes and sizes, demonstrating a strong wavelength dependance on the amount of light scattered. For this reason, the use of longer wavelengths results in less scattering when inside inhomogeneous media [78]. In addition, the use of longer wavelengths, short pulses, and high intensities (in TPM) enhances the number photons reaching the focus. This increases the probability of a 2-photon absorption and enables deeper imaging [87].

In the previous chapter, the fluorescence intensity for a 2-photon excitation in thick samples was given by:

$$F(t) = \frac{1}{2} g^{(2)} \phi \eta C \sigma_2 \langle P(t) \rangle^2 \frac{n_o \pi}{\lambda} \tag{2.16}$$

The fluorescence intensity was insensitive to the spot size and the total amount of fluorescence remained unchanged over the entire focal volume. Even if the emitted light is scattered, the collection and detection of this scattered light can still be used in rebuilding the image and thus, increases the detection efficiency. This property is well exploited in TPM and gives it an edge over confocal and other 3-D microscopes.

2.4.2 Photodamage

In Chapter 1, it was made clear that the use of shorter wavelengths for imaging was detrimental to the viability and physical integrity of the biological samples. Thus the use of a near-IR laser as the excitation source in TPM dramatically decreases the chances of photodamage to the tissues due to the wavelength dependance of each photodamage process (photobleaching, phototoxicity, photochemical damage). However, photodamage may still occur but, due to the confinement of the interaction region, the photodamage is limited to the focal volume leaving the surrounding regions untouched [66, 88].

Nonlinear Photodamage

The use of longer wavelengths and short pulses, in TPM, has been widely accepted to significantly reduce photodamage in biological tissues. However, recent studies have demonstrated that the use of lasers in the near-IR, capable of delivering fs pulses, inflicted new types of photodamage by nonlinear interactions with the sample [90].

These recent studies showed lysis in tissues with the use of short pulses in the 100-300 fs range [90, 91, 92, 93, 94]. Lysis of tissues is a process that compromises the physical integrity of the cell and is described as the physical breakdown of the cell itself. Koester et al. [95] demonstrated that, for fs pulses in the near-IR with powers exceeding 10 mW, cells would start to lyse and divide. Experiments on bovine adrenal chromafin cells by Hopt *et al.* [90] showed an increase in photodamage with each succesive scan when increasing the power delivered to the focal plane and the lowering of the photodamage threshold as a function of pulse width (shown in figure 2.11).

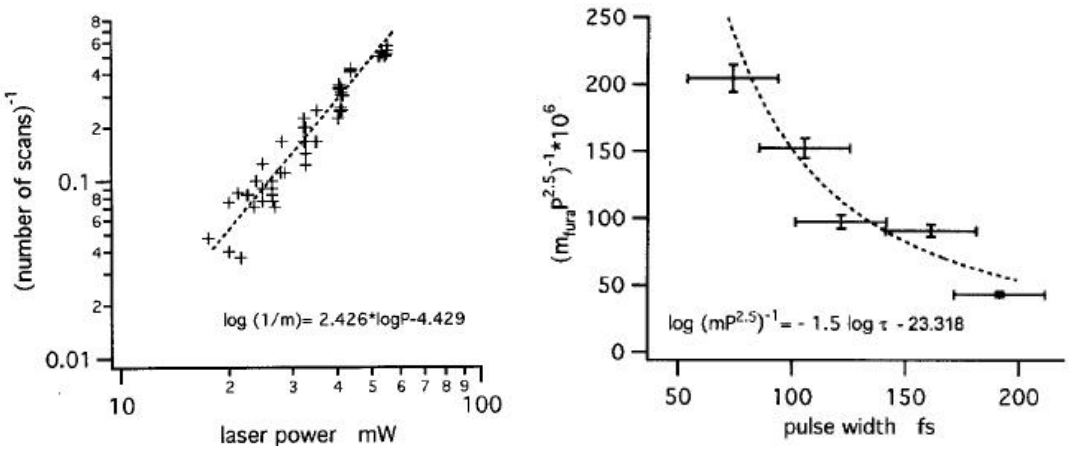

Figure 2.11: (left) Shows the increase in photodamage per scan when increasing the power at the focal volume. (right) Shows photodamage thresholds as a function of pulse duration. Demonstrating an increase in the photodamage threshold as the pulse duration get shorter. Reprinted from [90]. © 2001 with permission from Elsevier.

Other experiments by Konig *et al.* [91, 92, 93, 94] on the cloning efficiency of Chinese hamster ovary cells showed that the cloning efficiency of the cells remained unchanged for laser powers lower than 1 mW in the focal plane. Upon reaching powers of 6 mW and higher, the cells were no longer able to form clones. Further analysis showed the creation of a large population of dead cells for powers exceeding 10 mW [90]. These observations were explained by the possible increase in probability for 3-photon absorption by the biological tissues. Typically, the wavelengths used in two-photon microscopy are situated between 800-900 nm with 3-photon absorption corresponding to the absorption in the 200-300 nm range. Cellular DNA and proteins are well known to be highly absorbent within that range [34] and it would explain the increasing number of dead cells by apoptosis (i.e. events leading to characteristic cell changes followed by the death of the cell) [96]. To eliminate this effect, the power should not exceed 10 mW. This limitation on the power does not significantly change the resolution since even at these powers, the signal-to-noise ratio is still extremely good.

2.4.3 Simultaneous Excitation of Multiple Dyes

As previously explained in this chapter, different dyes inherently attach themselves to different sections of the tissue. In the 1-photon case, the excitation source must match

the excitation wavelength specific to each dye. The need to change the excitation source to image different parts of the sample increases the total exposure time needed to fully image it. During this exposure time, the samples have an increasing chance of suffering photodamage.

The use of pulsed lasers in TPM will excite all dyes simulaneously within the visible spectrum located within the focal volume. With the correct sets of filters and detectors, the simultaneous emissions of the dyes can be collected and used to image different parts of the biological sample. This limits the exposure time significantly[74, 75, 76].

Fluorescence intensity is proportional to the probability of the 2-photon excitation and depends both on the molecular cross-section, $\sigma_2(\lambda)$ [5, 6], and the intensity within the focal volume (see equation 1.9). This relation holds true for every dye situated within the focal volume. The only difference comes from the value of $\sigma_2(\lambda)$, which is specific to each dye for a certain wavelength. Hence, all dyes within the focal volume will be excited but the emitted intensity depends on the value of $\sigma_2(\lambda)$. This factor can be controlled by the concentration of each dye tagged to the sample.

2.4.4 Ablation and Thermal Damage

The ability of TPM to both image and have the freedom to perform ablation has proved to be a promising tool in biological studies. When imaging or ionizing, the time scale of energy transfer to the lattice by heat or collision is on the order of a few ps [14]. Therefore, for pulses shorter than this time scale (in our case, fs pulses), no energy is transferred outside the focal volume to the surrounding regions. Thermal damage from imaging (or by optical breakdown) is spacially contained to the focal volume, leaving the surrounding regions untouched. This ensures the viability and physical integrity of the surrounding cells [67, 88].

Chapter 3

Two-Photon Microscopy:Design and Implementation

3.1 Introduction

The goal of this project is to design, build, and test a system capable of nano-manipulation of soft matter. The requirements of this system were a) to have the ability to image biological tissues in their native environment, and b) to have the freedom to do precise material ablation without damaging the surrounding regions. The system built to meet these requirements is a multiphoton microscope.

The design aesthetics of the multiphoton microscope are original. Its constraints and criteria are based on previously built multiphoton microscopes developed by other research groups[97, 98, 99, 100]. The multiphoton microscope is designed to meet these criteria in order to minimize aberrations, to improve resolution, to increase the collection efficiency of the emitted signals, and to obtain optimal performance.

3.2 Laser System

The excitation source used for this research is a Kerr lens mode-locked Ti:sapphire laser (Spectra-Physics Tsunami) pumped by a 5 W Nd:YVO_4 diode solid-state laser (Spectra-Physics Millenia, $\lambda = 532$ nm, M^2 1.1). The system produces sub-30 fs pulses, with 8 nJ of energy, a central wavelength of 800 nm, and at a repetition rate of 76 MHz.

3.3 Experimental Setup

The setup (as shown in Figure 3.1) demonstrates the placement of components and optical elements in the beam path of the multiphoton microscope. The functionality of each component is explained below as well as its design criteria.

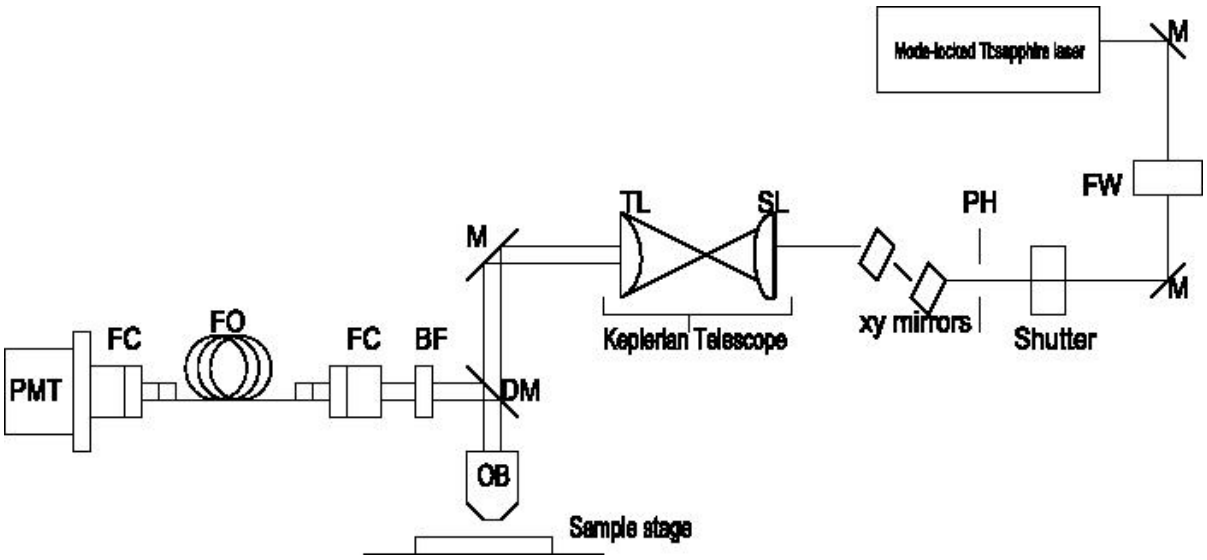

Figure 3.1: Multiphoton microscope setup consisting of plane mirrors (M, r = 97.5%), filter wheel (FW), shutter, pinholes (PH), galvanometric xy mirrors, a Keplerian telescope composed of a scan lens (SL, f = 5 cm) and a tube lens (TL, f = 15 cm), dichroic mirror (DM, t $\geq$ 85% and r $\geq$ 85%), microscope objective (OB), bandpass filter (BP), fibre collimators (FC), fibre optic (FO) cable and a photomultiplier tube (PMT)

In multiphoton microscopy, two different setups can be used. The first is the descanned mode where the emitted light travels to the detector using the same optical pathway as the laser beam used to excite the dye molecules. The descanned mode captures the emitted light using the galvanometric mirrors. This increases the optical elements located between the emitted light and the detector and fails to correct for chromatic aberration. Furthermore, the use of galvanometric mirrors to direct the emitted light into the detector introduces astigmatism due to the off-axis collection of the light, affecting the overall image quality. The second setup, which is the one used in this design, is the non-descanned mode. This setup optimizes the optical pathway by minimizing the amount of optical elements encountered by the emitted light and ensures maximum fluorescence intensity at the detector. This method increases the collection efficiency of the microscope and is done by placing a dichroic mirror, at 45°, directly in front of the objective's back aperture (Figure 3.1). The emitted light collected by the objective is then reflected by the dichroic mirror into the detector. No astigmatism is introduced since the galvanometric mirrors are not used to collect the emitted light.

3.4 Optical Design of the Multiphoton Microscope

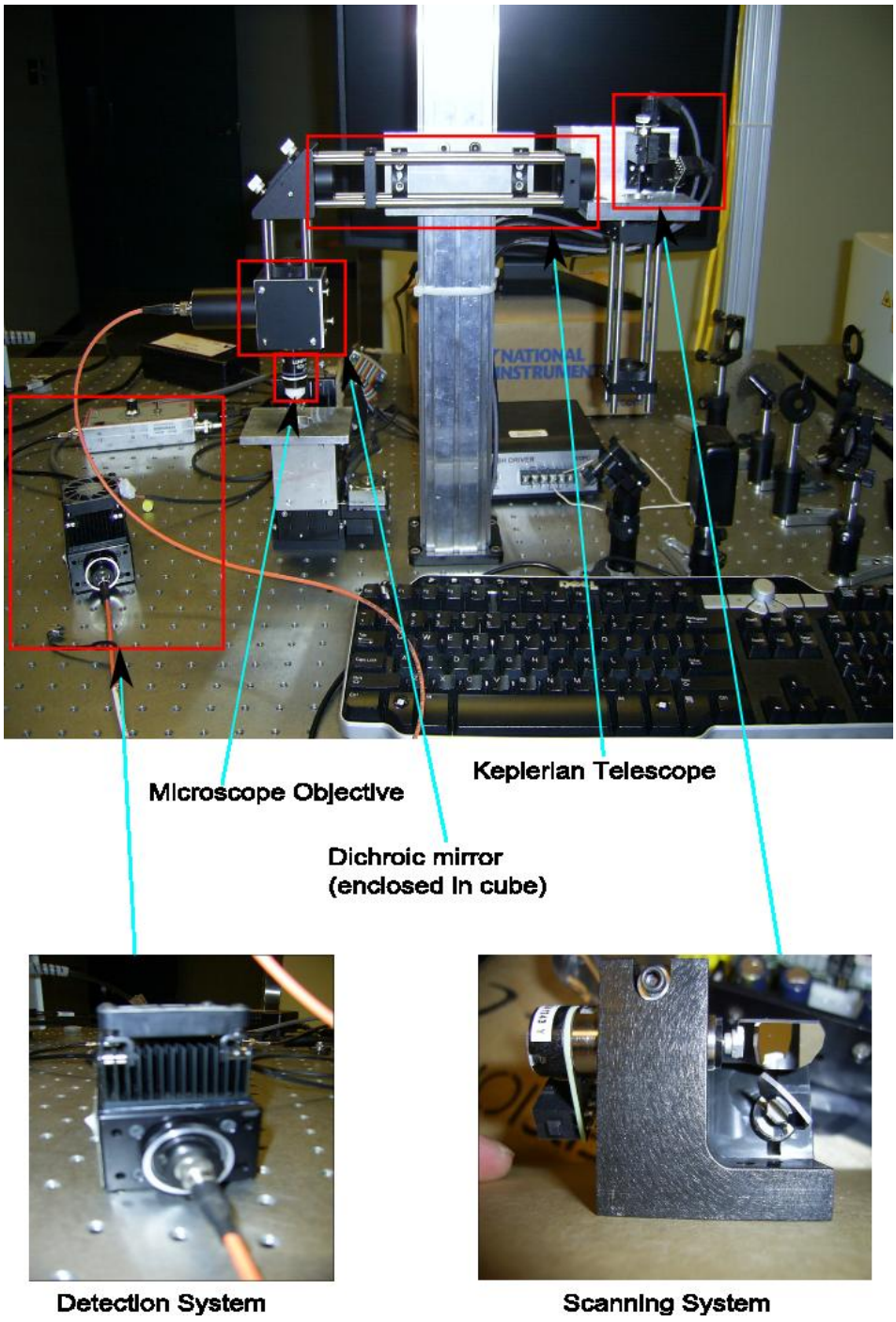

Figure 3.2: The Multiphoton Microscope

In our design, the light from the oscillator first passes through a gradient neutral density filter to control the intensity delivered to the focal plane. This control on the intensity enables imaging and the subsequent ablation of specific locations. A shutter (EOPC, SH-10) with a 15 msec response time is used to block the light beam. It is timed with the data acquisition process to block the light in between the repositioning of the objective's focus in the z-direction from the previously imaged focal plane onto a new one. The light is then directed into the scanning system of the microscope (see Figure 3.2). The scanning system consists of two orthogonal mirrors mounted on galvomagnetic motors which deflects the laser beam in the x and y direction. The amount of deflection being proportional to the voltage applied to the galvo's (discussed further below). The light entering the scanning system is deflected at large angles by the scanning motion of the galvanometric mirrors. A Keplerian telescope is used to collimate and expand the beam onto the back aperture of the objective. The beam is then transmitted through a dichroic mirror (Newport, 10CMR-45) onto the back aperture (BA) of the objectives (Olympus, 10-20-40x dry and 60x waterdip). The light is then focused onto the focal plane of the objective where each layer of the sample is raster scanned in a z pattern by the galvanometric mirrors. The deflection angle of the mirrors is related to a specific position in the focal plane. The emission from each of the individual points located in the focal plane are epicollected by the microscope objective and reflected by the dichroic mirror into the detection system. The objective is then moved to another focal plane. The process is repeated for every layer of the sample. The information of each individual point from all layers are stored onto the computer memory from which the image can be fully reconstructed [97].

3.4.1 Scanning System

The scanning system (refer to Figure 3.2) of the multiphoton microscope is composed of 6 mm diameter x-y mirrors mounted on galvo scanners to raster scan the laser beam onto the BA of the objective. The galvanometric mirrors are controlled by a micromax servo driver amplifier (Cambridge-Technology, 673xx dual axis servo driver). It is connected to the breakout box (National Instruments, BNC-2090A) where it receives a ± 10 V analog position command from the data acquisition (DAQ) card (National Instrument, PCI-6110E) to move the mirrors in a raster scan pattern. This analog position command corresponds to a $\pm 10^\circ$ rotation of the mirror shafts and an optical scan movement of $\pm 20^\circ$. The maximum rotation angle is 40° for each mirror. Corresponding to 0.5V per

optical degree. The mirrors are controlled by the DAQ card which communicates with the software, sending a sinusoidal signal to the fast scanning mirror (rapidly varying the voltage making the mirror scan in a line) and a canonical waveform with step intervals to the slow scanning mirror (changing lines for the fast mirror). Scan rates of up to 1.7 kHz are feasible at reduced deflection angles. This method allows the raster of the laser beam in the focal plane and along with the relay optics consisting of a scan and tube lens, ensures the light remains parallel to the optical axis.

3.4.2 Keplerian Telescope and Beam Expansion

The design employs an infinity corrected objective to deliver the light onto the focal plane. The use of an infinity corrected objective requires that the laser beam be collimated upon entering the back aperture of the objective [97]. The use of a collimated beam minimizes the presence of spherical aberrations and eliminates vignetting conditions. Furthermore, to obtain maximum fluorescence emissions, the expanded beam should slightly overfill the BA of the objective in order to have a gaussian beam profile at the focus and therefore, the smallest excitation area [13, 101]. To meet these requirements, a Keplerian telescope was designed (refer to Figure 3.2). The Keplerian telescope permits any sample to be scanned without having to mechanically move it on a stage. It is composed of 2 achromatic doublet lenses (to eliminate chromatic aberrations), a scan lens, and a tube lens. The scan lens (Thorlabs, ACN254-050-B, f = 50 mm) is placed in front of the galvometric mirrors where it focuses the light diverging by the scanning motion of the mirrors. The tube lens (Thorlabs, ACN254-150-B, f = 150 mm) is placed such that its focus is at the focus of the scan lens. This lens combination collimates the light into the back aperture of the objective and enables the scanning of the sample in the x-y directions. The objective then converts this incident angle into a diffraction limited spot position in the focal plane, as shown in Figure 3.3.

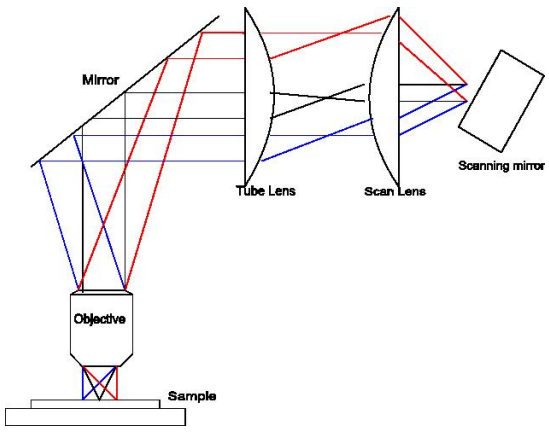

Figure 3.3: Keplerian telescope

Constraints

To design the Keplerian telescope, some constaints had to be satisfied in order to optimize performance and minimize aberration[97].

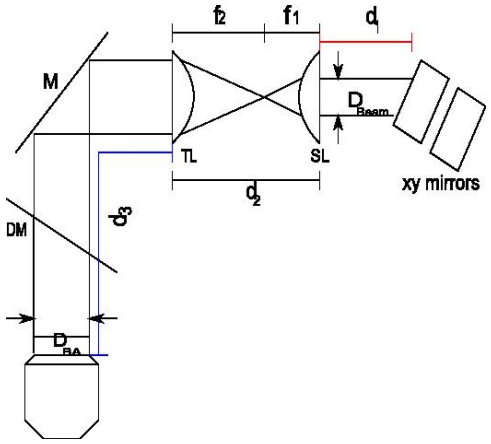

Figure 3.4: Parameters in designing a Keplerian telescope: d_1 is the distance seperating the scan lens and xy mirrors, f_1 is the scan lens focal length, f_2 is the tube lens focal length, d_3 is the distance between the tube lens and the back aperture (BA) of the microscope objective, D_{beam} is the beam diameter of the excitation source and D_{BA} is the diameter of the BA of the microscope objective. The optical elements located within the beam path: tube lens (TL), scan lens (SL), mirror (M) and dichroic mirror (DM).

1. The use of an infinity corrected objective on the setup requires that the light be collimated at the back aperture of the objective. For the light to be properly collimated, the distance between the scan and tube lens should be the sum of both focal lengths.
$$d_2 = f_1 + f_2 \tag{3.1}$$

2. To ensure that the intensity delivered to the focal plane is the same for all the mirror angles, the scan lens should have the light coming through its center when the scan mirrors are at their rest positions. Similarly at the same rest position, the light should enter the back aperture of the objective in its center.

3. The distance of the scan lens from the scanning mirrors is determined by the following relation
$$d_1 = \frac{(f_1)^2}{f_2} + f_1 - d_3(\frac{f_1}{f_2})^2 \tag{3.2}$$
where d_1 is the distance required to maintain a constant laser power at the back aperture of the objective during the scanning motion of the mirrors (refer to figure 3.4).

4. The laser beam should slightly overfill the back aperture of the objective to ensure a gaussian beam profile at the focus in order to achieve the highest power and resolution. The magnification that meets this condition is calculated by the ratio of the diameter of the back aperture to the diameter of the laser beam.
$$|m| = \frac{D_{BA}}{D_{laser}} \tag{3.3}$$

5. The focal lengths of the lenses must satisfy these constraints and give the appropriate magnification given by the following relation
$$|m| = \frac{f_2}{f_1} \tag{3.4}$$

Meeting the Constraints

The diameter of the laser beam from the oscillator is 3 mm and the back aperture of the objective used is 9 mm. Therefore, from equation 3.3, the magnification of the beam had

to be 3. Hence, the ratio of the focal lengths for the scan and tube lens had to be 3 as well.

$$3 = \frac{f_2}{f_1} \tag{3.5}$$

This ratio is satisfied by choosing f_1 to be 50 mm and f_2 to be 150 mm. The lenses were chosen to be achromatic doublets to minimize aberrations and were anti-reflection (AR) coated for maximum infrared transmission.

The scan lens distance, from the x-y mirrors, was determined by equation 3.2. Since f_1 and f_2 were fixed, d_1 depended solely on d_3, the separation between the tube lens and the BA. In order to select both distances, a graph of d_1 versus d_3 was plotted.

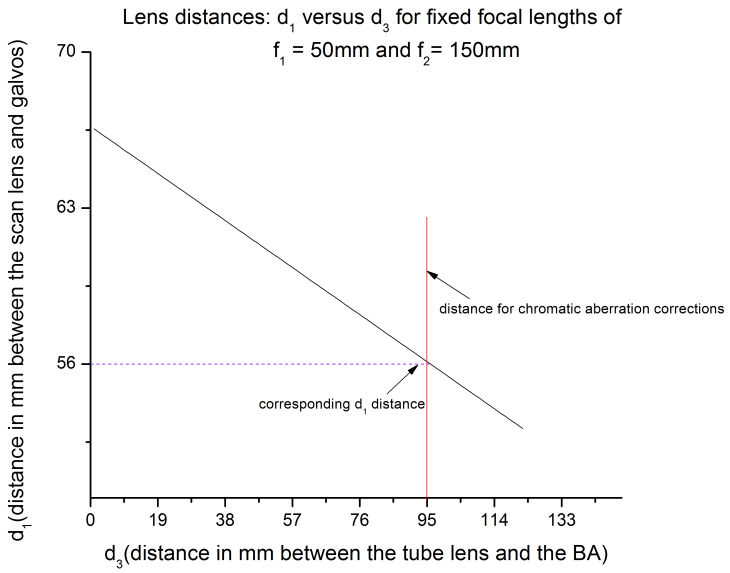

Figure 3.5: Lens distances

Since typical objectives are corrected for chromatic aberrations up to 95 mm, d_3 was chosen to be 95 mm leaving d_1 to take the value of 56 mm [97]. The system was built to satisfy all of these pre-determined parameters.

3.4.3 Microscope Objectives

In two-photon microscopy, the objective is used both to deliver the laser beam and collect the emitted light. This process of excitation is commonly known as epi-fluorescence [64].

Although multiphoton microscopy yields much better resolution and can image deeper than its counter-part, the confocal microscope, brightness or signal is always a problem since the fluorescence intensity coming from the excited region is much lower. For this reason, the objective must be carefully choosen for maximum performance and signal detection. To achieve maximum light collection, the objective's performance depends critically on two factors. It depends firstly on the numerical aperture (NA) of the objective; the higher the NA, the higher the collection of emitted light. Secondly, it also depends on the immersion medium of the objective [13, 25].

It is commonly thought that it is more beneficial to use an objective with the highest NA since it gives better resolution and signal collection efficiency. While this is technically true, the use of a high NA objective comes at the cost of reducing the working distance [13] which restricts its ability to image thick samples. Therefore, a balance had to be made so it was chosen to use an objective with a good NA and decent working distance (Olympus 60x waterdip objective, plan fluor, 3 mm working distance).

In multiphoton microscopy the objective has a very wide spectrum of light going through its optical elements and so the objectives chosen for this design were **plan fluor** objectives due to their high transmission within the visible to the infra-red (IR) spectrum [13].

Infinity Corrected Objectives

The use of near-IR light for the 2-photon excitation process and the collection of emission located in the visible spectrum requires by default, the use of an infinity corrected objective.

The term infinity-correction refers to the objectives' ability to collimate both the infrared and visible light [34, 102]. However, these are only corrected for chromatic aberrations up to a short distance. Also, when an off-axis system is used to scan the sample, comatic aberrations are introduced in the system. However, it was shown that using a collimated beam with an infinity corrected objective eliminated comatic aberrations entirely while minizing spherical aberrations [97]. Therefore, the use of a Keplerian telescope in combination with the infinity corrected objective was chosen for our microscope design.

Immersion Objectives

The immersion medium of the objective plays a significant role in the resolution and detection of the signal. Refractive index mismatch between the immersion medium of the objective and the sample's medium introduces spherical aberrations and results in severe reduction of the fluorescence intensity produced within the interaction region [13, 80, 87]. Therefore, matching the medium between the objective's tip and that of the sample is essential. Since the microscope was built to image biological tissues which are mostly composed of water, we chose to use a waterdip objective.

Magnification

In multiphoton microscopy, the fluorescence intensity coming from the interaction region is very low. Therefore the light emitted from the excitation of the dye molecules must be efficiently collected by the objective in order to have a good signal and better image quality.

The light gathering power of an objective used in epi-fluorescence, F_{epi}, is given by

$$F_{epi} = 10^4(\frac{NA^2}{M})^2 \tag{3.6}$$

where NA is the numeral aperture and M is the magnification of the microscope objective.

Light gathering power increases significantly for higher NA and lower magnification. For this reason, we chose a 40x objective with an NA of 0.75 and a 60x objective with an NA 0.90 in order to optimize the light gathering power of the objective.

3.4.4 Dichroic Mirror

A dichroic mirror placed at 45° is used in front of the objective's BA to reflect the emitted light collected by the objective into the detector. This eliminates the use of the galvanometric mirrors to collect the emitted light (descanned mode) as well as preventing the light from travelling through other optical elements like the Keplerian telescope and therefore increases the collection efficiency of the microscope. For maximum performance and efficiency, the dichroic mirror was chosen to transmit light in the near-IR in order to deliver the light onto the sample, and be highly reflective in the visible spectrum to efficiently reflect the emitted light to the detector.

The dichroic mirror has the following characteristics:

Type	**Wavelength**	**Reflectivity and Transmission**	**Angle of incidence**
Cold mirror	400-700 nm	$R_{avg} \geq 95\%$	$45° \pm 5°$
	780-1250 nm	$T_{avg} \geq 85\%$	
	850-2500 nm	$T_{avg} \geq 80\%$	

3.4.5 Detection System

Since the fluorescence signal is very low, the collection and detection efficiency must be optimal. In our design, the light reflected from the dichroic mirror is first passed through a bandpass filter (Newport, BG-40) to prevent back scattered light from being gathered and detected. The light is then focused into a multimode fibre (OZ Optics, UV/visible , 250 μm core) by a fibre collimator (Thorlabs, F810FC-543). The choice of incorporating a fibre into the detection system design is due to their low loss while carrying a signal over a great distance. A second collimator (Thorlabs, F240FC-A) at the ouput of the fibre collimates the beam onto the PMT (Hamamatsu, H7422P-40) (refer to Figures 3.1, 3.2). Since the photocathode is located at a distance of 16.3 mm from the entrance of the PMT, the absence of a fibre collimator would result in signal being lost due to the finite size of the detection area. The effective focal length of the second collimator is 7.86 mm and produces an output $1/e^2$ diameter of 1.5 mm. The photocathode has an effective diameter of 5 mm.

Chromatic Aberration and Vignetting

By industry standard, infinity corrected objectives are corrected for chromatic aberration up to a distance of 95 mm [97]. Chromatic aberration is a common problem in multiphoton microscopy since the objective has a wide range of wavelengths passing through its optical elements. Chromatic aberrations occur when the wavelength used for excitation is far away from the emitted light. Since the focus of an objective depends on the wavelength of light, if not corrected, aberrations will result in the collection of the emitted light by the objective to be at different focal planes [13, 97]. This is known

as longitudinal chromatic aberration (or focal plane mismatch) and results in the loss of signal and overall reduction in the system performance. The second problem arising from the wide spectrum of light going through the objective's optical elements is that the light collected from the focal planes is not being collimated at the BA but instead diverges, leading to vignetting [97].
For this reason, the tube lens and fibre collimator were both placed at a distance of 95 mm from the BA, as shown in figure 3.5.

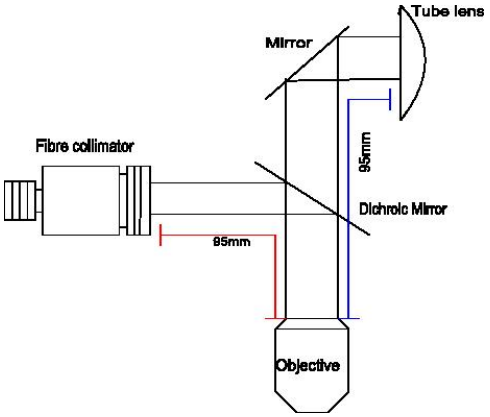

Figure 3.6: Optical setup in order to correct for chromatic aberration and vignetting.

3.5 Mechanical Design

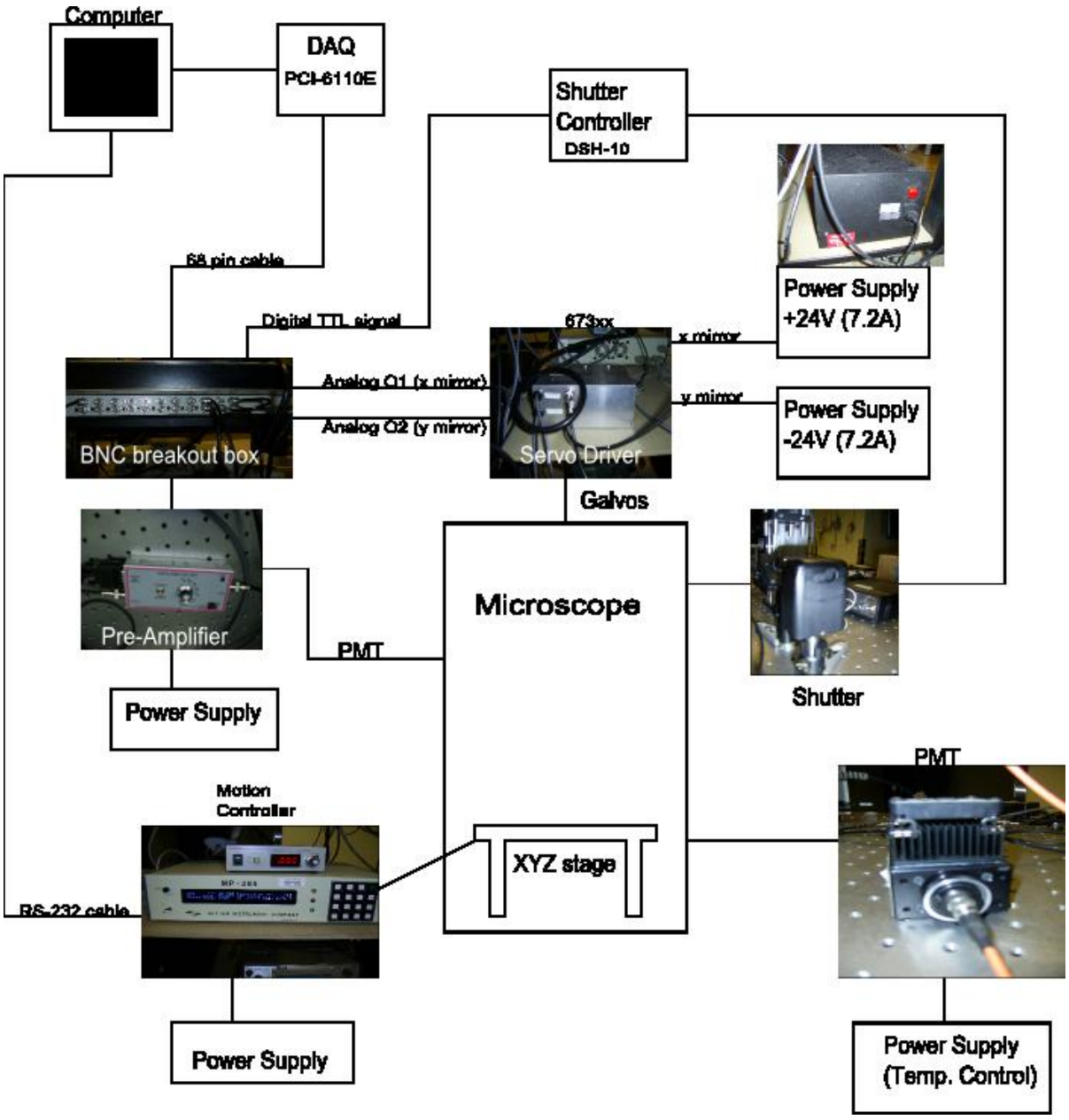

Figure 3.7: Mechanical schematic of the multiphoton microscope setup

3.5.1 Photomultiplier Tube and Pre-Amp

The PMT (Hamamatsu, H7422P-40) was chosen for its wide spectral response (from 300-720 nm), high sensitivity, and its relatively small size. In addition, the PMT has a quick response of roughly 1 ns rise time. This makes for the rapid collection of data which optimizes 3D image quality. The PMT has an adjustable gain to optimize the performance of the detector and it is temperature controlled to limit noise (refer to Figure 3.7).

When light strikes the photocathode of the PMT, photoelectrons are released which are then multiplied by striking a series of dynodes, exponentially increasing the number of electrons. A maximum current pulse of 2 μA is produced at the PMT output. The output from the PMT is fed into a preamplifier (Advanced Research Instruments Corporation, PMT-4V3, adjustable gain) that converts the current into a voltage signal output. The output from the preamplifier goes to the DAQ card to acquire the voltage signal and to process the collected data.

Multiple constraints were made on the selection of the current-to-voltage amplifier in this design. Since the DAQ card requires a $\pm$10 V input signal for optimal performance, the output of the preamplifier should be within this range. Second, the gain of the amplifier had to be adjustable in order to maximize the quality of the signal. Third, it should have a good signal-to-noise ratio. To satisfy these conditions, the current-to-voltage amplifier chosen was the PMT-4-V3 from Advanced Research Instruments.

3.5.2 Scanners Servo Driver

The servo driver responsible for the movement of the galvanometric mirrors can heat up extremely fast when the mirrors are continuously raster scanning. To dissipate the heat, the servo driver was mounted on an aluminum block which acted as a heatsink.
The servo obtained from Cambridge Technologies requires a $\pm$24 V, 7.2 A power source. To satisfy this requirement, a power supply was home-built and wired directly to the servo driver. For optimal performance, the power supply and servo driver were enclosed in perforated chassis along with a cooling fan. Moreover, to receive the analog command (to move to mirrors) from the DAQ card via the breakout box, wires were soldered to the servo's analog command input connections and made into BNC input connectors at the front of the box containing the servo (refer to Figure 3.7).

3.5.3 Z-stage Integration

The z-stage works in unity with the objective in order to achieve optical sectioning. The thickness of the slices depends on both the axial extent of the focus (confocal parameter) and the step size of the stage. We chose motion controlled stages from Sutter Instruments (Sutter Instruments, MP-285) which communicates directly with the software via a serial port connection (refer to figure 3.7). Since the resolution of the stage is of 200 nm in all directions, it is smaller than the confocal parameter and therefore the thickness of the slices is essentially limited by the confocal parameter.

The XYZ stage was custom-built for independant axis movement in all three directions and came equipped with a rotary optical encoder (ROE) to move each individual axis separately. The ROE allows the displacement of the stage in all three directions to locate a region of interest or surface before initiating a scan.

3.5.4 Shutter

The shutter was placed in the beam path in order to protect the samples from suffering heat damage and from overexposure to the excitation source. The shutter controller (EOPC, DSH-10) communicates with the DAQ card via a breakout box receiving a transistor-transistor logic (TTL) digital signal (refer to Figure 3.7). Since overexposure to near-IR wavelength can eventually kill the cells when imaging *in vivo*, it is therefore crucial that the exposure time of the sample to the excitation source be kept to a minimum.

3.5.5 Data Acquisition and Communication

The data acquisition card (National Instruments, PCI-6110E) is responsible for sending all the signals to each individual component and acquiring all the information to be processed. The DAQ card is connected to a BNC box (National Instrument, BNC-2090A) via a 68 pin connector. The BNC box breaks up all the digital/analog outputs or inputs of the DAQ card into individual BNC connectors that are connected to the components in order to give commands or receive data. All communications to and from the computer is done through this DAQ card with each channel sampling at a rate of 5 Ms/s per channel.

3.6 MPScope

The software responsible for controlling the components and enabling the reproduction of the 3D images was graciously provided by the Kleinfeld labs and our contact, Dr. Quoc-Thang Nguyen. It is called MPScope.

The mechanical functioning of a multiphoton microscope is very complex due to the number of components that need to be simultaneously controlled. The software is responsible for the order in which each of the processes are executed, communicating directly to the DAQ card or by serial port to the XYZ stage. It is also responsible for gathering the information collected from each point during the scan and saving them on the computer to produce an output file. It is important to note that even though MPScope gathers the information from each layer, it does not build a 3D representation of the original image. The output files are movies of the scans with each layer being a frame in the movie. Therefore, to rebuild the 3D representation of the object, the frames of the movie are exported as a multi-Tiff image file where all frames are separated into individual pictures. The multi-Tiff image files are then opened by the ImageJ software where they are z-projected by stacking the frames on top of each other to create a 3D replica of the original object.

MPScope offers many modes to scan the samples as well as giving the flexibility of setting parameters in order to increase the system's performance. Throughout the experiments conducted with the multiphoton microscope, only two modes were used: movie mode and stack mode. In movie mode, the sample is imaged in realtime and gives the user the freedom of displacing the objective's focus in all three directions. This is good to find the regions of interest. On the down side, there is no frame averaging which can make the image noisy. In stack mode, the region of interest is imaged in 3D by successively raster scanning each optical layer and storing them in the computer's memory. Before each scan, the number of sections and the distance (interval) between them must be selected. This action results in the objective's focus being lowered into the sample by the interval chosen and repeated for the number of sections selected. The advantage of using stack mode is that there is the option of averaging frames as the sample is being scanned which is a good way of filtering out noise, resulting in better quality images.

3.6.1 Mirror deflection angle

The multiphoton microscope was designed to be compact and easily transportable. For this reason, the scan and tube lens were chosen to have a 1-inch diameter. The default setting in MPScope gives a ±2.5 V analog voltage command to the galvos corresponding to a total rotation angle of 10° by the mirrors. In this setting, the light was observed to be clipped by the lens holders and failed to enter the tube lens. Therefore to prevent the clipping of the beam, the deflection angle of the mirrors was changed in the software by lowering the analog voltage command given to the mirrors. The analog signal was reduced to ±0.9 V, corresponding to a total rotation angle of 3.6°.

3.6.2 Image duplication and pixel offset

During the first test, images seen by the multiphoton microscope appeared to be duplicated. This was found to be the result of an improper pixel offset adjustment in the sofware which resulted in the misalignment of the pixels on the computer screen (see Figure 3.8). This occurred when the lag between the actual position of the mirrors and the voltage command remained uncompensated.

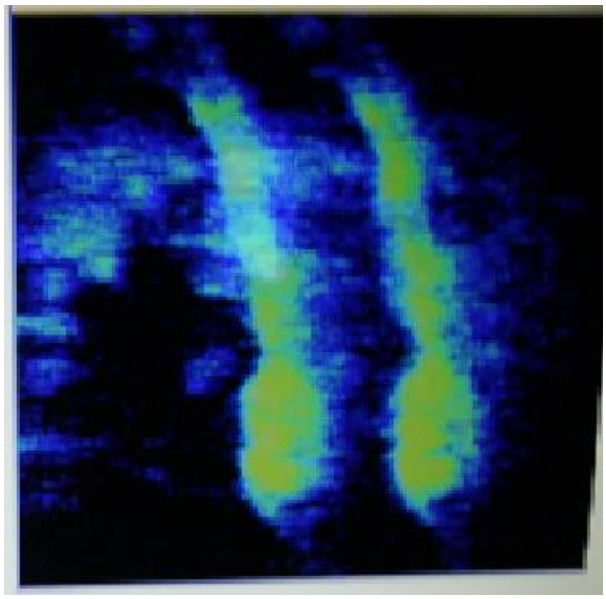

Figure 3.8: Image duplication if lag remains uncompensated.

In order to prevent the duplication of the object and to compensate for the lag, a

pixel offset adjustment was made to the software by imaging a drop of the chemical, fluorescein, and changing the pixel offset until the dots overlapped (Figure 3.9).

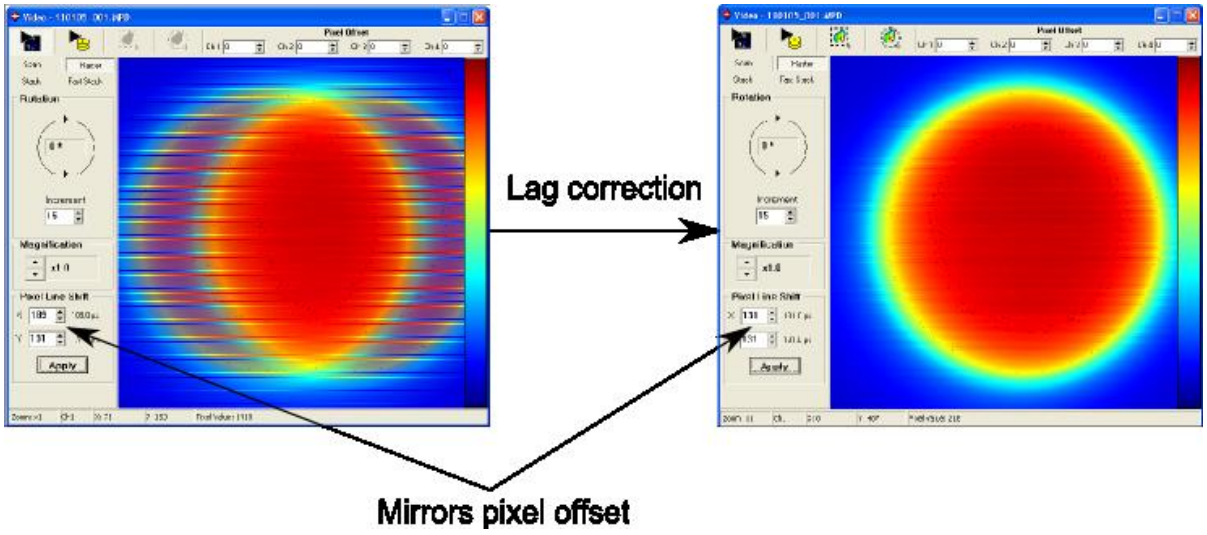

Figure 3.9: Compensation of the lag by changing the pixel offset of the mirrors.

Chapter 4

Two-Photon Microscope: Results and Comparaison

4.1 Introduction

The microscopic study of biological tissues has been developed throughout the ages. In the past century, the use of lasers to examine biological tissues have shown many promises, enabling researchers to obtain in-depth information without having to physically cut the sample at the risk of contaminating the tissues. The first such system capable of 3D imaging was the Confocal microscope developed and patented by Marvin Minsky in 1961 [24]. Confocal microscopy (CM) provided researchers a means to achieve in-depth information without having to examine the tissue one layer at a time. Although due to the excitation source and processes occuring during excitation, the physical integrity of the tissues were greatly affected. These damaging effects were later eliminated by the introduction of ultrafast lasers as an excitation source [6, 103, 104]. Using wavelengths in the near-IR region, this ultrafast technology gave birth to multiphoton microscopy which held the advantage of preserving the physical integrity of the sample [67, 88] during imaging. With the capabilities of using even longer wavelengths to image, accessing information in deeper layers was possible as less scattering occurred when inside inhomogeneous media [87]. But the true strength of a multiphoton microscope compared to other traditional microscopes is that imaging and the ablation of biological tissues can be done using the same system.

This chapter summarizes the testing of the home-built multiphoton microscope that would also provide the means to do precise ablation on biological tissues. We present the results obtained upon imaging bioligical tissues and compare them to results from a Confocal microscope for the exact same sample.

4.2 Experimental

The experimental setup used to obtain the results presented in this chapter is described in details in Chapter 3.

4.2.1 Pulse Duration

The pulse duration from the femtosecond laser oscillator is 30 fs. Since pulse duration plays a very important role, both in imaging and ablation, it is important to fully characterize the pulse after it propagates through different optical elements. This is because 2-photon excitation processes have a quadratic dependance on intensity and longer pulses significantly reduce the intensity delivered to the focal plane [5]. Short pulses of light, by definition, signifies that the pulses are composed of a certain bandwidth of frequencies. The refractive index of any optical element is wavelength dependent and therefore, as the pulse propagates through optical elements, the pulse will have some of its frequencies travelling faster than the others which stretches the pulse [84]. This process is known as group velocity dispersion (GVD). Hence, the number of optical elements in the beam path should be kept to the minimum as multiphoton microscopy acquires most if its advantages from the use of short pulses to image tissues. Furthermore, the ablation of tissues requires the use of short pulses ($<$ ps) since the pulse duration limits the energy branched out into disruptive mechanical pathways (refer to Chapter 1, section 1.10.1) which leaves the surrounding regions undamaged by the ablation process [55, 62]. Also, femtosecond laser pulses are shorter than the thermal expansion time and as a result, confines the ablation to the focus leaving the surrounding regions untouched [14].

To calculate the broadening of the pulse, the refractive index of the optical elements (with central wavelength at 800 nm) was calculated using the Sellmeier equation[105].

$$n(\lambda_l) = \sqrt{1 + \sum \frac{A_j \lambda^2}{\lambda^2 - B_j}} \quad (4.1)$$

where A_j and B_j are parameters characterizing the material called the Sellmeier coefficient, and λ_l is the laser's central wavelength.

The optics in the beam path were mostly made of BK7 glass. Therefore, the values of the Sellmeier coeffiecients for BK7 glass [106] are

Sellmeier Coefficients for BK7 ($\lambda = 800nm$)		
A_1	A_2	A_3
1.03961212	0.231792344	1.01046945
B_1	B_2	B_3
$6.0069867\text{x}10^{-3}\mu m^2$	$2.00179144\text{x}10^{-2}\mu m^2$	$1.03580653\text{x}10^{2}\mu m^2$

Replacing these coefficients in equation 4.1 gives the value of the refractive index for BK7 to be 1.5106.

To calculate the broadening of the pulse, the GVD caused by the BK7 glass must be determined. The GVD was calculated using the following relation [83]

$$GVD = \frac{d}{d\omega}\frac{1}{v_g} = \frac{d}{d\omega}\frac{dk}{d\omega} = \frac{d^2k}{d\omega^2} \tag{4.2}$$

and by more rigorous development we get

$$GVD = \frac{\lambda^3}{2\pi c^2}\frac{d^2n}{d\omega^2} \tag{4.3}$$

where v_g is the group velocity, λ is the central wavelength of the laser, c is the speed of light, k is the wave vector, and ω is the frequency.

From the second derivative of the Sellmeier equation, the coefficient $\frac{d^2n}{d\omega^2}$ was found to be .056 μm^2. Substituting this value and with a wavelength of 800 nm, equation 4.3 gives a GVD value of 50.6 $\frac{fs^2}{mm}$ for BK7.

The group delay dispersion (GDD) [107] of light travelling through the BK7 glass is given by the following equation:

$$GDD = GVD \cdot l \tag{4.4}$$

where l is the length of glass that the pulse travels through.

In our microscope, the optical elements in the beam path, before entering the objective, are the scan lens, tube lens, filter wheel and the dichroic mirror. The combined glass thickness of the components through which the pulse travels is ≈ 23.1 mm, giving a GDD value of 1169 fs^2.

From the group delay dispersion, the pulse duration was calculated using the dispersive pulse broadening equation [84, 107].

$$\tau = \tau_o \sqrt{1 + (\frac{GDD}{\tau_o^2} 4 \ln 2)^2} \tag{4.5}$$

where τ_o is the pulse duration before entering the dispersive media; in this case, 30 fs.

Equation 4.5 gives a pulse duration of 48.4 fs after propagation through the optical elements and before entering the back aperture of the objective.

Determining the pulse duration after travelling through the objective and all its optical elements is very complex and difficult to measure. However, the GDD of a 60x waterdip objective used on the microscope is known to be 21338 fs^2. Therefore, a rough approximation of the pulse duration at the focus can be determined using the pulse broadening equation. The pulse duration exiting the objective is approximated to be roughly $\tau = 1.2$ ps.

4.2.2 Systems evaluation and performance

The pulses from the oscillator were focused by a microscope objectives (Olympus, 10x, 20x, 40x, and 60x waterdip). In chapters 1 and 2, it was mentioned that the amount of fluorescence in 2-photon microscopy has a quadratic dependence on intensity. In order to fully characterize the optical system, the intensity delivered to the focal plane must be determined [5, 17].

The peak laser power, P, delivered to the region is defined as:

$$P = \frac{E}{\tau} \tag{4.6}$$

where E is the energy per pulse and τ is the pulse duration.

The intensity, I, delivered to the sample's surface, assuming 100 percent transmission, is determined by:

$$I = \frac{P}{A} \tag{4.7}$$

Where A is the area of focus.

In microscopy, the area of focus can only be determined by precisely knowing the PSF of the optical system since the PSF reflects the true nature of the area of focus and incorporates unwanted factors such as: spherical aberrations, refractive index mismatch, and nonlinear processes among others.

Assuming the case where there are no aberrations and no coverslip used, the area of focus is determined by knowing the focal spot size of the objective.
The focal spot size of an objective is given by [71]

$$D(x, y) = 1.22\frac{\lambda}{NA} \tag{4.8}$$

where λ is the wavelength of the excitation source and NA is the numerical aperture of the objective.

In order to determine the depth of focus, resolution, and the intensity distribution along the z-direction, the confocal parameter was calculated. Within the confocal parameter, the intensity remains more or less constant [41, 105] and therefore, under ideal conditions, may give a good approximation to the resolution and the intensity distribution within the excited region along the z-direction.

For a low NA objective and assuming a gaussian beam profile, the paraxial approximation can be used [25, 108]. Hence, the confocal parameter can be calculated as

$$b = k\omega_o^2 \tag{4.9}$$

where k is the wavevector and ω_o is the beam radius at the focus.

The value of ω_o can be calculated from the spot size of the objective using the following

equation.

$$\omega_o = \frac{D(x,y)}{2} = \frac{0.66\lambda}{NA} \tag{4.10}$$

Thus, the confocal parameter is given by

$$b = k(\frac{0.66\lambda}{NA})^2 \tag{4.11}$$

with

$$k = \frac{2\pi n}{\lambda} \tag{4.12}$$

where n is the refractive index of the medium into which the light is being focused.

Equation 4.11 is simplified to

$$b = \frac{2\pi n}{\lambda}(\frac{0.66\lambda}{NA})^2 \approx \frac{2.74n\lambda}{NA^2} \tag{4.13}$$

By the definition of the confocal parameter, the intensity remains basically the same all along the length of the confocal parameter and is given by (using equation 4.7)

$$I(x,y) = (\frac{NA}{.66\lambda})^2\frac{E}{\tau} \tag{4.14}$$

This intensity is only valid along the length of the confocal parameter and will significantly be lowered further away from the focus.

Resolution

Finding the values of both the spot size and the confocal parameter can give a good approximation as to the resolution of the microscope along the xyz directions. The theoritical value of the spot size of the objective, $D(x,y)$, and half of its value gives a rough approximation to the resolution along the xy direction. The confocal parameter will, on the other hand, give a rough approximation to the resolution along the z-direction. The reason comes simply from the principle that a 2-photon process has a quadratic dependance on intensity so emission from layers outside the length of the confocal parameter diminish rather quickly, confining the excitation mostly within that length.

Most of our experiments on fish gills were done using a 10x dry objective with an NA of 0.3. Due to the low NA, the paraxial approximation is satisfied and the equation for

the confocal parameter is applicable [25, 108]. In the absence of aberrations, the resolution of the microscope can be approximated by the following equation using a central wavelength of 800 nm for excitation and $n = 1.33$ for water.

$$resolution(x, y) = \frac{D(x, y)}{2} \approx 1.63\mu m \tag{4.15}$$

and the confocal parameter

$$b \approx 32.4\mu m \tag{4.16}$$

The theoretical value is 1.63 μm for the lateral resolution and 32.4μm for resolution along the axial direction. This is in good agreement with other experimental results [20, 69, 103] where a lateral resolution of 1.84μm and an axial resolution of 27.24μm was obtained for a similar microscope objective.

In order to determine the quality of the alignment and the overall performance of the system, the PSF of the system, using a 10x objective, should find itself to be within the range of 1.63-2.00μm for the lateral direction and 25-35μm for the axial direction. Any higher values could mean that the system is not optimized and alignment should be re-ajusted to enhance the microscope's performance.

Intensity at the focal plane

For a rough approximation of the peak intensity delivered at the focal volume, equation 4.13 is used. Assuming that the 10x objective has the same quantity of optical elements and is made of the same material as the 60x objective, the pulse duration at the exit of the objective should be approximately of $\tau = 1.2$ ps. For a diffraction limited spot size and maximum energy of 8 nJ at 800 nm, the intensity delivered to the focal volume is approximately $10^{11}\ \frac{W}{cm^2}$.

From Chapter 2, the fluorescence intensity emitted from within the focal volume, per pulse, was proportionnal to the intensity delivered to the focus and gives

$$I_f(\tau = 1.22ps) \approx \delta_2(\lambda) \cdot (10^{11}\frac{W}{cm^2})^2 \tag{4.17}$$

where $\delta_2(\lambda)$ is the cross section of the dye molecules at the wavelength of light used for excitation.

4.3 Results

4.3.1 Goldfish (*Carassius auratus*)

The goldfish gill sample imaged in this section was graciously provided by Prof. Steve Perry and his Ph.D student, Velislava Tzaneva, from the University of Ottawa. The gills are believed to be the system responsible for filtering and delivering the oxygen to the fish's cells.

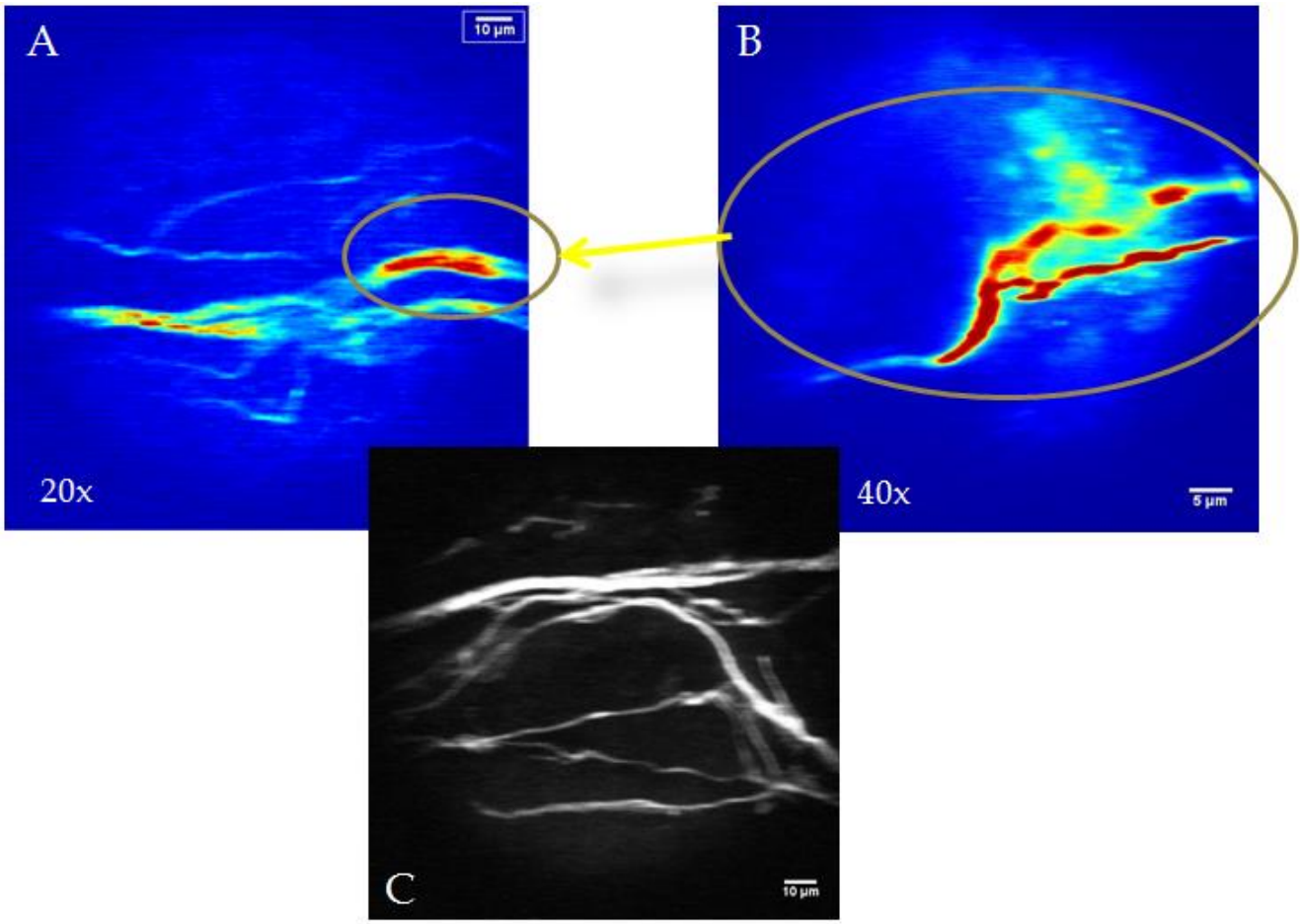

Figure 4.1: Panels (A),(B), and (C) are images of the filamental nerve fibres of the goldfish gills obtained with the multiphoton microscope. (A) was taken using a 20x dry objective and (B) is a close up of (A) using a 40x dry objective. Figure (C) is a filamental nerve fiber network of the gill using a 20x dry objective.

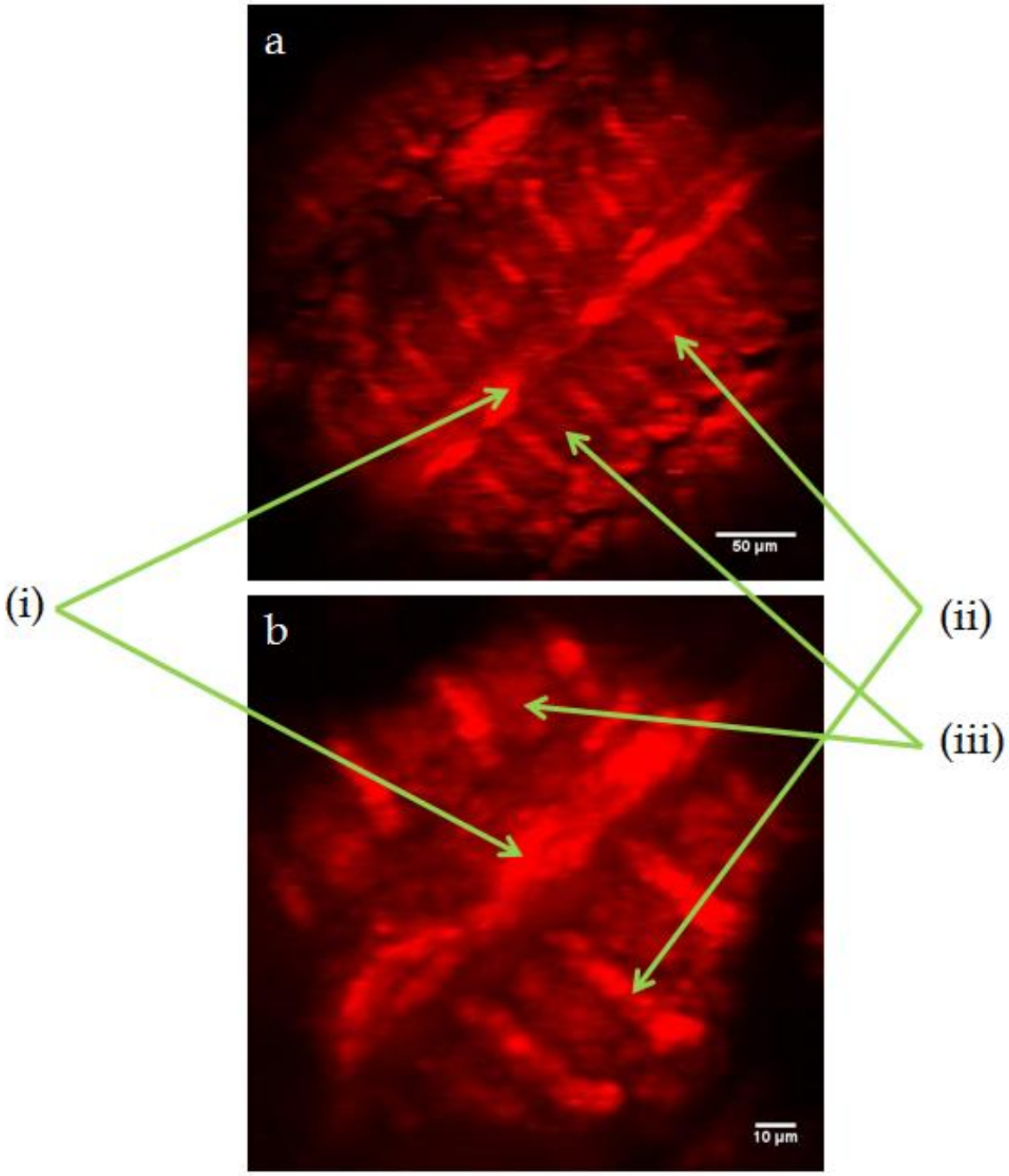

Figure 4.2: Panels (a) and (b) are images of goldfish gills acclimated to $7°C$. The temperature at which the goldfish are acclimated results in different gill morphology. Panels (a) and (b) are z-stack projections of 235 sections with a 1 μm interval between each slice; taken with a (a) 10x dry objective and (b) 20x dry objective of the same region and depth. In the images, the core of the gill (i) is the filament; the branches coming on either side of the filament (ii) are the lamellae; (iii) the interlamellar cell mass located in between the lamellae.

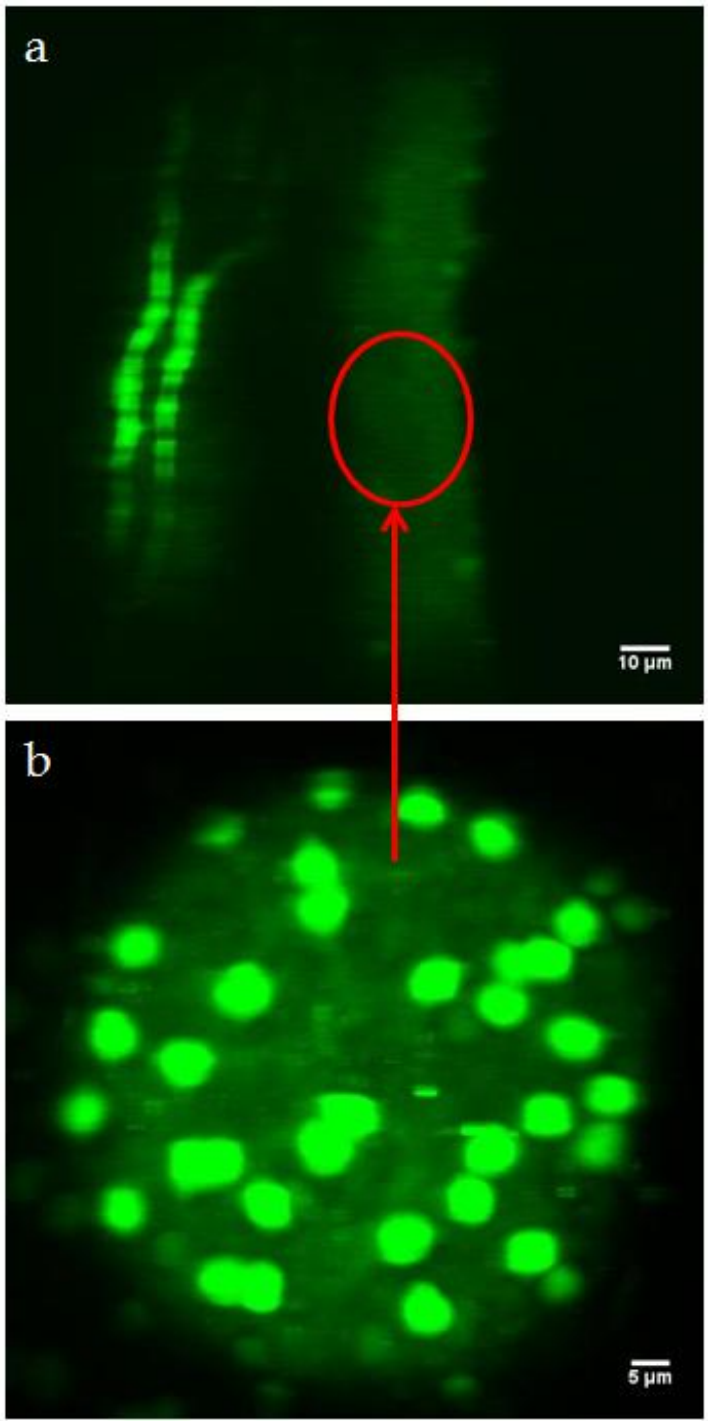

Figure 4.3: Panels (a) and (b) are images taken of a goldfish gill acclimated to $7°C$. (a) taken with a 20x dry objective and located at a depth of $64\mu m$. The central staining of (a) are filamental nerve fibers; (b) is a close up of the fish's lamella using a 40x dry objective, the bright dots are stained lamellar neuroepithelial cells.

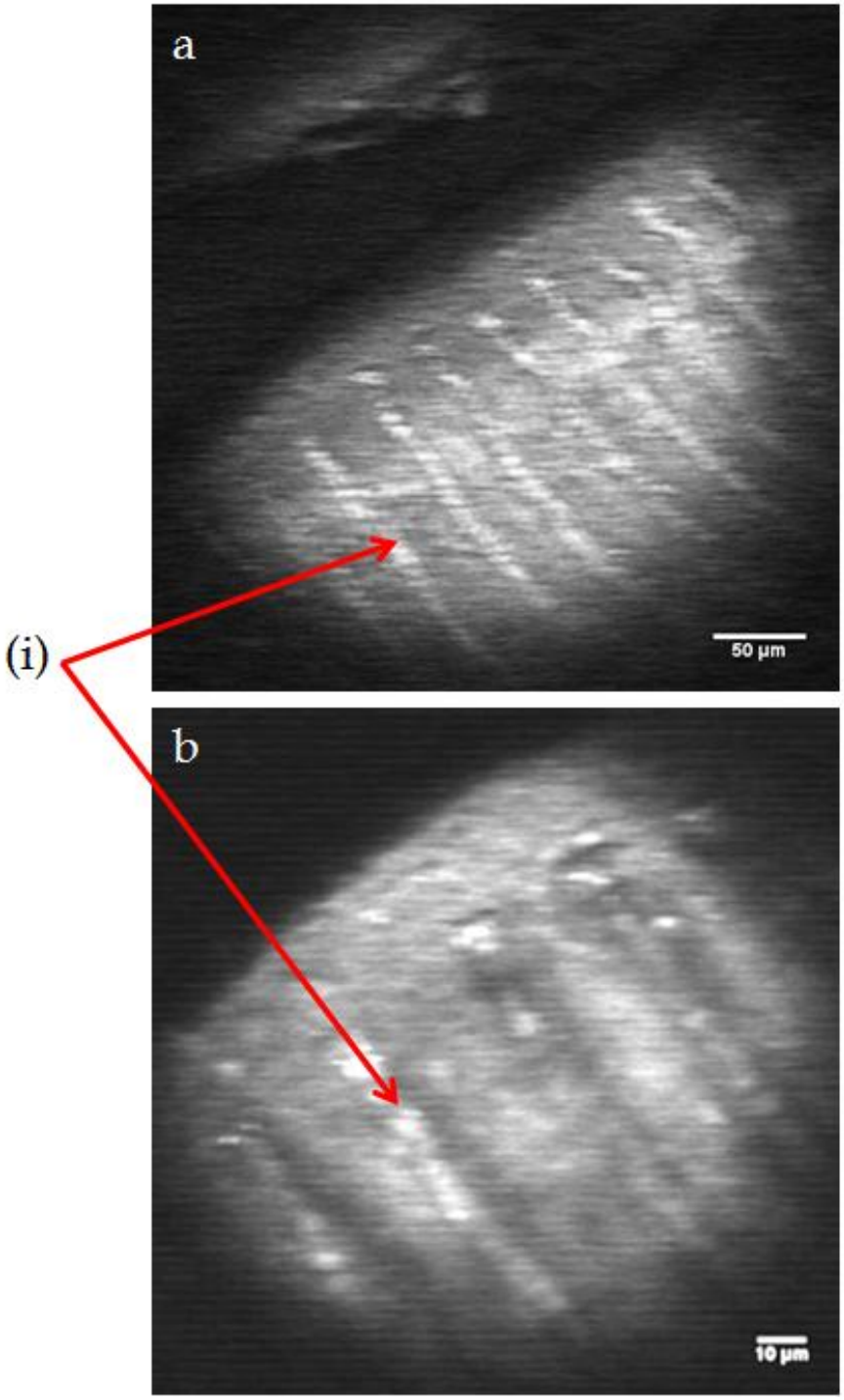

Figure 4.4: Panels (a) and (b) are images taken of a goldfish gill acclimated to $7°C$. The gill was prepared and placed on its side and imaged as if having a sideway view of the gill. Images taken with a (a) 10x dry objective and (b) 20x dry objective. Both images were taken at a depth of $48.4\mu m$. Arrow pointing at (i) the lamella.

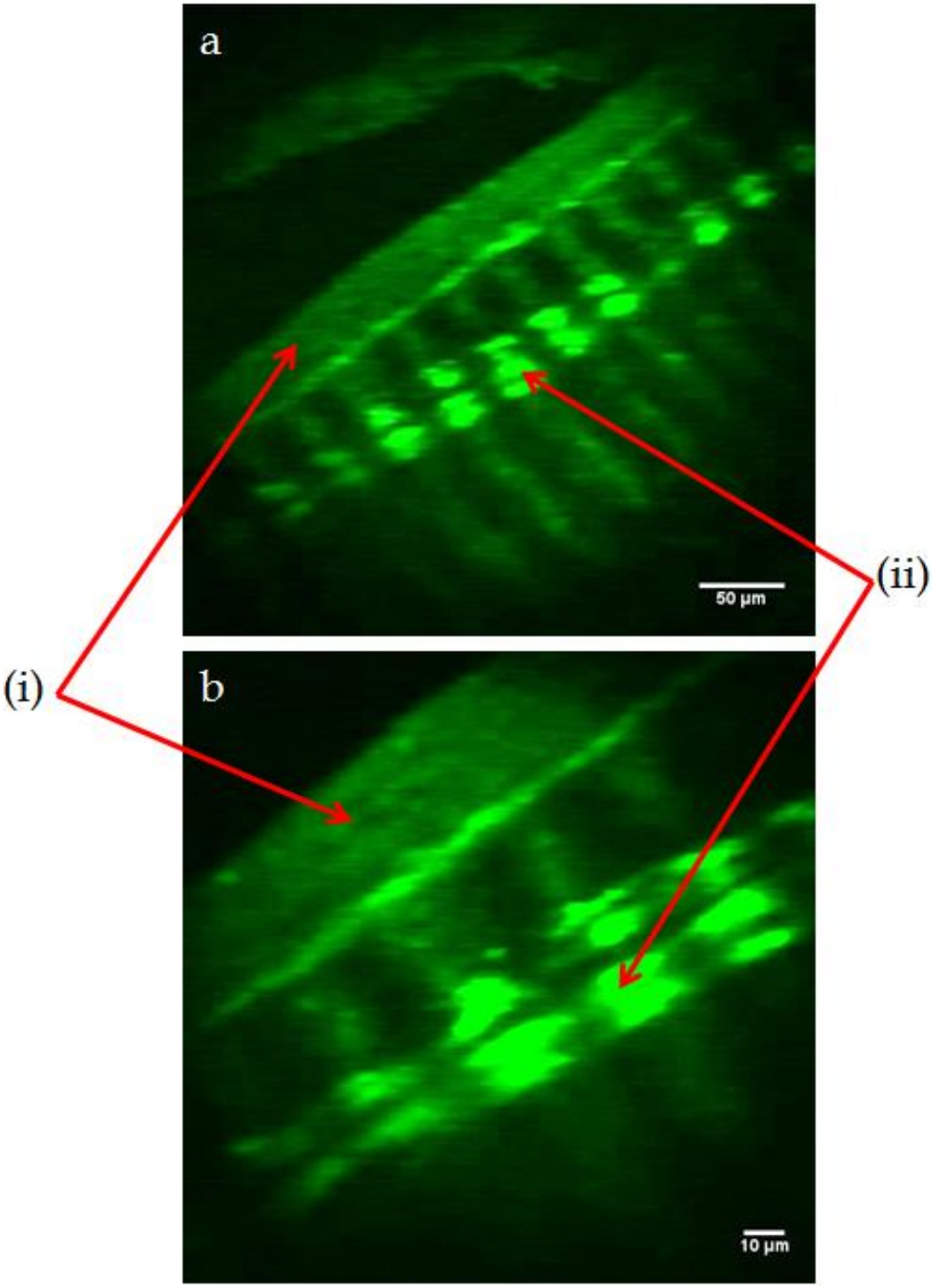

Figure 4.5: Panels (a) and (b) are images taken of a goldfish gill acclimated to $7°C$. The gill was prepared and placed on its side and imaged as if having a sideway view of the gill. Images were taken with a (a) 10x dry objective and (b) 20x dry objective. Panel (a) was taken at a depth of $88\mu m$ and Panel (b) at a depth of $75.2\mu m$. Arrows pointing at the (i)filament and (ii) the filamental neuroepithelial cells.

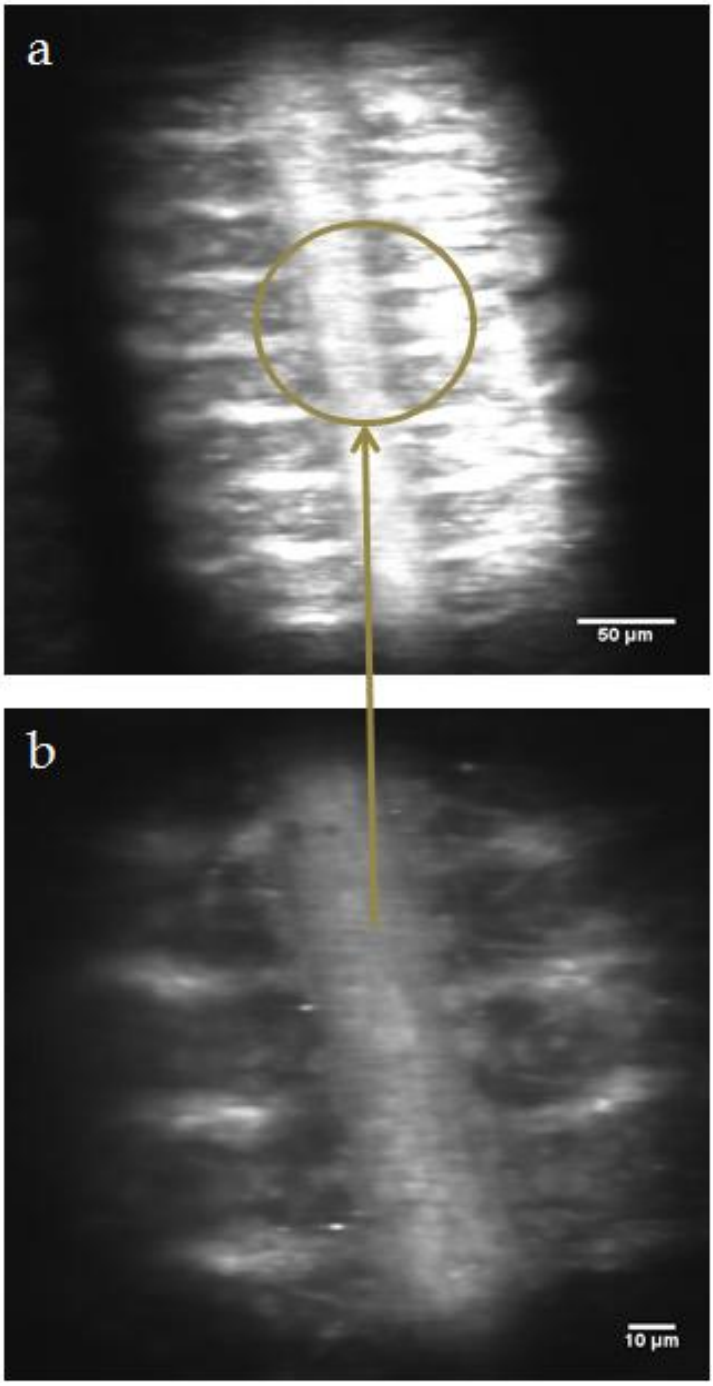

Figure 4.6: Panels (a) and (b) of a goldfish gill acclimated to $7°C$. The staining of the goldfish gill, in these reconstructions, proved to be unsuccessful and no strong emission from the stained parts of the gill are observed. The obtained images, as shown, were built by the collection of the background signal emitted from the fish gill structure. Panel (b) a closeup of the fish filament and lamellae of Panel (a). Images were taken with a (a) 10x dry objective and (b) 20x dry objective.

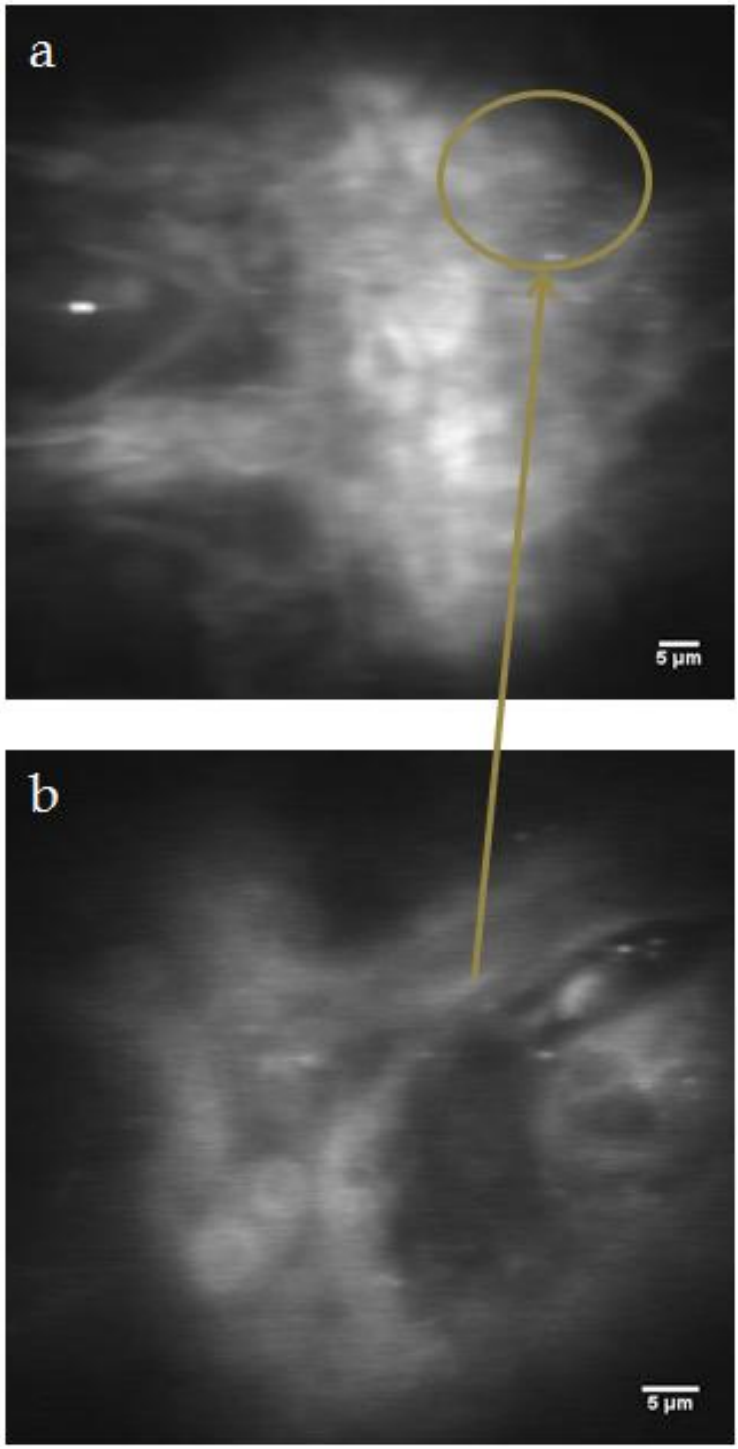

Figure 4.7: Further closeups on the fish filament and lamellae of Panel (a) and (b) in Figure 4.6. Images were taken with a (a) 40x dry objective and (b) 60x waterdip objective.

Image filtering

One of the advantages of multiphoton microscopy is its ability to excite multiple dyes simultaneously, each releasing a fluorescence signal with the wavelength specific to that dye. This advantage can be exploited if the system design includes bandpass filters and numerous detectors. Bandpass filters are used to seperate each fluorescence signal by sending the signals along different pathways onto different detectors. The signals captured by the detectors are then superposed, giving a clear image. The current design of the multiphoton microscope currently only works with a single detector but with the ability to eventually add more. Hence, in the case where a sample is tagged with numerous dyes, the system would capture all the fluorescent signals and image them simultaneously, reducing the resolution and the overall image quality. The resolution is reduced since the signal from overlapping regions cannot be distinguished by the detector. Figure 4.8 demonstrates the image quality of a goldfish gill, z-stacked, in the absence of bandpass filters and multiple detectors. In Figure 4.8, three dyes were used. The first was tagged to the filamental nerve fibers, the second was used to tag onto the filamental neuroepithelial cells, and the third dye was DAPI. DAPI gives extra protection against photobleaching and is a dye widely used by biologists when imaging with a confocal microscope. Multiple dyes attached to different sites allow the complete accumulation of information in a single scan. All three dyes fluoresce at different wavelengths which can be independantly detected using appropriate cold mirrors and filters. The image below is obtained without filtering.

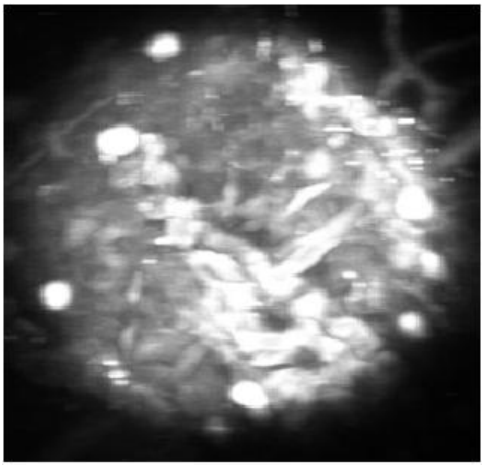

Figure 4.8: Image obtained upon exciting the three dyes tagged to the goldfish gill; no clear structure and different parts of the gill can be discerned from each other.

The images constructed by the collection of data can sometimes be of questionable quality. The intensity of the layers can sometimes be too high (see Figure 4.9(a,b)), leaving out the finer details lost in the background. For this reason, in order to improve the quality of the images, biologists commonly use a software called ImageJ. It is a software capable of manipulating the data collected to build the original image and improve image quality by diminishing the signal intensity of the layers exposing the finer details. In addition, it also has the ability to filter out noise, to smooth and sharpen the images. This is done through the software modifying the floating point pixel values. Values attributed the each pixel the signal was being collected by the computer.

Figure 4.9 demonstrates the strength of ImageJ in improving image quality and exposing the finer details previously lost in the background. The images are z-stacked projections of all the collected layers recreating a 3D image of the goldfish gill. Figure 4.9(a,b) are the original images obtained upon doing a z-projection of the collected layers directly without using imageJ and with the signal intensity too high. This leaves out the finer details. These original images were then manupilated in ImageJ using two different type of projections to z-stack and recreate the 3D images. The median projection type (see Figure 4.9(c,d)) exposed the finer details of the fish's filament. The sum projection type (see Figure 4.9(e,f)) exposed the finer details of the lamellae.

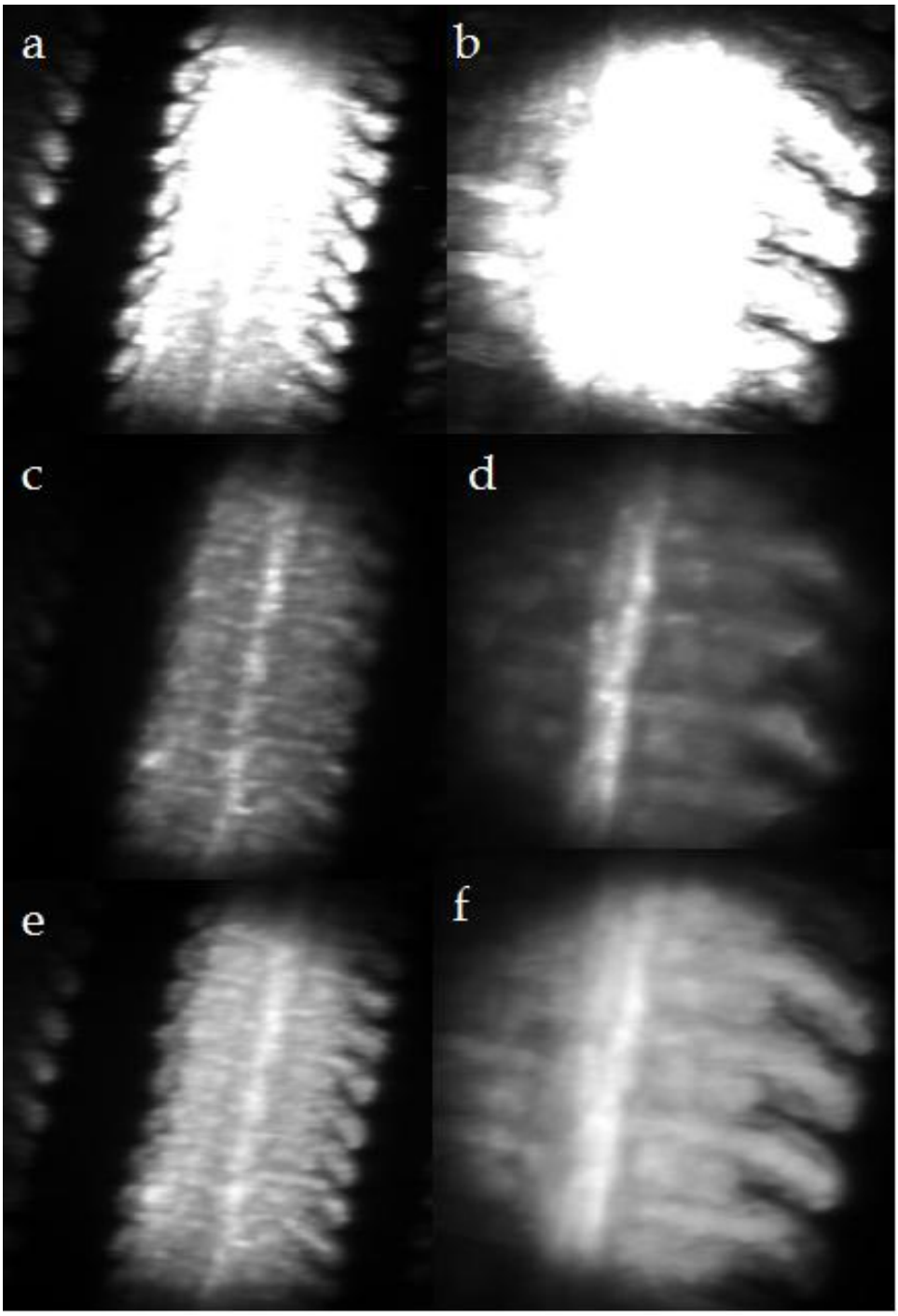

Figure 4.9: Images of a goldfish gill acclimated to 7°C; all images are z-projections of the collected layers. Panel (a) and (b) are the original images obtained from the multiphoton microscope; Panel (c) and (d) are median z-projections of the original collected layers; Panel (e) and (f) are sum z-projections of the original collected layers. Panel (a) was taken with a 10x dry objective and (b) with a 20x dry objective.

Figure 4.10 is another example of the use of ImageJ in improving the image quality and the layers of collected data. Figure 4.10(a) is a layer section of a goldfish gill obtained by a confocal microscope from Dr. Andrew Pelling's Lab. The scan is that of an XYZ galvano scan technique. Figure 4.10(b) is a maximum intensity projection of all the layers, z-stacked, and show results in better detail quality with a sharper and smoother image than that directly coming from the confocal microscope.

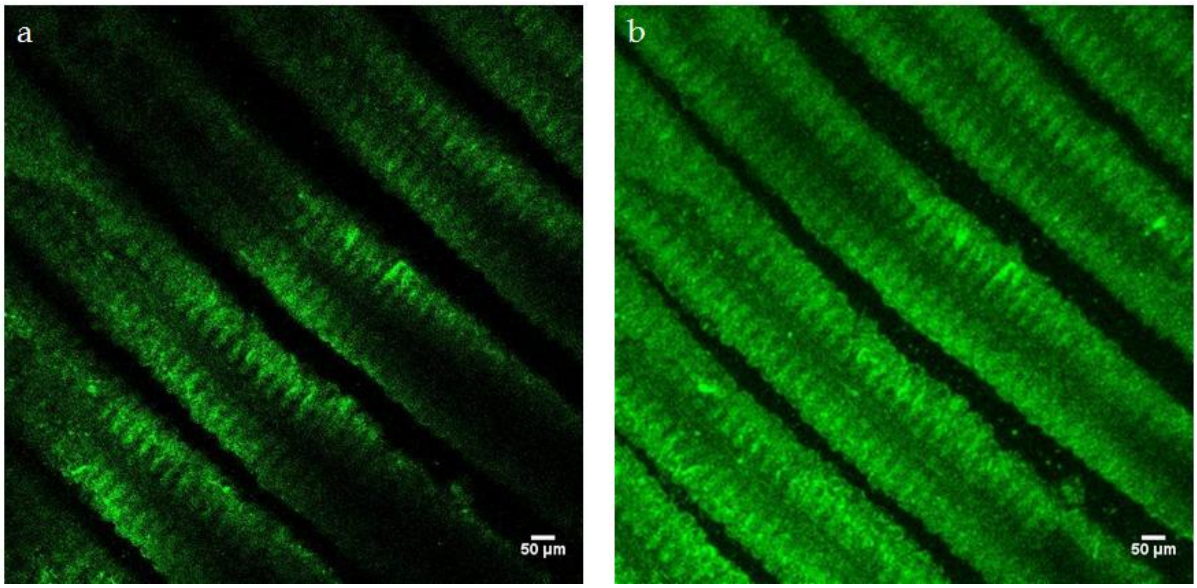

Figure 4.10: Confocal microscope images of a goldfish gill acclimated to 7°C. The scan type used to obtain the gill image was a XYZ galvano scan technique. (a) is the original layer collected by the microscope, located at a depth of $9\mu m$; taken with a 10x dry objective (graciously provided by Dr. Andrew Pelling's lab). (b) is the maximum intensity projection of all the layers, z-stacked, using ImageJ.

Confocal Comparison

In theory the Confocal microscope should yield better results than that of the multi-photon microscope. In order to test the alignment and overall system performance, the images obtained with the two-photon microscope were compared to that of the confocal images for the same samples.

Figure 4.11 are images of a goldfish gill acclimated to 7°C, obtained from a confocal microscope (a,c) and the multiphoton microscope (b,d). For comparison, the images were obtained under the same conditions by using a 10x dry objective with the same NA and scans were performed on the exact same sample. At first glance, it may appear that the images obtained by the multiphoton microscope used an objective of higher magnification. This is not the case as it is due to the limited field of view of the design and the small deflection angle of the mirror which gives the appearance of a digital zoom on the gill. It is also to be mentionned that, due to the absence of DAPI to protect against photobleaching, the sample was first scanned by the multiphoton microscope due to the possible damage to the physical integrity of the gill if it first went under the confocal microscope.
The central gill filament in (b) clearly shows much finer details than that of (a), where most of the central details of the filament are absent. Furthermore, the lamellae, or branches, of the gill in (a) are barely visible when compared to the details in (b). From these images, it was concluded that our system was fully functional and could perform on the same level as the Confocal microscope.

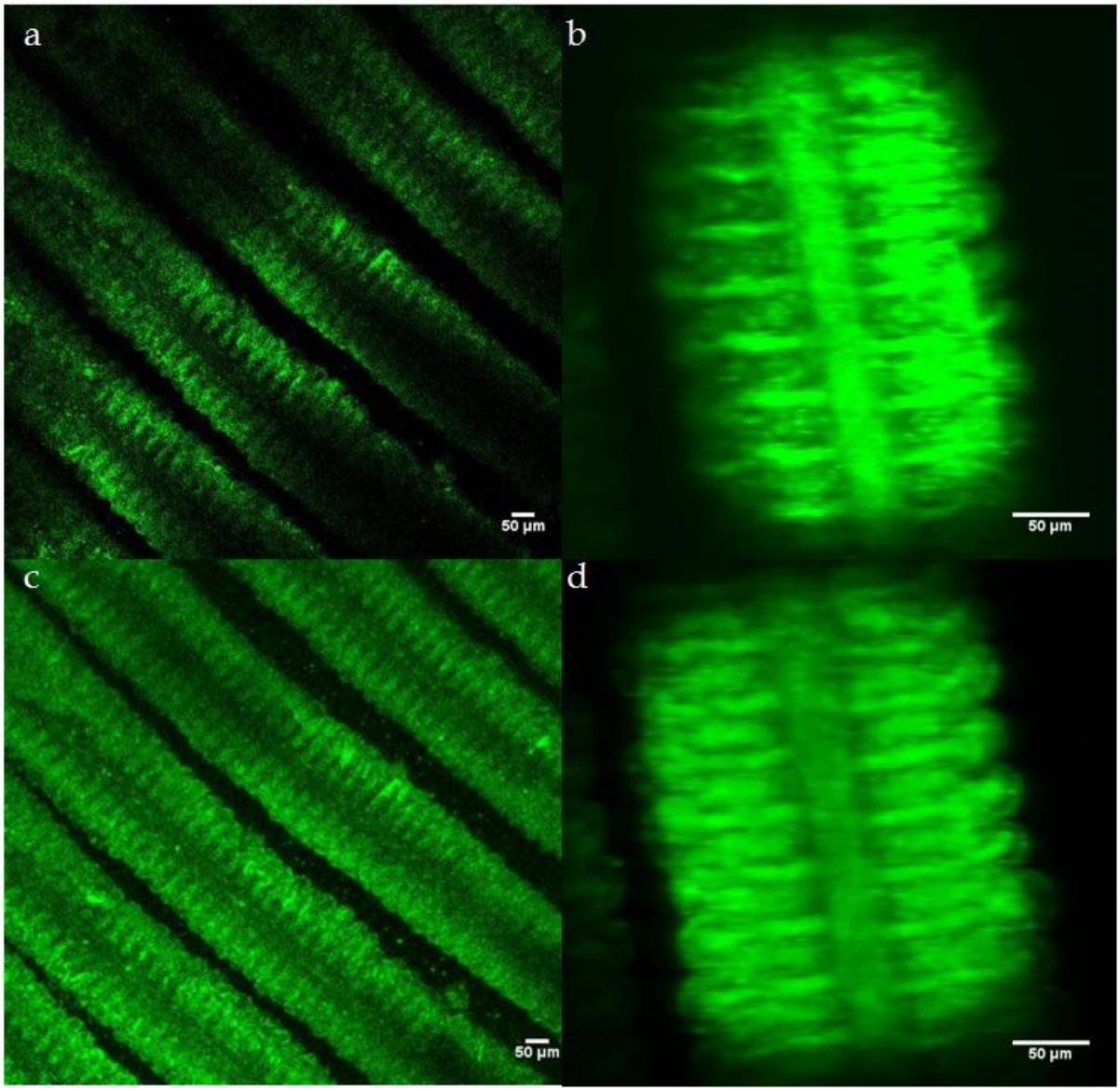

Figure 4.11: Goldfish gill acclimated to 7°C. (a) was taken by a Confocal microscope and (b) our Multiphoton microscope; (c) and (d) are projection, z-stack, of the layers producing a 3D images of the gill. Images were taken with a 10x dry objective.

4.3.2 Bovine Pulmonary Artery Endothelial cells

The bovine pulmonary artery endothelial sample imaged in this section was graciously provided by Dr. Pelling at the University of Ottawa. Since 1970, bovine cells have been studied to better understand hypertension and coronary heart diseases.

The samples obtained for this experiment were prepared and bought from Fisher. The sample is tagged with three different dyes onto different parts of the bovine cells. Due to the capture of all the signals and use of a single detector in the multiphoton microscope, the image quality is affected and appears blurry. There is also another factor that may cause this blurriness which could be the result of the presence of longitudinal chromatic aberrations in the system. The aberrations can be eliminated by modifying the distance of the telescope optics located in front of the objective.

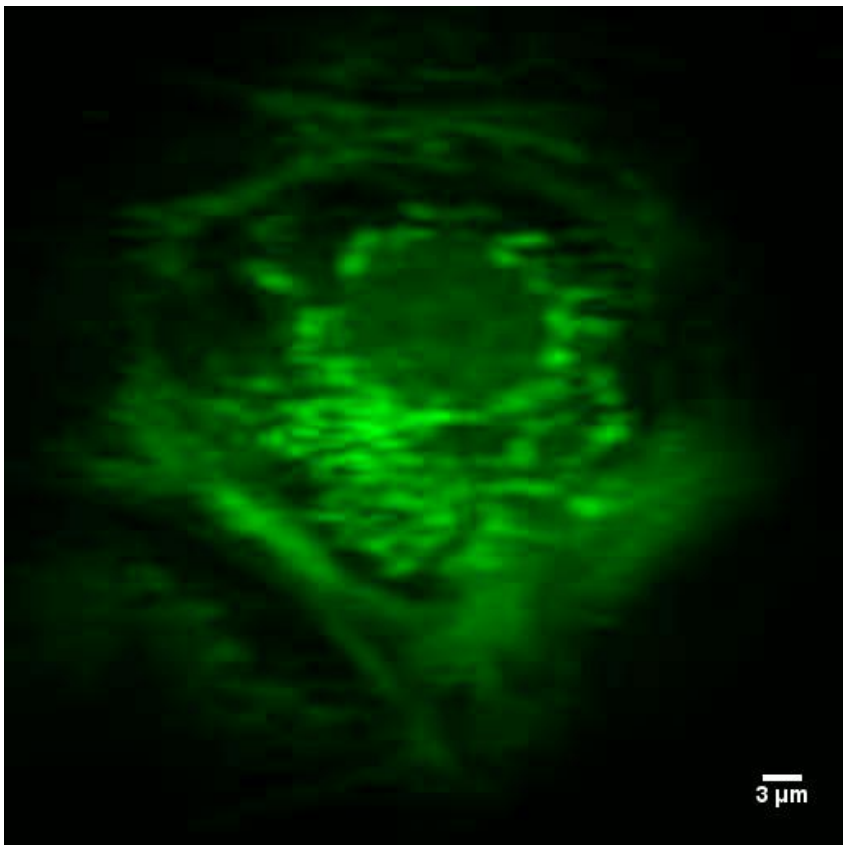

Figure 4.12: Bovine Pulmonary Artery Endothelial cell (BPAE line); taken with a 60x waterdip objective.

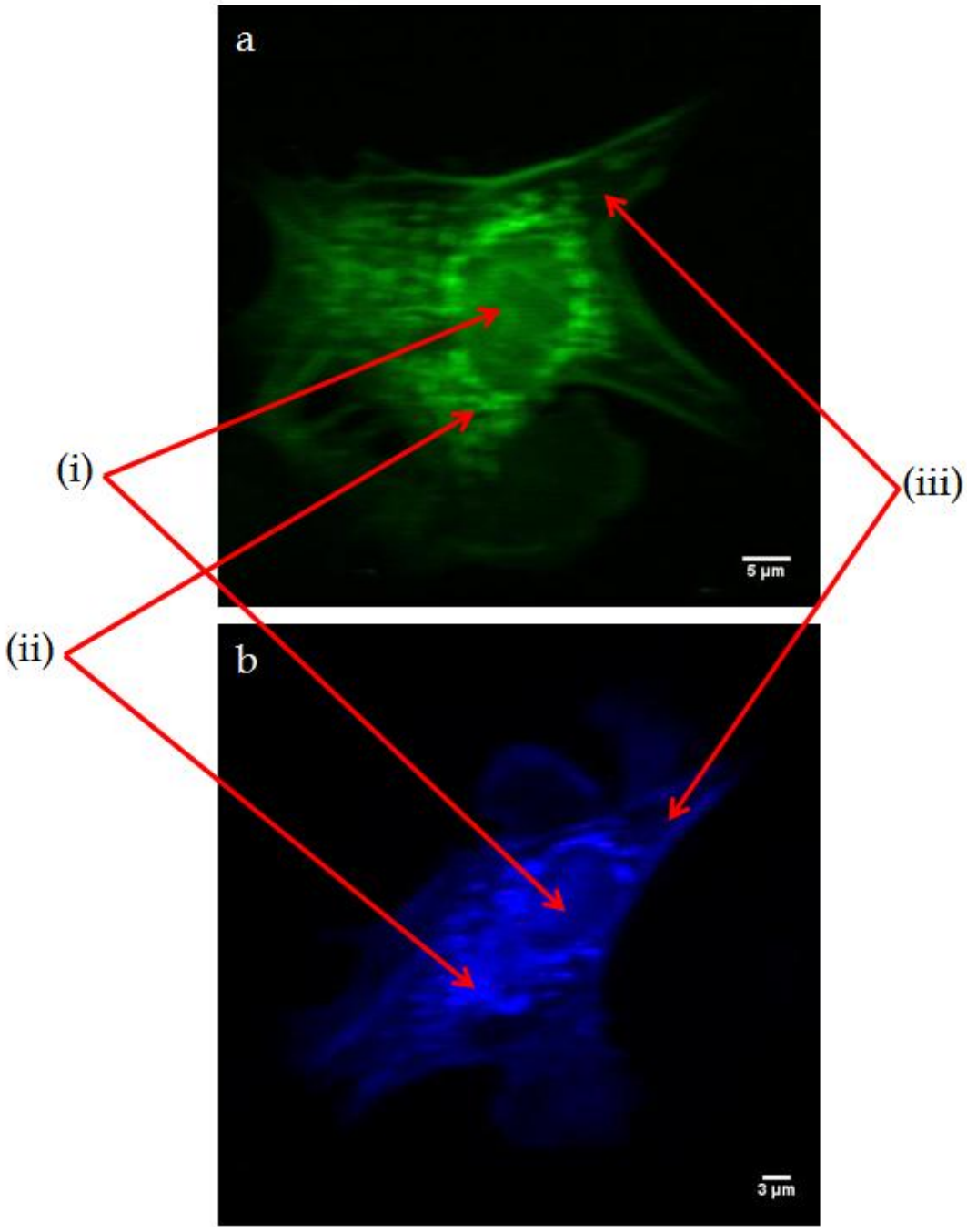

Figure 4.13: Bovine Pulmonary Artery Endothelial cell (BPAE line); images obtained by the Multiphoton microscope. Images were taken with (a) a 40x dry objective and (b) a 60x waterdip objective. The cells were tagged with 3 dyes each attaching themselves to different parts of the cell; Dapi(blue) is attached to the (i) nucleus, MitoTracker Red CMXRos(red) tagged to the (ii) mitonchondrial network (spots) and Alexa Fluor 488 conjugated to phalloidin(green) tagged to the (iii) filamentus actin (membrane).

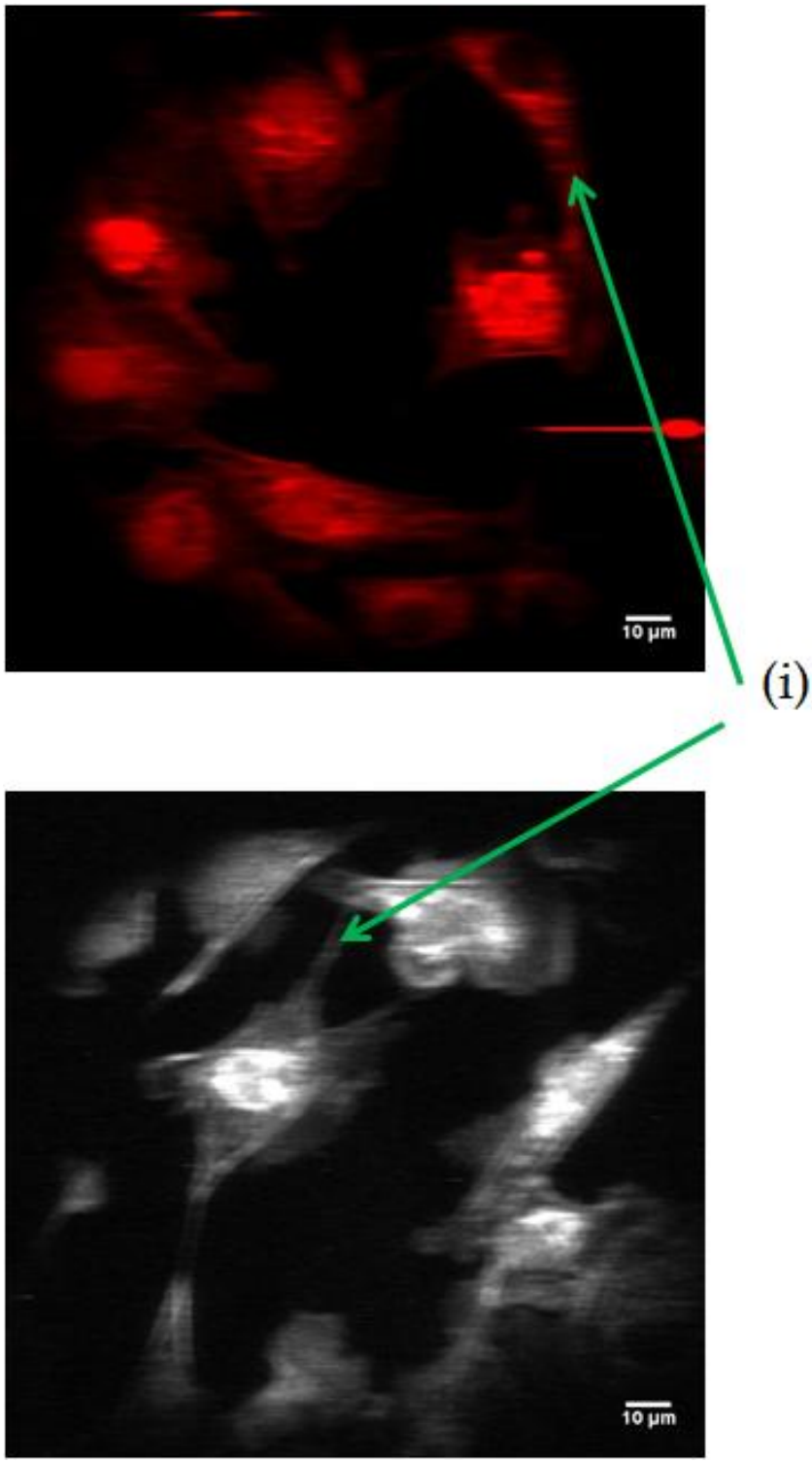

Figure 4.14: Images of Bovine Pulmonary Artery Endothelial cells; interconnected by the (i) filamentus actin into a broad network of interlinked cells enabling nutriment exchange and communication between the cells. (top) taken with a 20x dry objective; (bottom) taken with a 20x dry objective and z-projected with a thickness of $24\mu m$.

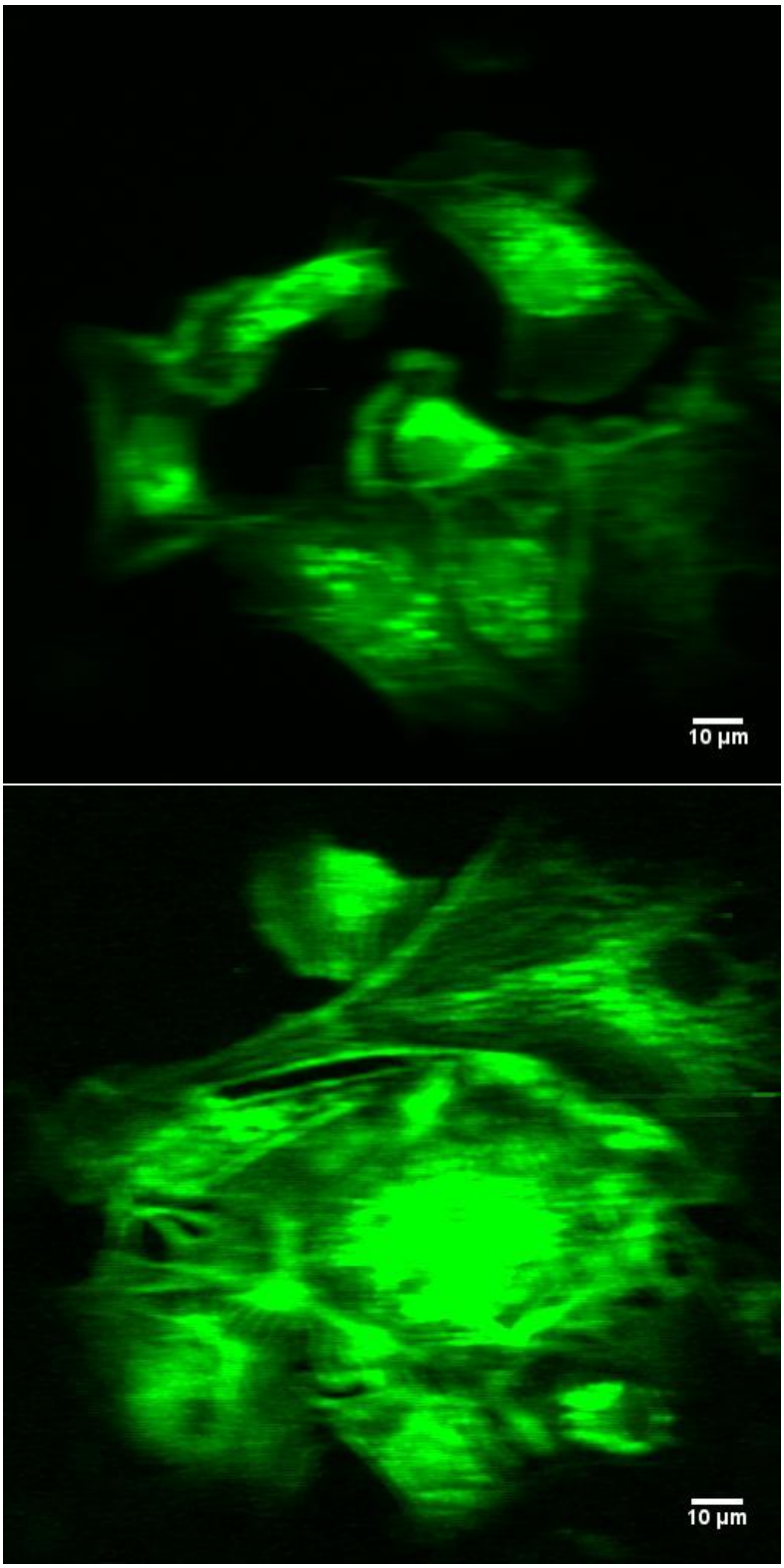

Figure 4.15: Network of Bovine Pulmonary Artery Endothelial cells. Images taken with (top, bottom) a 20x dry objective and (top) z-projected with a thickness of $27\mu m$.

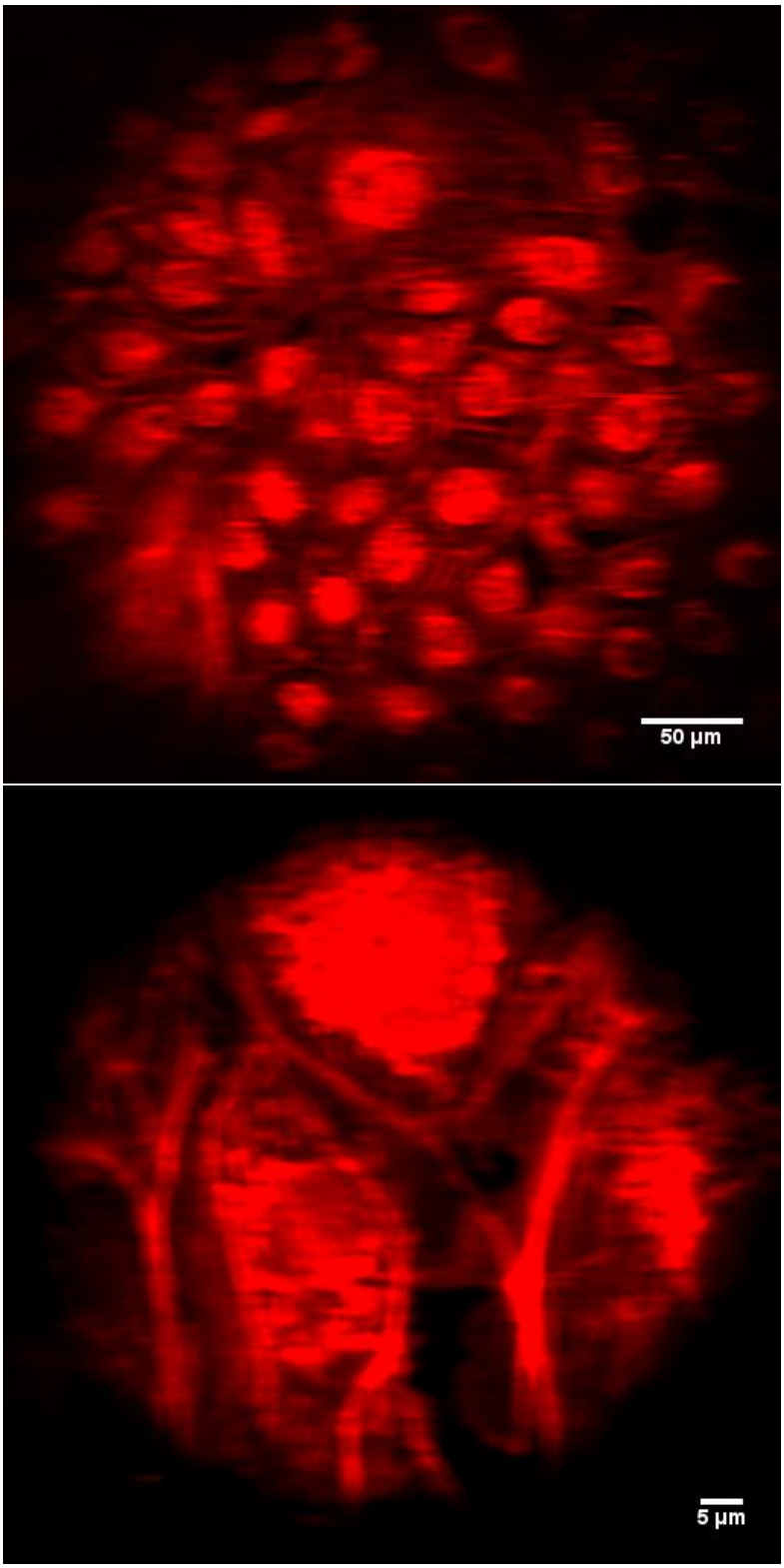

Figure 4.16: Images of Bovine Pulmonary Artery Endothelial cells; monolayer of interconnected cells; (top) taken with a 10x dry objective and z-projected with a thickness of $70\mu m$ and (bottom) taken with a 40x objective and z-projected with a thickness of $11\mu m$.

4.4 Conclusion and Future Work

In conclusion, we have successfully designed, built, and tested a multiphoton microscope. Many improvements are still in order to increase the overall performance of the microscope and to decrease any aberrations that could be present. We will also strive to increase the quality of the images. Even without these improvements the comparison of the image of the goldfish gill between our multiphoton microscope to a confocal microscopy shows that this system can perform equally or better without the disruptive effects to the physical integrity of the sample. In addition, our ability to distinguish the different parts of the Bovine Pulmonary Artery Endothelial cells leads us conclude that our system is capable of sub-cellular resolution.

Future work on the microscope will focus on improving some of the characterictics of the design and add components to the setup. Firstly, the design should be improved to incorporate the addition of bandpass filters and detectors in order to separate the different wavelengths coming from the multiple dyes tagged onto a sample. The separation of the wavelengths would increase the resolution and the quality of the image making it possible to differentiate between the different regions of the biological tissues and decreasing the image blurriness. Secondly, pre-chirping the pulse would minimize pulse broadening due to GVD, resulting in the delivery of shorter pulses at the interaction region. This would increase the intensity at the focal volume producing higher emitted fluorescence intensity signals and, as a result, increase the resolution by a significant amount. As well, the 10x, 20x, and 40x dry objectives should be changed to waterdip objectives in order to increase the resolution of the microscope by reducing spherical aberrations and false axial scaling which is introduced by the index mismatch of the media.

With the microscope now functioning, future studies should now concentrate on nanoscale ablation of soft-tissue and its effect on the cells and surrounding regions. A better understanding of the ablation process and its effects should, in the future, help in the development of new techniques that could be used for nanoscale manipulation of matter with light, resulting in new ways of treating cancer by using lasers to destroy cancerous tumors.

Chapter 5

Dielectrics Studies

5.1 Introduction

The study of the interaction of intense light with soft-matter, such as a tissue, in its native environment is very complex. This complexity arises from the introduction of an immersion medium in which the material is situated in order to maintain its physical integrity. This alters the optical breakdown process compared to, for example, the optical breakdown in air [55, 56, 57]. Since most biological systems, like tissues, are polymers, it was deemed more prudent to first study light-matter interaction with harder polymers such as PMMA and gradually make the way to softer polymers such as contact lenses contained in a saline solution and eventually to tissues in their native environment.

In our experiments, energy thresholds for the laser ablation and internal modification of PMMA were determined. The threshold energies for the ablation of PMMA were obtained using two different methods: first by surface line ablation and secondly, by surface single shot ablation. In line ablation, each micron of the sample is exposed to numerous laser shots. The number of laser shots is varied by changing the speed with which the laser focus is moved. The threshold values were then determined by the analysis of the sample under a microscope and finding the lowest energy for which ablation occured.

The threshold values for single shot ablation of PMMA were obtained by displacing the stage to a fixed position and delivering a pre-determined number of shots into the region. The stage is then displaced to another fixed position, repeating the procedure using a different pulse energy. Threshold values were then determined by analysing the

samples using a microscope (standard or a scanning electron microscope (SEM)) and finding the lowest energy that led to the ablation of PMMA. This process was repeated for different numbers of shots and different laser polarizations. Ablation craters demonstrated 3D nano-structures with honey comb like patterns within the ablation holes. The analysis of the modified regions and the nano-structures located within them suggested a prefered direction to the photoionization process that was along the laser polarization. Also, the nano-structures evolved with the number of shots delivered to the region.

Experiments were conducted to determine the threshold energy values for permanent refractive index modification and waveguide creation within the confined regions of the PMMA bulk. The threshold values were found using the same method used as surface line ablation except that light was being focused inside the material instead of on the surface.

5.2 Laser System

The light source used in this dielectric study is a Kerr lens mode-locked Ti:sapphire oscillator (Tsunami, Spectra-Physics) capable of producing pulses of < 30 fs with a maximum pulse energy of 8 nJ at a central wavelength of 800 nm and repitition rate of 76 MHz. The oscillator is pumped by a 5 W Nd:YVO_4 diode solid-state laser (Millenia, Spectra-Physics, 532 nm). The pulses are sent into the regenerative amplifier (Spitfire pro, Spectra-Physics) for energy amplification. The regenerative amplifier is composed of a special cavity design enabling the passage of a single seed pulse, from the oscillator, to pass through the Pockels cell and into the cavity. Upon entering the amplifier, the pulse is first temporally stretched in order to prevent the catastrophic self-focusing of the light onto the Ti:sapphire crystal. The pulse is amplified and recompressed by a grating compressor. The output power of the amplifier is 2.5 W and produces pulses of 46 fs in duration at a repetition rate of 5 kHz. The amplifier is pumped by a 30 W frequency-doubled Nd:YLF (Empower, Spectra-physics, 527 nm) laser.

5.3 Experimental Setup

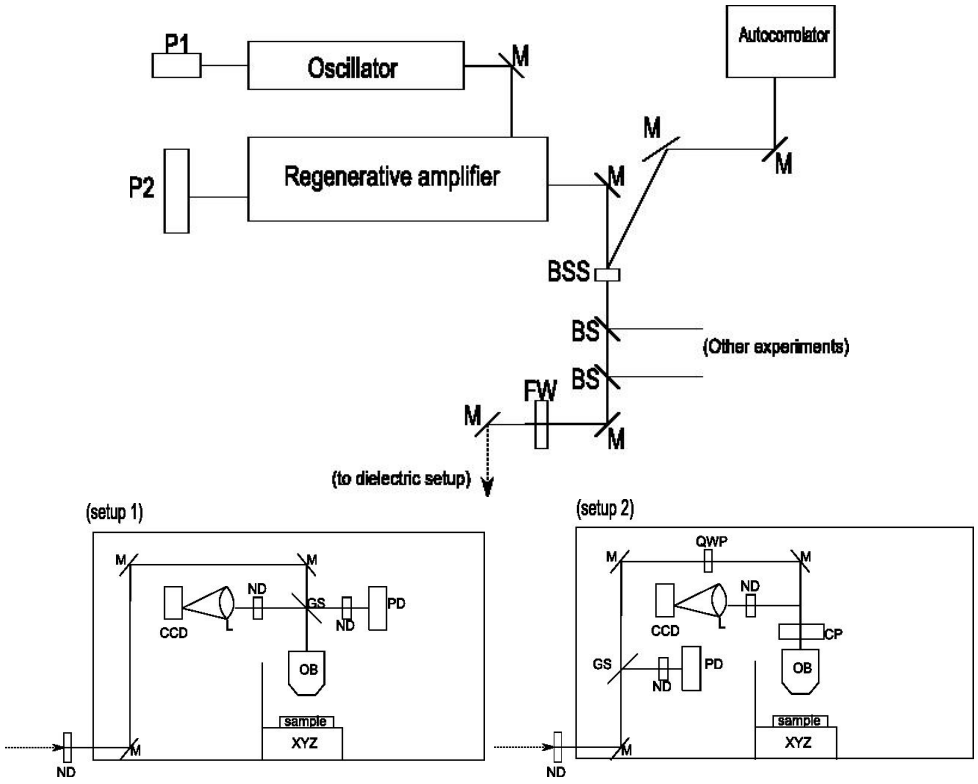

Figure 5.1: Experimental setup: Optical table and dielectric setups. The optical elements placed in the beam path are: plane mirrors (M, r = 97.5%), beam sampler (BSS), beam splitters (BS), filter wheel (FW), neutral density filters (ND), glass slide (GS), fast photodiode (PD), plano-convex lens (L) with f = 100 mm, a CCD camera (CCD) and a microscope objective (OB). In setup two, a quarter-wave plate (QWP) and a cube polarizer (CB) are added to control the power.

The dielectric setup is mounted on an optical breadboard held in an upright position and bolted to the optical table. At the output of the laser, a small percentage of the beam is reflected by a beam sampler (BSF10-B1, Thorlabs, 650-1050 nm) and directed into an autocorrolator for beam diagnostics. The transmitted light then proceeds into the dielectric setup and passes through a gradient neutral density filter (Thorlabs, NDC-100C-4M) to control the power delivered to the focal plane. The power is further attenuated by additional neutral density filters. The laser beam is directed by a series of mirrors (silver coated, PF10-03-P01, Thorlabs) into the back aperture of the microscope objective

(10x-0.25 NA, f = 16.5 mm, Newport). A glass slide is placed at 45° before the BA (setup1), to reflect a small percentage of the incident light to monitor power using a fast photodiode (PDA100A, Thorlabs, 400-1100 nm). A series of ND filters, placed in front of the photodiode, ensures a linear response. The photodiode is calibrated at the start of each experiment to obtain a linear relation between power and voltage that will be used throughout the experiments to determine the energy delivered to the focal plane.

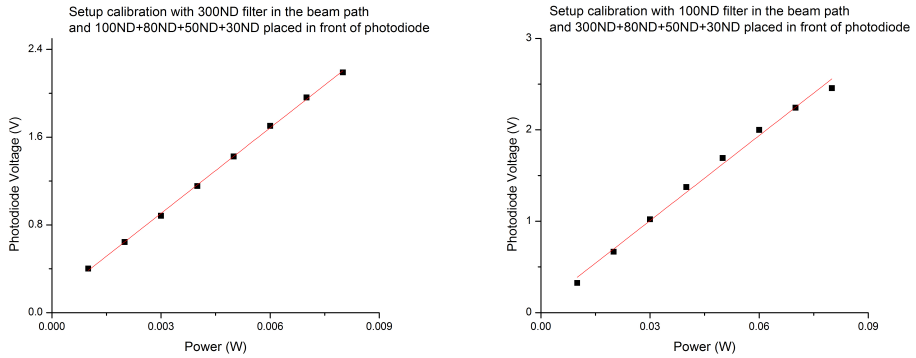

Figure 5.2: Calibration graphs of the photodiode using different ND filters in the beam path and in front of the photodiode. Both calibration were taken with the same gain of 10dB. Multiple points were taken to extrapolate linear relation and verify the linear response of the photodiode. The R^2 value of each graph are nearly 1; indicating a good linear response and accuracy of the measurements.

The light traveling through the microscope objective is focused onto the sample. From the sample's surface, a small percentage of the light is reflected in the backward direction, travels through the microscope objective and exits the BA where it is reflected by the glass slide and focused (Thorlabs, f = 100 mm, plano-convex lens) onto a CCD camera (MCE-B013-US, Mightex) in order to determine the sample's surface. When the camera is placed at the focus of the lens, light from the surface is well focused resulting in a pair of concentric dots being detected by the CCD camera. Light reflected from the surface is well collimated by the objective which, when focused by the lens, gives the smallest spot size. The spot size varies significantly for light reflected above or below the surface. As the light reflected is not properly collimated at the BA of the objective with the light coming out either convergent or divergent resulting in larger dots on the CCD when focused by the lens.

Some experiments required the setup be modified such that the light polarization be changed or the electric field of the linearly polarized light be reduced (setup 2). In order to change the polarization (or the electric field) of the light delivered to the focal plane, a quarter-wave plate (WPQ05M-780, 780 nm, Thorlabs) and a cube polarizer (CM1-PBS252, 620-1000 nm, Thorlabs) were introduced in the beam path.

5.3.1 Autocorrelator and pulse duration

The pulse duration entering the dielectric setup is monitored by a single shot autocorrelator capable of precisely measuring the pulse duration in the range of 30 - 150 fs. In this technique, the output beam is split into two seperate beams. The two beams, after a time delay, are then focused into a nonlinear medium (BBO crystal). The two beams entering the BBO crystal generate a second harmonic (SH) signal in the forward direction due to momentum conservation. As the time delay between the pulses is varied, the intensity of the SH signal changes. Signal is maximum when there is a temporal overlap and drops off gradually moving to the extremities. An autocorrelation in time is therefore transformed into a spatial intensity distribution.

$$A_c(\tau) = \int_{-\infty}^{\infty} I_s(t) I_r(t-\tau) dt \tag{5.1}$$

where A_c is the SH signal intensity, I_s is the intensity of one of the beams, and $I_r(t-\tau)$ is the intensity of the delayed pulse.

In a single shot autocorrelator, the intensity for all delays are imaged simultaneously. The resulting SH signal and spatial intensity distribution is captured by a CCD camera to give an autocorrelation trace of the pulse. The measurement of the pulse duration is done from the evaluation of the spatial delay which was transformed from the time delay.

The relation between the spatial distribution and the pulse duration is given by the following relation, assuming a gaussian beam profile.

$$\tau = \frac{\Delta\omega \sin(\Theta)}{\sqrt{2}c} \tag{5.2}$$

where $\Delta\omega$ is the vertical width of the trace, τ is the pulse duration, and Θ is the intersecting angle between the two beams. From this technique, the pulse duration from the regenerative amplifier was determined to be 46 fs.

For accurate evaluation of the pulse duration delivered to the focal plane, necessary steps were taken to determine the pulse duration at the BA. In order to mimic the conditions for which the pulse travels before entering the BA, all of the dispersive optical elements located in the beam path before entering the objective, with the exception of the beamsplitters, were placed in the autocorrelator's beam path. From this approach, the measured pulse duration at the BA was found to be 52 fs.

To include the dispersive effect of the two beam splitters on the pulse duration, the Sellmeier's equation was used in order to determine the dispersion [105].

$$n(\lambda_l) = \sqrt{1 + \sum \frac{A_j \lambda^2}{\lambda^2 - B_j}} \quad (5.3)$$

where A_j and B_j are parameters characteristic to the material and λ_l is the laser's central wavelength.

From equation 5.3, the refractive index of BK7 is found to be 1.51 (see Chapter 4 for the complete treatment) for the central wavelength of 800 nm. The group velocity dispersion (GVD) of BK7 was calculated to be of 50.6 $\frac{fs^2}{mm}$ (refer to Chapter 4). The beamsplitters were measured to have a combined thickness of 6 mm, giving a total group delay dispersion (GDD) of 303.6 fs^2. The pulse duration, including the beamsplitters, was calculated using the dispersive pulse broadening equation [84, 107].

$$\tau = \tau_o \sqrt{1 + (\frac{GDD}{\tau_o^2} 4 \ln 2)^2} \quad (5.4)$$

where τ_o is the pulse duration before entering the dispersive medium.

From equation 5.4, the pulse duration at the BA is calculated to be of $\tau = 55$ fs.

To change the laser polarization, a quarter-wave plate or a half-wave plate was introduced in the beam path along with a cube polarizer. This resulted in the further broadening of the pulse which was finally calculated to have a duration of 72 fs.

5.3.2 Energy deposition and focus properties

The calibration of the photodiode is done by measuring the average laser power, with the power meter, and associating it with the voltage from the photodiode.

The average laser power, P_{ave}, being measured by the power meter is given by the following relation

$$P_{ave} = Ef \tag{5.5}$$

where E is the pulse energy and f is the repetition rate of the amplifier.

The pulse energy, E, is given by

$$E = \frac{P_{ave}}{f} \tag{5.6}$$

For surface ablation, the peak intensity at the focal spot must be determined since it is the intensity that determines the dominant regimes of photoionization that occurs during the ablation process. In order to calcute the peak intensity, the laser peak power, P_{peak}, is given by

$$P_{peak} = \frac{E}{\tau} = \frac{P_{ave}}{\tau f} \tag{5.7}$$

where E is the pulse energy and τ is the pulse duration.

The intensity at the focal spot is given by

$$I = \frac{P_{peak}}{A} \tag{5.8}$$

where A is the focus area.

Assuming no aberrations and that the objective's spot size is diffraction limited, the spot size is given by [71]

$$D(x, y) = \frac{1.22\lambda}{NA} \tag{5.9}$$

where λ is the laser's central wavelength and NA is the numerical aperture of the objective.

For a laser with a central wavelength of 800 nm and with the use of a 10x objective with a NA of 0.25, the spot size is calculated to be of 3.904 μm.

The modified region during the ablation process greatly depends on the extent of the length of the confocal parameter [41, 105]. In surface laser ablation experiments, knowing the value of the confocal parameter gives the margin of error in which the sample's surface must be located in order to have accurate data. In the event that the sample's surface finds itself outside the confocal parameter, the threshold energies would be erroneous and the photoionization rate would decrease significantly due its n-th order dependance on intensity.

The confocal parameter, b, is given by [41]

$$b = 2.74\frac{n\lambda}{NA^2} \tag{5.10}$$

where n is the refractive index of the medium, λ is the central wavelength of the laser and NA is the numerical aperture of the objective.

For a 10x objective with a NA of 0.25 and taking $n = 1$ (air), the confocal parameter is $\approx 35\mu$m. The sample should then be located within that length in order to ensure accurate data on the threshold values.

As previously mentioned, the process of photoionization depends on the intensity delivered to the focal plane. For the energy range of 1 nJ to 10 μJ used in the experiment and pulse duration at the BA found for the different arrangements, the approximate values for the intensity are:

$$I_{54.5fs}(x, y) = 1.5 \times 10^{11}\frac{W}{cm^2} - 1.5 \times 10^{15}\frac{W}{cm^2} \tag{5.11}$$

$$I_{75.7fs}(x, y) = 1.1 \times 10^{11}\frac{W}{cm^2} - 1.1 \times 10^{15}\frac{W}{cm^2} \tag{5.12}$$

From these intensities and the theory brought forth in Chapter 1, it is clear that ablation within the lower range of energies is dominated by multiphoton ionization while at higher energies, it is dominated by tunnel ionization.

It is important to note that the intensities mentioned above are only rough estimates and are not accurate since the pulse duration used for the calculations was determined for the light before it entered the back aperture of the objective. The broadening of the pulse by the optical elements of the objective was not considered due to the complexity of the

task (virtually impossible). In addition, the spot size measured experimentally (later in this Chapter) was found to be slightly larger than that of the diffraction limited spot size. For these reasons, the intensities calculated (above) are expected to be relatively lower.

5.4 Results: Polymer Studies

For this research, the transparent material chosen for the study of light-matter interaction was PMMA or Poly(Methyl Methacrylate) as shown in figure 5.3.

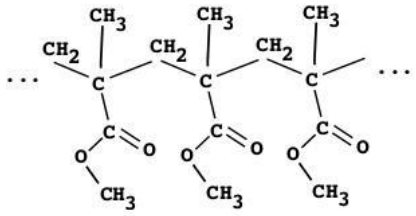

Figure 5.3: PMMA polymer structure [109]

PMMA was chosen for its composition since methacrylate is commonly used to make contact lenses. Allowing the results on PMMA to be later compared to those obtained from the experiments on the contact lenses. The link between the composition of the materials could later help to study the transition of light-matter interaction from harder polymers to softer polymers, reducing the amount of unknown parameters.

The bandgap energy of the polymer is known to be 3.55 eV [110], making the photoionization of PMMA a 3-photon process when using an excitation source with a central wavelength of 800 nm (photon energy is 1.55 eV).

5.4.1 Line Ablation(PMMA)

To determine the energy threshold values for line ablation, the light was focused at the surface of the PMMA samples which were placed on a motorized stage and moved in a sideways motion at a constant velocity so that every section in the entire sample is exposed to a certain number of laser shots. This can be varied by changing the speed

of the translation stage. The values obtained for the threshold were observed to be dependant on the velocity of the stage vis-a-vis the number of laser shots delivered to the interaction region.

The energy thresholds were determined by fixing a stage velocity and changing the energy between each successive lines which were seperated by a 50 μm interval. This process was repeated for different velocities to find threshold values as a function of number of shots per micron. The energy range used in the experiments ranged from 10 μJ all the way down to 1 nJ. The energy was lowered by steps of 500 nJ for the higher energy range (10 μJ - 2.5 μJ), 100 nJ for the middle energy range (2.5 μJ - 1 μJ), and 50 nJ for the lower energy range (1 μJ - 1 nJ).

The threhold energies for ablation were obtained by determining the last energy where ablation occured using a microscope to look at the surface of the PMMA sample (Figure 5.4).

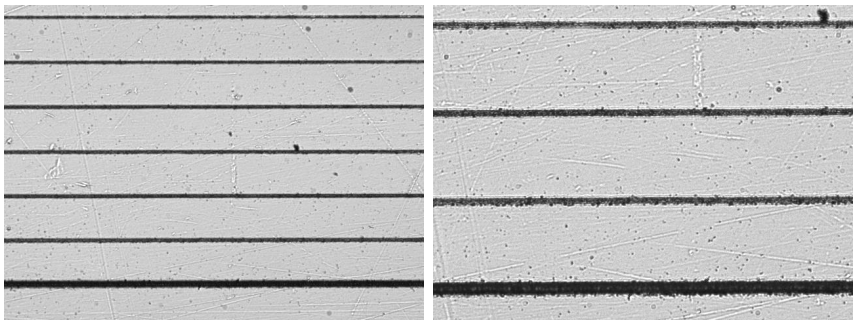

Figure 5.4: Line ablation at the PMMA's surface using linear polarization oriented parallel to the stage motion. Debris(black dots) can be observed around the ablation craters resulting from the ejection of material off the PMMA's surface during the ablation process. Images were taken with a (left) 10x dry objective and (right) 20x dry objective.

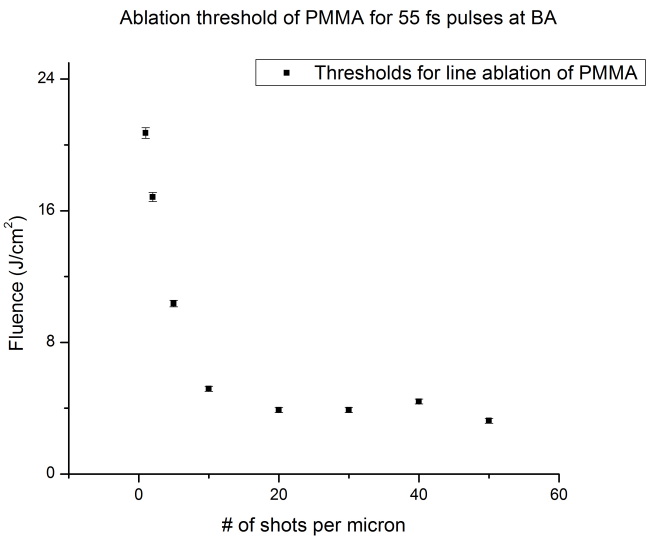

Figure 5.5: Graph of threshold fluence required to initiate the ablation process versus the number of shot per micron.

Results showed a decrease in the fluence threshold, required for ablation, as the number of shots delivered to the interaction increased until it eventually reached a saturation point (see Figure 5.5). This behavior can be explained by the shot-to-shot memory of the PMMA sample and results in the lowering of the bandgap energy required for photoionization [39]. Shot-to-shot memory indicates that the material remembers the influence of the previous laser shot, within the region, leading to a reduction of the bandgap. When the next pulse arrives, it requires less energy to preferentially ionize that region thereby lowering the threshold.

5.4.2 Single Shot Ablation (PMMA)

Experiments of single shot ablation of PMMA were conducted using the same setup and method as line ablation with the lone difference being that the stage was at rest during the ablation process. To manually control the number of shots delivered to the focal plane, the operational mode of the laser was changed from continuous to single shot. The single shot experiments were done using two different pulse durations.

Characterization of the modified regions

The delivery of short pulses of light at a polymer's surface may cause ablation if the laser fluence, ϕ_o, exceeds a certain fluence threshold, ϕ_{th}, required to eject material from the surface [111, 112]. The ϕ_{th} value is characteristic to the material and on the number of laser shots delivered to the region.

The modified regions caused by ablation, assuming a gaussian profile of the laser beam, is related to the laser fluence by the following equation [111]

$$D^2 = 2\omega_o^2 \ln(\frac{\phi_o}{\phi_{th}}) \tag{5.13}$$

where D^2 is the square diameter of the modified region and ω_o is the $1/e^2$ beam radius of the gaussian beam. The laser fluence, ϕ_o, is given by

$$\phi_o = \frac{2E_{pulse}}{\pi\omega_o^2} \tag{5.14}$$

where E_{pulse} is the pulse energy.

Experimentally (beside using a knife edge technic), the true spot size at the surface can be estimated from the graph of D^2 versus $\ln(E_{pulse})$ as there is a linear relationship between both E_{pulse} and ϕ_o. The slope of such a graph gives an approximate $1/e^2$ radius value for a gaussian beam [111, 112]. In our experiments, the back aperture of the microscope objective is overfilled, giving the beam a flat top-like profile. Nonetheless, it gives an appoximate value to the spot size of the objective.

In order to find the spot size at the surface, the dimensions of all the ablation holes, from the SEM pictures, were measured using the software imageJ (Figure 5.6).

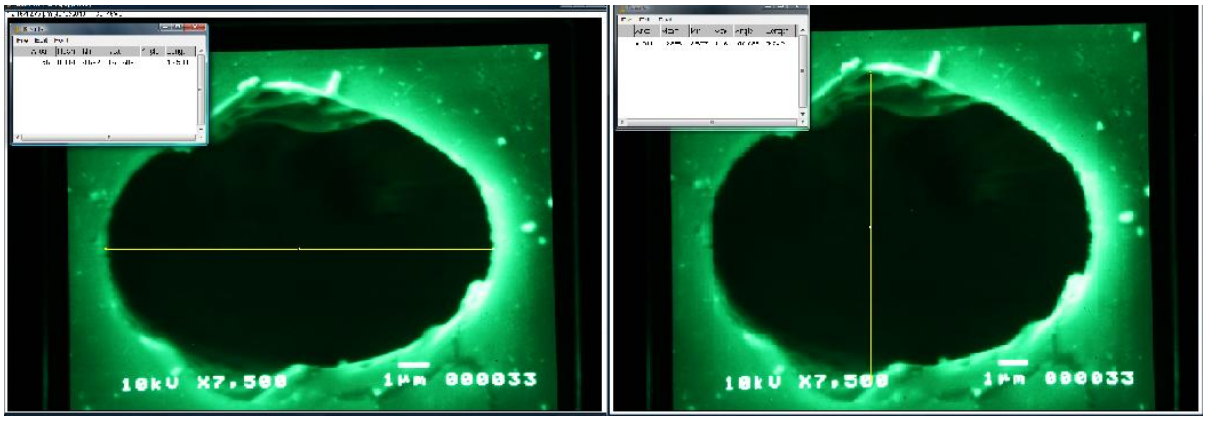

Figure 5.6: Measurement of the modified regions using ImageJ. The scale of the software was matched to that of the SEM scale in the bottom right of the pictures.

Pulse duration of 55 fs

The dimensions of the modified regions were measured from the SEM images taken of the ablation craters made from the 2-shot and 5-shot experiments.

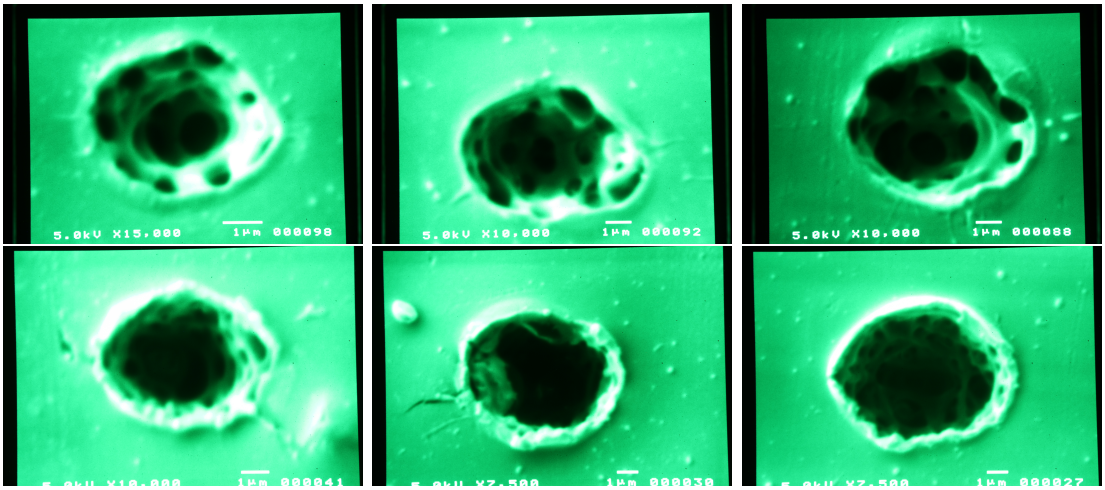

Figure 5.7: SEM pictures of the ablation craters made by (top) 2 shots and (bottom) 5 shots. With energies of (left) 1.8 μJ; (center) 5.4 μJ; (left) 6.9 μJ

From these measurements, D^2 versus $\ln(E_{pulse})$ graphs were plotted; one for the 2-shot and the other for the 5-shot measurements.

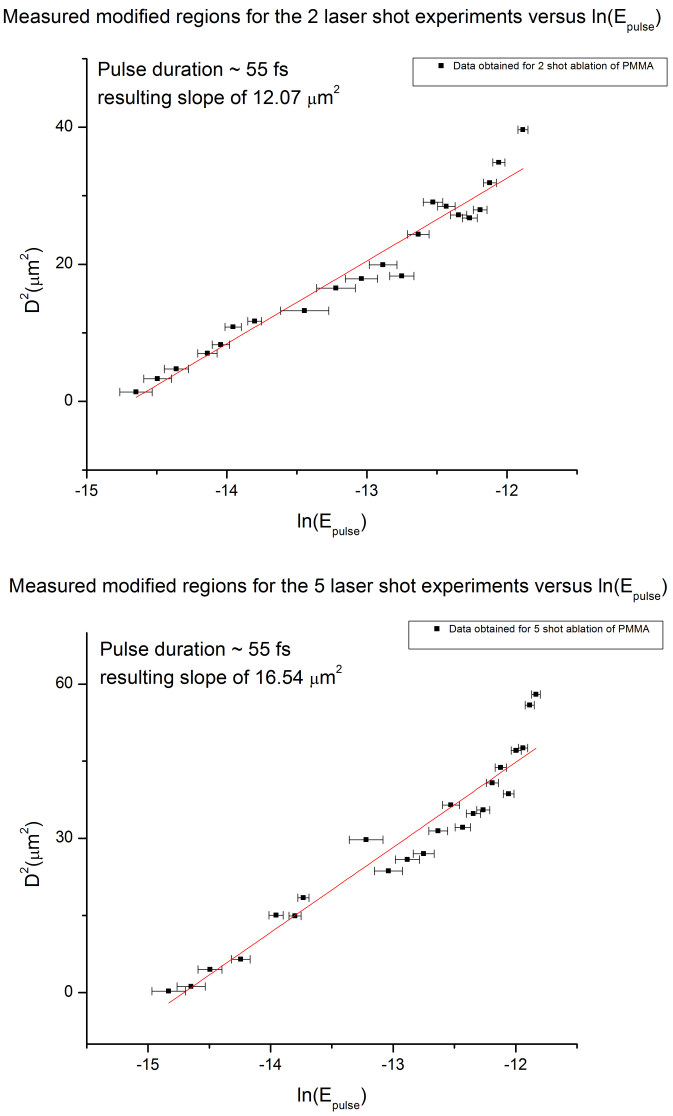

Figure 5.8: Graphs of D^2 versus $\ln(E_{pulse})$; (top) for 2 shots and (bottom) 5 shots. From the slope, the beam radius is obtained: 2.46 μm from the 2-shot and 2.87 μm from the 5-shot graph.

From each of the graphs, a linear fit was extrapolated and a value for the slope was obtained. From equation 5.13, the slope of a graph of D^2 versus $\ln(E_{pulse})$ is equal to $2\omega_o^2$. The slope of both these graphs gave two slightly different values for the beam radius. Therefore, an average was taken giving an estimated beam radius of 2.67 μm. The estimated spot size is 5.34 μm for the light focused at the surface of the PMMA sample

using a 10x and 0.25 NA dry objective.

Care had to be taken while measuring the spot size from an ablation hole since its size depends on pulse energy. Ablation occurs when the pulse energy is above the threshold value. Therefore, when the pulse energy is made higher than the threshold value, ionization occurs over larger spatial dimensions within the focal volume as shown in Figure 5.9.

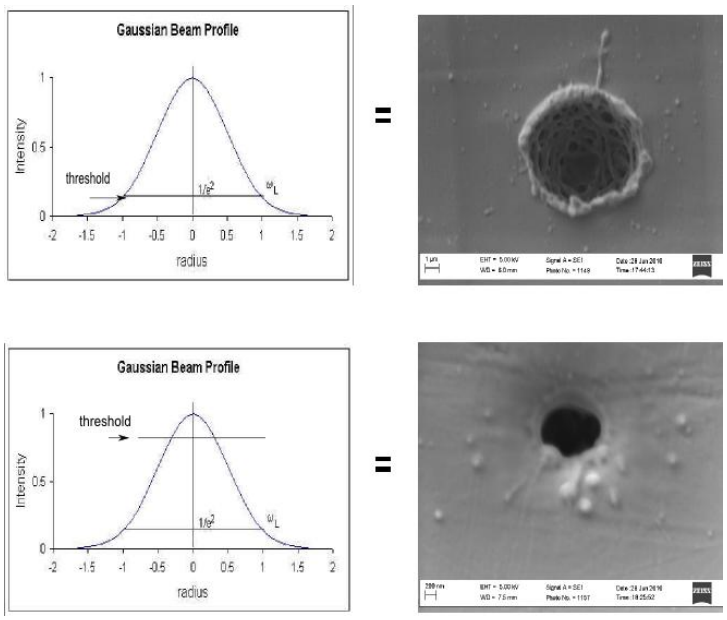

Figure 5.9: Demonstrates the size of the ablation craters depending on how much over threshold the energy is. At high energy (top), the intensity is high and the peak and wings both contribute to the process of photoionization. At low energy (bottom), only the peak of the beam is above threshold resulting in an ablation crater smaller than the calculated spot size.

The experimentally obtained D^2 values, measured from the SEM pictures, were plotted as a function of laser fluence, ϕ_0, (knowing the spot size); for both 2 and 5 laser shot surface ablation of PMMA, see Figure 5.10.

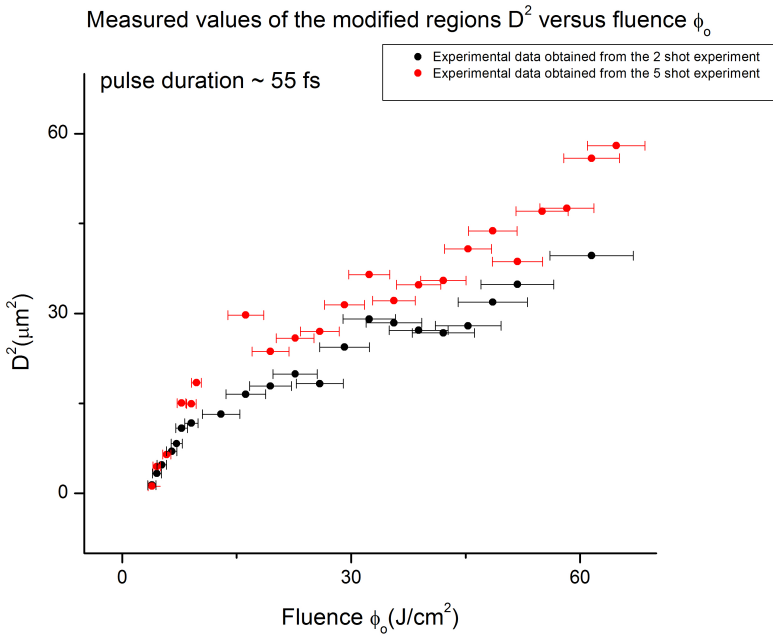

Figure 5.10: Graph containing the measured values of the modified regions as a function of laser fluence.

Ablation threshold

Ablation thresholds were experimentally determined for 1, 2, and 5 laser shots by examining the PMMA samples using an optical and SEM microscope.

Pulse duration of 55 fs

From these threshold values, a graph was plotted of threshold fluence as a function of the number of shots delivered to the region.

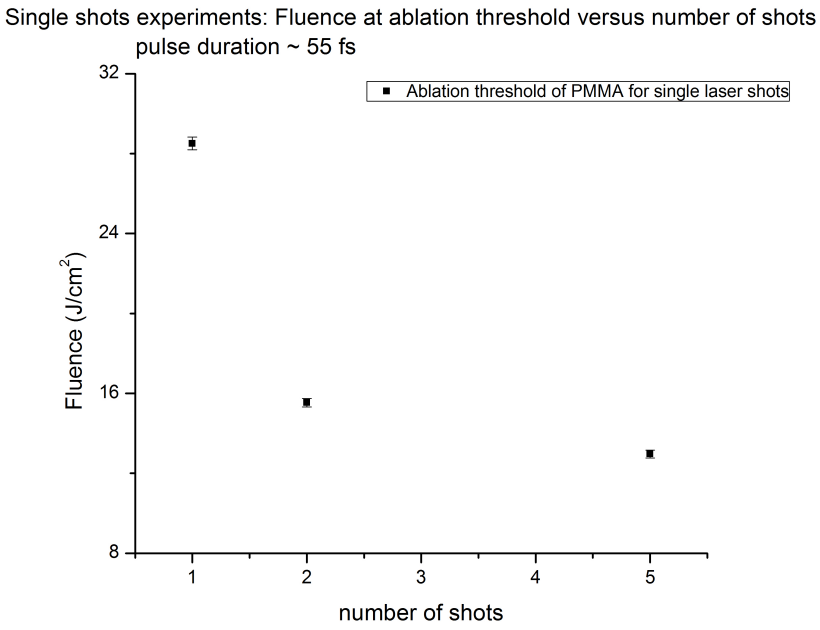

Figure 5.11: Graph: Fluence at threshold versus the number of shots

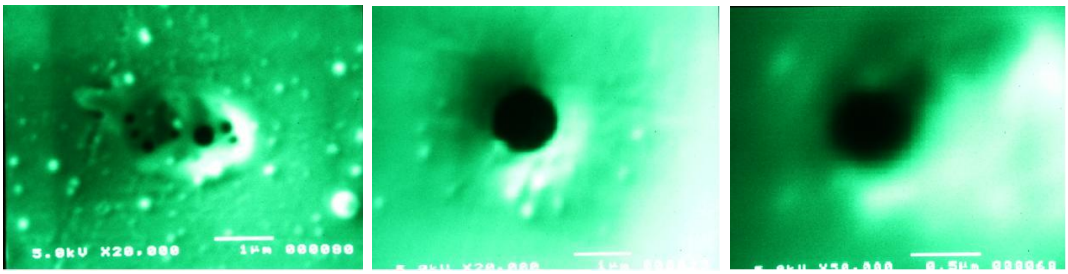

Figure 5.12: SEM pictures of the ablation craters at threshold; (left) threshold energy value of 798 nJ for 1-shot ablation of PMMA; (middle) threshold energy value of 475 nJ for 2-shot ablation of PMMA; (right) threshold energy value of 363 nJ for the 5-shot ablation of PMMA.

Figure 5.12 shows the SEM images of the ablation craters at threshold for 1, 2, and 5 shots. The threshold fluence decreases with the increasing number of laser shots. For areas of PMMA exposed to energies lower than threshold, the full and complete examination of the sample under an SEM revealed no modification or even an indication that a laser shot had previously been delivered unto the region. Figure 5.11 shows the

threshold fluence as a function of number of laser shots. This behavior is similar to that of the results obtained for line ablation and can be explained by the shot-to-shot memory induced in the region (refer to Chapter 1 for details of memory effect in PMMA) [39]. The examination of the sample wiyj an SEM also revealed no modifications whats so ever for areas exposed to energy lower than threshold.

Polarization dependant structures

During the course of these experiments, distinct structures were observed to form within the ablation craters upon using different laser polarizations.

Single shot ablation ($\tau = 55$ fs)

Figures 5.13-15 are SEM images of the 1 shot ablation of PMMA for different pulse energies and laser polarization. For 1 shot experiments, results already suggest that there is a polarization dependence on the structures.

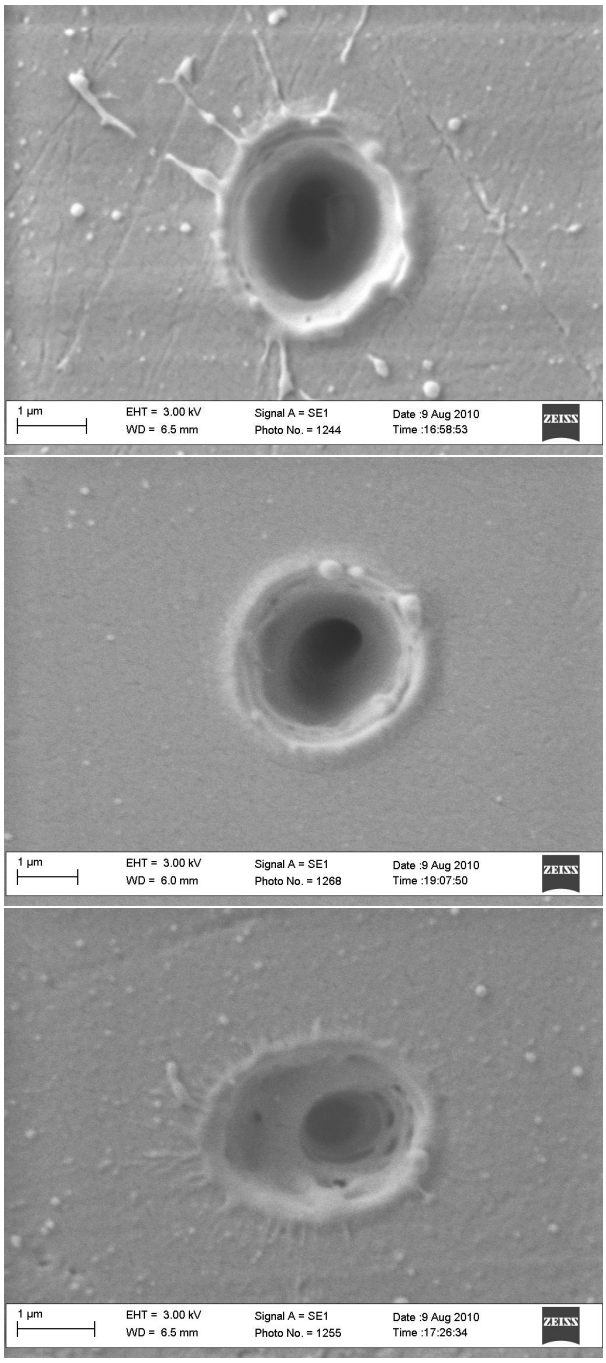

Figure 5.13: 1 shot experiment. Images taken with a SEM of the ablation craters caused by the use of different light polarizations; (top,left) linear polarization, (top,right) circular polarization, (bottom) elliptical polarization (ellipticity of 0.5). Energy was 1.33 μJ.

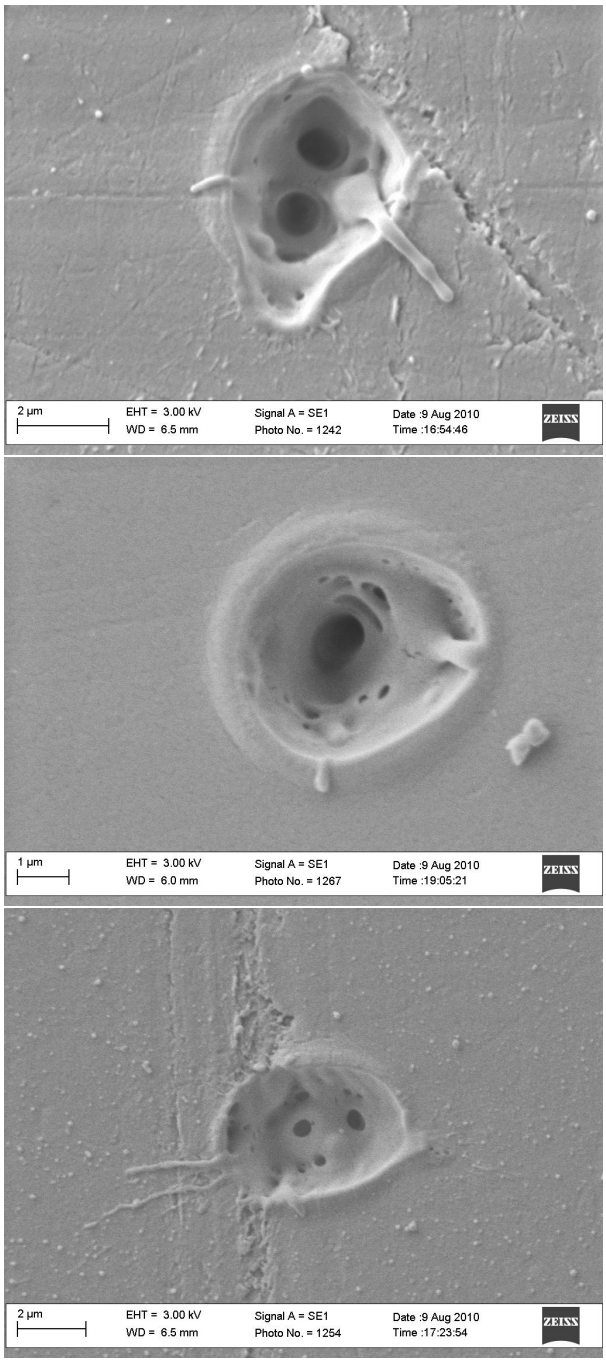

Figure 5.14: 1 shot experiment. Images taken with a SEM of the ablation craters caused by the use of different light polarizations; (top) linear polarization, (middle) circular polarization, (bottom) elliptical polarization (ellipticity of 0.5). Energy was 4.35 μJ.

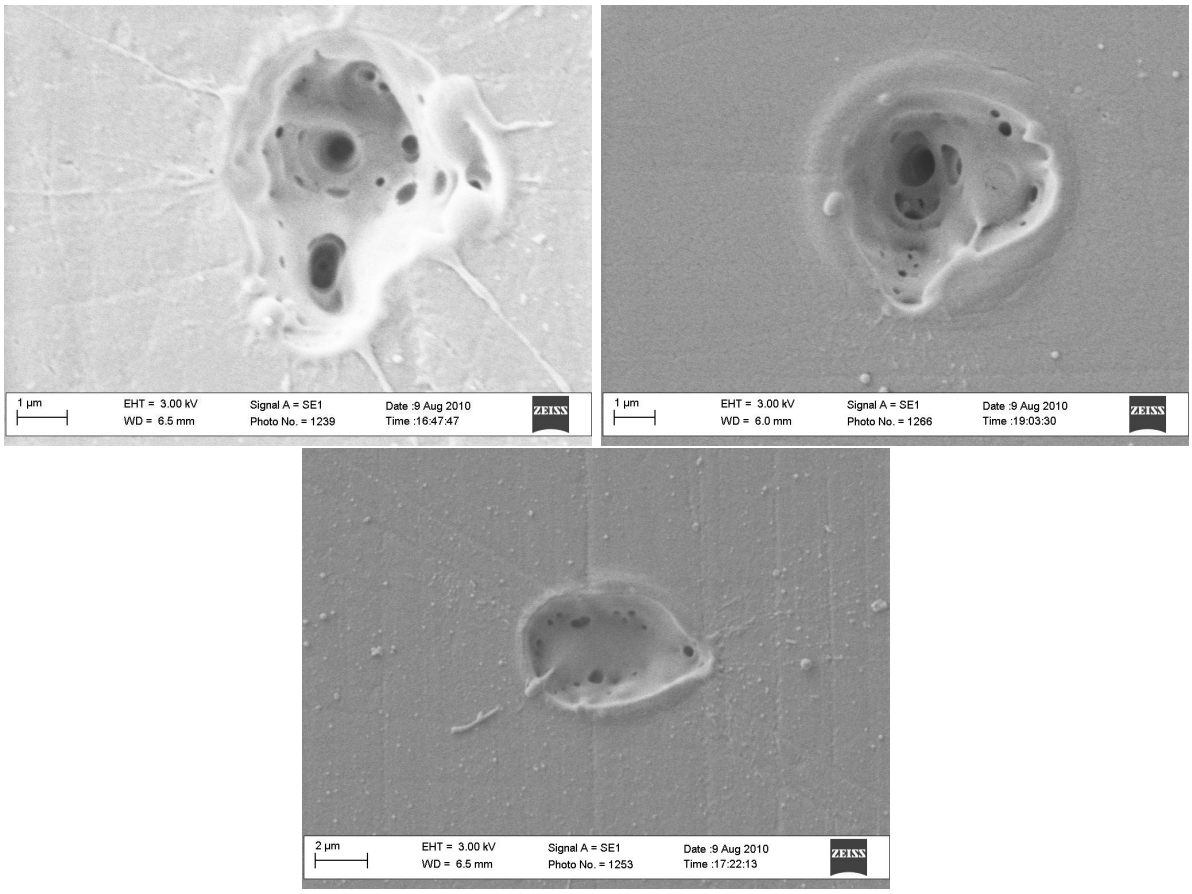

Figure 5.15: 1 shot experiment. Images taken with a SEM of the ablation craters caused by the use of different light polarizations; (top,left) linear polarization, (top,right) circular polarization, (bottom) elliptical polarization (ellipticity of 0.5). Energy was 7.25 μJ.

Interestingly from Figures 5.16-18, this observation hold true and becomes more significant as the number of shots delivered to the area is increased. In addition, the differences in the structures are observed to become more significant as the energy delivered to the region is increased.

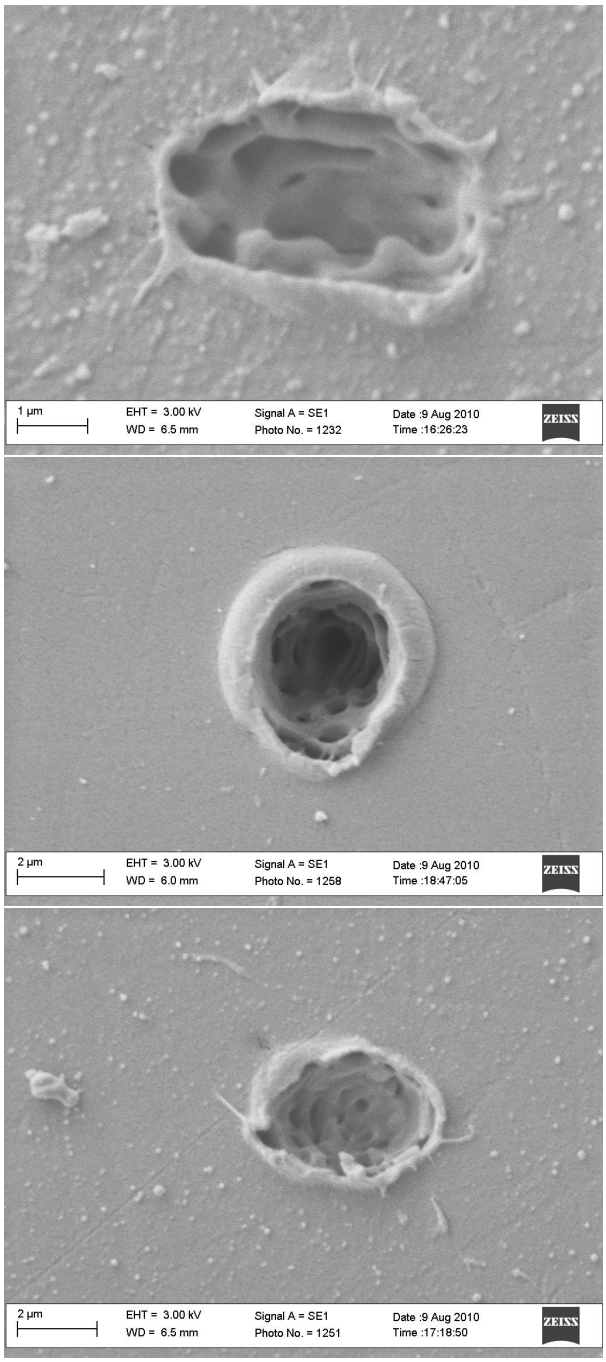

Figure 5.16: 5 shot experiment. Images taken with a SEM of the ablation craters caused by the use of different light polarizations; (top) linear polarization, (middle) circular polarization, (bottom) elliptical polarization (ellipticity of 0.5). Energy was 1.33 μJ.

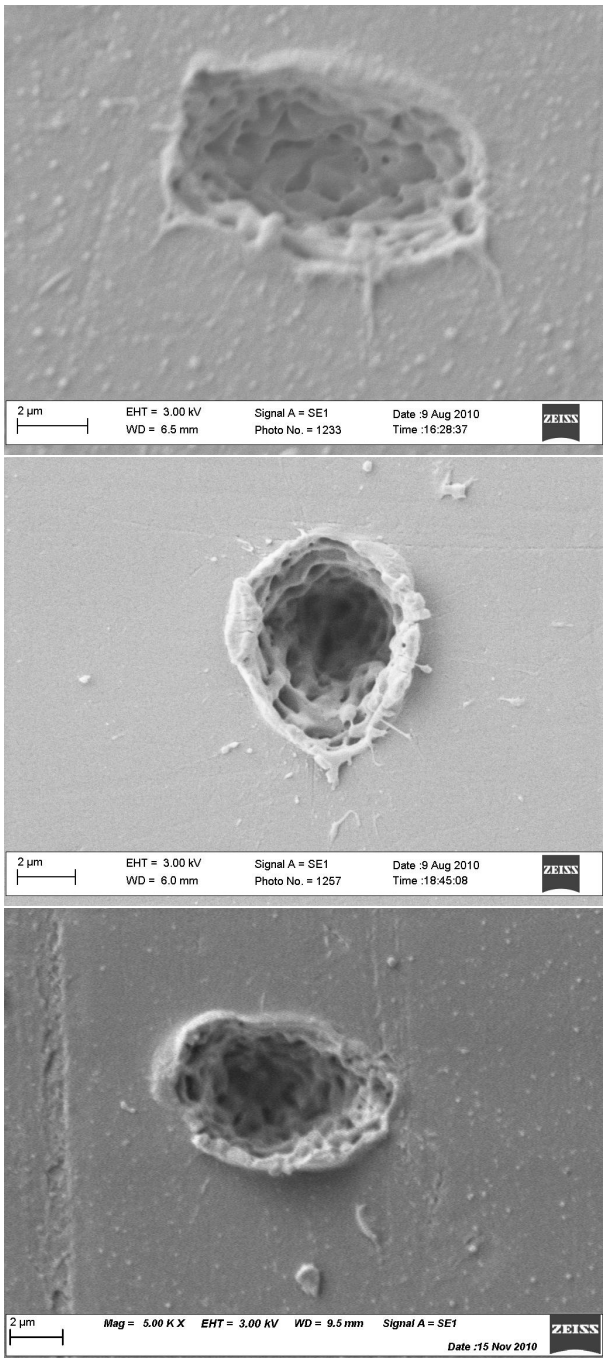

Figure 5.17: 5 shot experiment. Images taken with a SEM of the ablation craters caused by the use of different light polarizations; (top) linear polarization, (middle) circular polarization, (bottom) elliptical polarization (ellipticity of 0.5). Energy was 4.35 μJ.

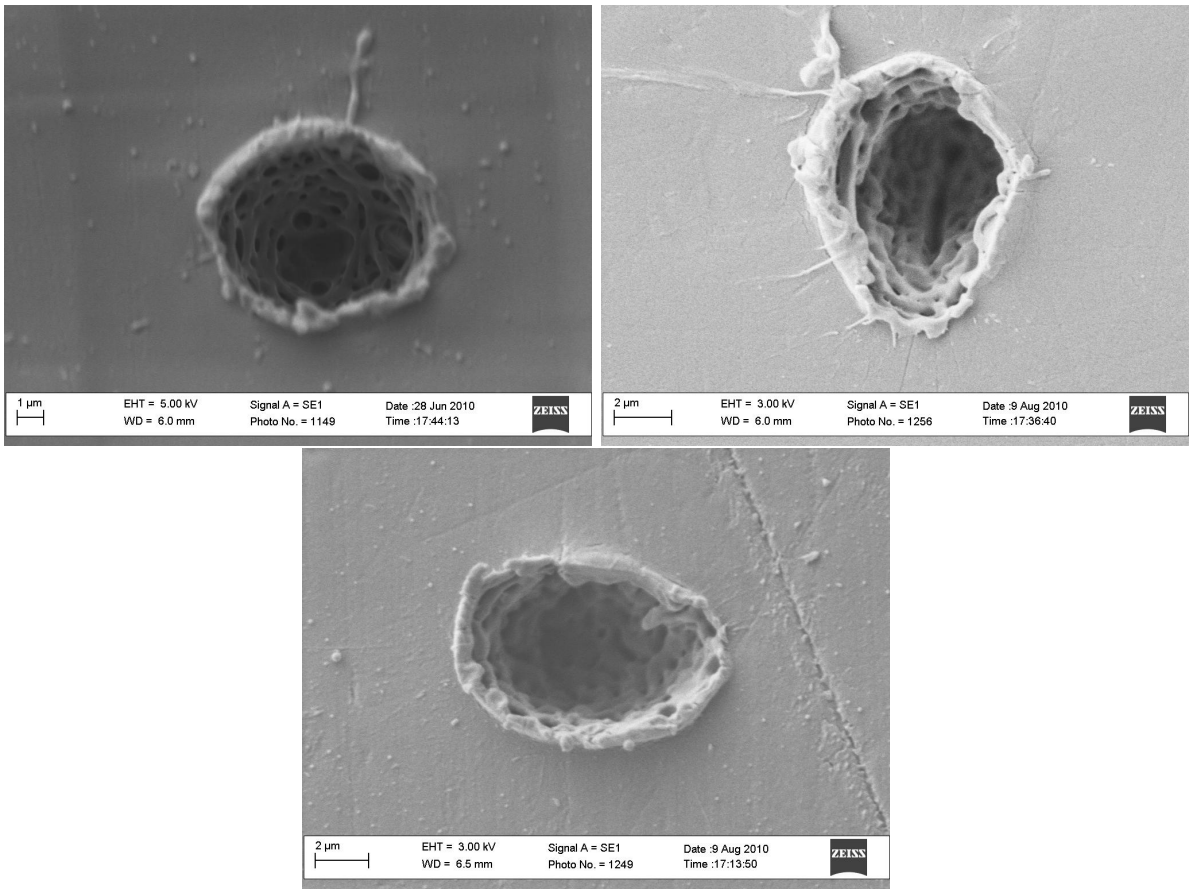

Figure 5.18: 5 shot experiment: Images taken with a SEM of the ablation craters caused by the use of different light polarizations; (top,left) linear polarization, (top,right) circular polarization, (bottom) elliptical polarization (ellipticity of 0.5). Energy was 7.25 μJ.

There were two interesting observations made; first, the shape of the ablation craters is found to be dependent on the polarization and on the number of shots delivered to the region, as shown in Figures 5.19-21. Second, 3D honeycomb structures are observed to evolve, within the craters, with each successive shot delivered to the interaction region, as shown in Figures 5.19-22.

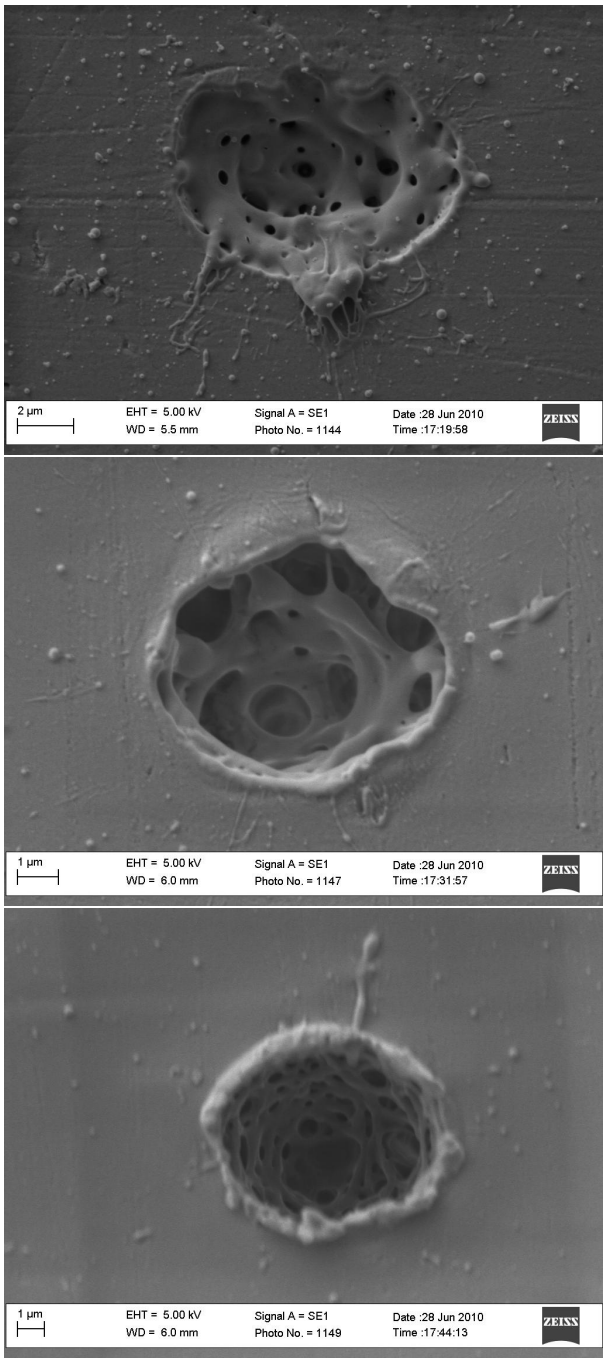

Figure 5.19: SEM images demonstrating the changes in the structures, using linearly polarized light, as the number of shots is increased; (top) 1 shot, (middle) 2 shots and (bottom) 5 shots. Energy was 7.7 μJ.

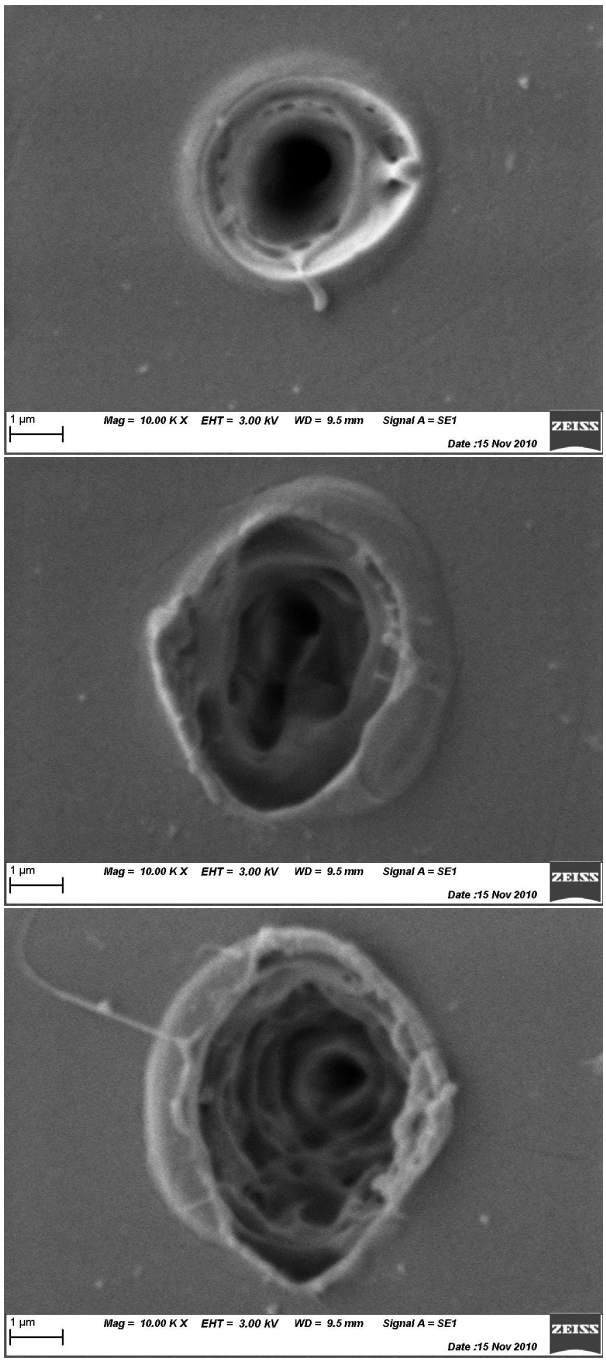

Figure 5.20: SEM images demonstrating the changes in the structures, using circularly polarized light, as the number of shots is increased; (top) 1 shot, (middle) 2 shots and (bottom) 5 shots. Energy was 2.6 μJ.

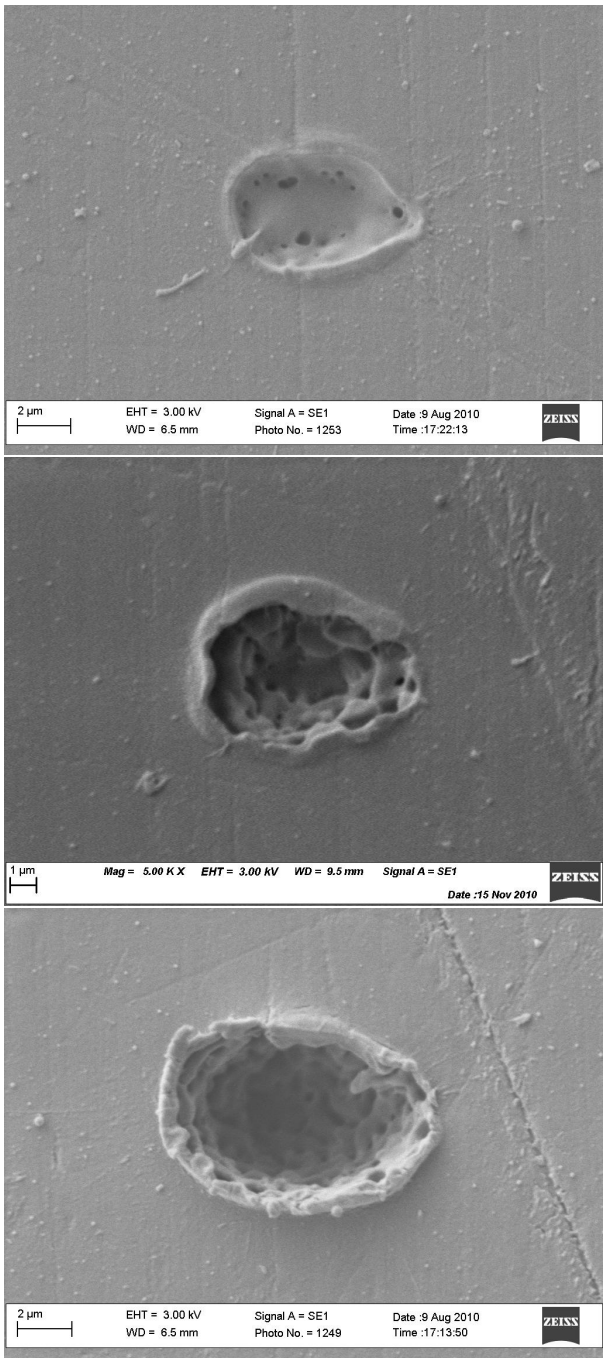

Figure 5.21: SEM images demonstrating the changes in the structures, using elliptically polarized light, as the number of shots is increased; (top) 1 shot, (middle) 2 shots and (bottom) 5 shots. Energy was 6.6 μJ.

Formation of periodic nano-structures have been observed in the ablation craters of different materials. Such as: semi-conductors, metal foils, and other polymers. The structures are generally found only at the bottom of the craters (2D stuctures, xy direction). Their formation is explained and widely accepted as being the product of light interference between the incident and scattered radiation, resulting in the formation of ripple structures located only at the bottom of the crater. In our case, the analysis of the ablation craters under an SEM, see Figure 5.22, showed the formation of structures not only at the bottom of the craters but also on the side of the holes (3D structures, xyz direction). The observation of such 3D nano-structures (like a bee hive) in the ablation craters of PMMA was highly unexpected. Previously, 3D periodic nano-structures were observed in the laser-modified regions within the bulk of fused silica glass and was explained in terms of a nanoplasmonic model that involves the interaction of the light with the confined plasma within the bulk [48]. Such a model may be extended to PMMA and we are currently investigating the mechanism responsible for such 3D structuring.

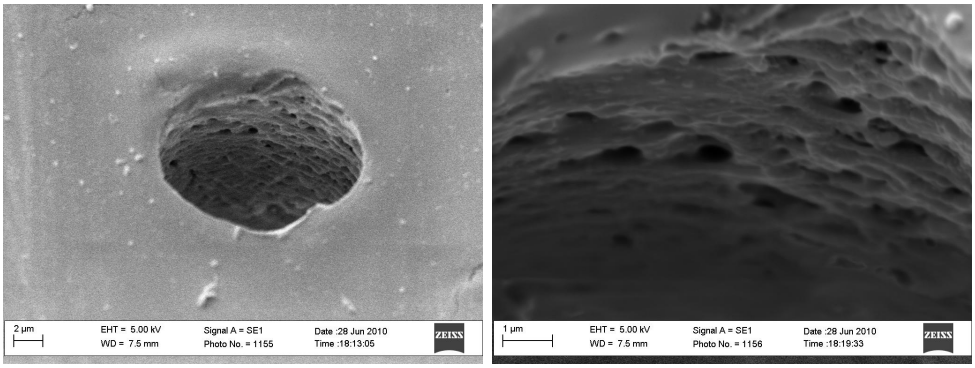

Figure 5.22: Side view of an ablation crater using linearly polarized light; with energy of 6.89 μJ and 5 shots delivered to the region.

Prefered direction to photoionization in an isotropic material (PMMA)

The analysis of the modified region from single shot surface ablation of PMMA using linearly polarized light, has shown an interesting trend in the photoionization process. Results suggest photionization of the material to occur preferentially along the electric field of the laser, resulting in an elongated crater. With the widest part of the crater always pointing in the direction of the electric field. The orientation of the elongated crater changes when modifying the orientation of the laser polarization, as shown in Figure 5.23.

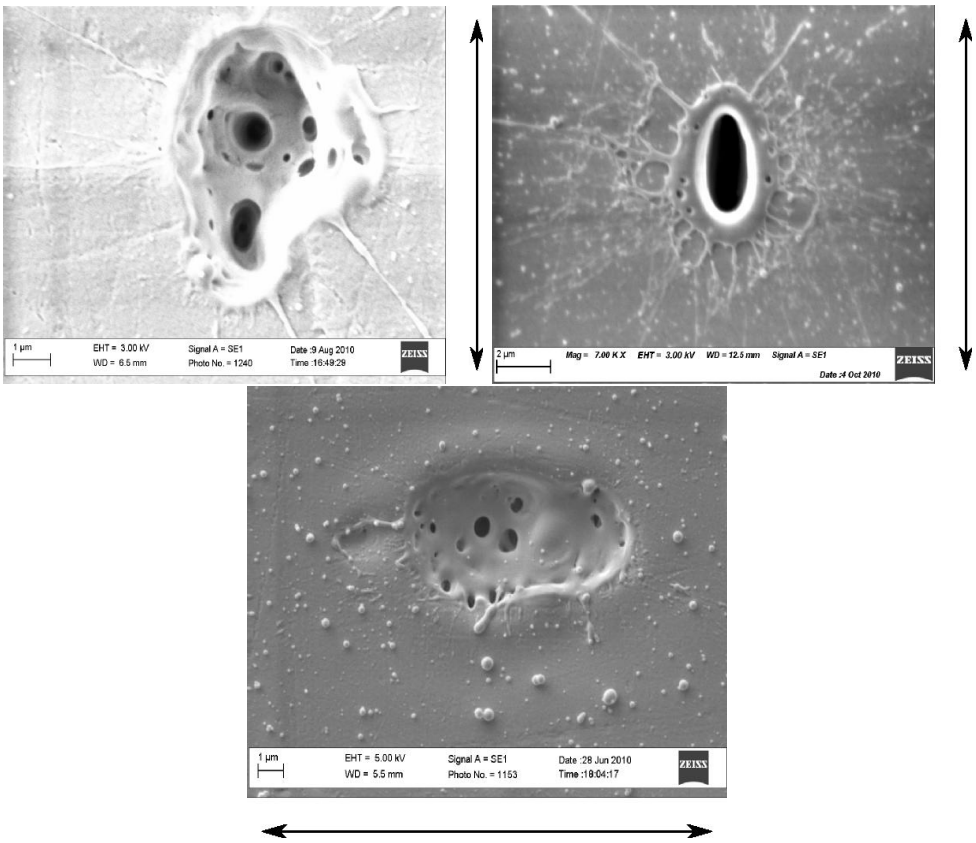

Figure 5.23: Results obtained from the ablation of PMMA using linearly polarized light, showing a prefered direction to the photoionization process along the electric field of the laser. (bottom, top-left) pulse duration of 55 fs, energy of 7.25 μJ and electric field E; (top-right) pulse duration of 72 fs, energy of 6.57 μJ and electric field $\frac{E}{\sqrt{2}}$. Located around the craters are debris and nano-droplets ejected from the surface during the ablation process (arrows pointing in the direction of the field).

PMMA is known to be an isotropic medium and therefore shouldn't exhibit a prefered direction to ionization vis-a-vis ablation. However, observations made on multiple PMMA samples, for 1 laser shot, have repetitively suggested otherwise. Observation of a preferential orientation of the ablation craters along the polarization direction could be associated with preferential photoionization of long polymer chains in PMMA. Though there is no long range order, only those chains that are aligned along the laser polarization are preferentially ionized. Such a preferential ionization has been previously observed in molecules. Since ionization is the first step to ablation, preferential ionization leaves

an imprint on the ablation crater. In PMMA the molecular chains are extremely long reaching lengths from a few hundred nanometers to a micron. Further studies with poled polymers should reveal this effect.
It is interesting to note that similar results where obtained in fused silica glass where the orientation of periodic structures formed inside the bulk material were observed to depend on the laser polarization [113]. The formation and growth of these periodic structures is explained interms of a nanoplasmonic model. The orientation dependence of the periodic structures in fused silica do not vanish as the laser focus is scanned inside the material.

Electric field orientation dependant structures (Linearly polarized light)

The purpose of this experiment is to examine the structures formed inside the ablation trails by changing the orientation of the linearly polarized while moving the laser focus. This was accomplished by introducing a $\lambda/2$ waveplate in the beam path. For convention, the orientation of the linearly polarized light will be characterized according to the displacement of the motorized stage.

With this setup, three sets of ablation lines were done, each with different speeds and orientation. One set of lines was done with the orientation of the linearly polarized light perpendicular to the motion of the stage, the second oriented to make a 45° angle with the motion of the stage, and the third set parallel.

The analysis of the ablation trails revealed significant differences when using different orientation of the linearly polarized light, as shown in Figure 5.24. From Figure 5.24, it can clearly be observed that the side of the ablation trails have a wave type pattern that comes more predominant as the orientation of the light is changed with respect to the motion of the stage. These wave patterns are thought to be a reaffirmation, like single shot, of a preferred direction to photoionization along the electric field of the laser (red arrows). Producing wave like pattern along the ablation trails and in the same direction as the laser polarization.

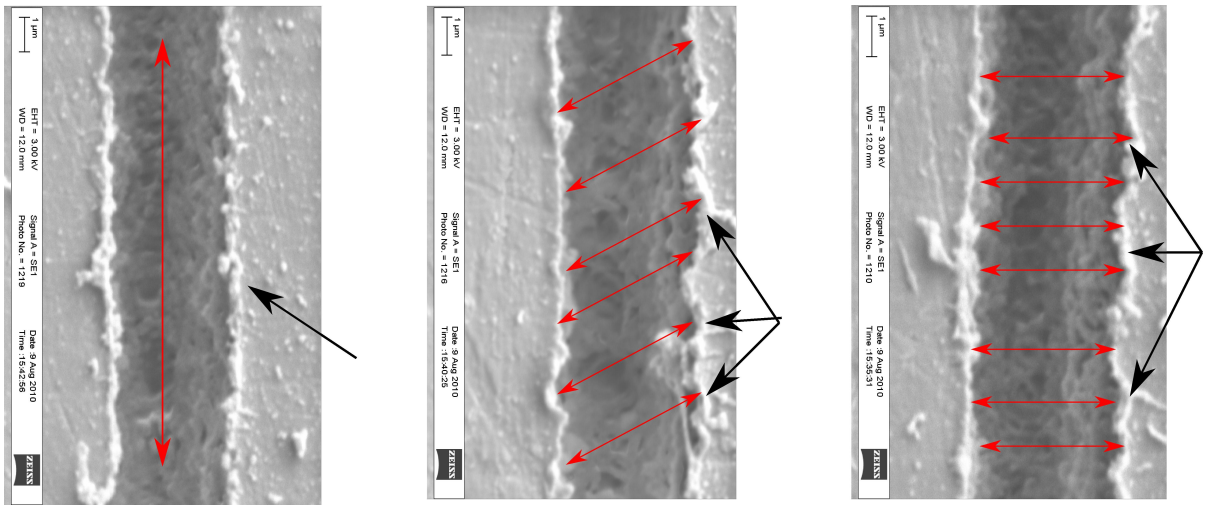

Figure 5.24: Demonstrates the cleanliness of the ablation trails, with energy of 985 nJ, depending on the orientation of the linearly polarized light with respect to the motion of the stage: (left) parallel, (center) 45° and (right) perpendicular. All three ablation lines were done with the same stage velocity of 1 mm/s. As the arrows point out in the pictures, there is wave like patterns along the ablation trails that appears when is oriented differently compared to the motion of the stage. Growing outwards in the direction of the laser polarization (red arrows). Suggesting a preferred direction to photoionization along the electric field of the laser.

For an indepth study of the ablation craters we used linearly polarized light that was oriented at 45° with respect to the motion of the stage and investigated the structures written for different energies and speeds. The electric field of the linear polarized light is diminished by $\sqrt{2}$ along the axis compared to the pictures taken in Figure 5.24. The structures resulting from this experiment were examined using an SEM.

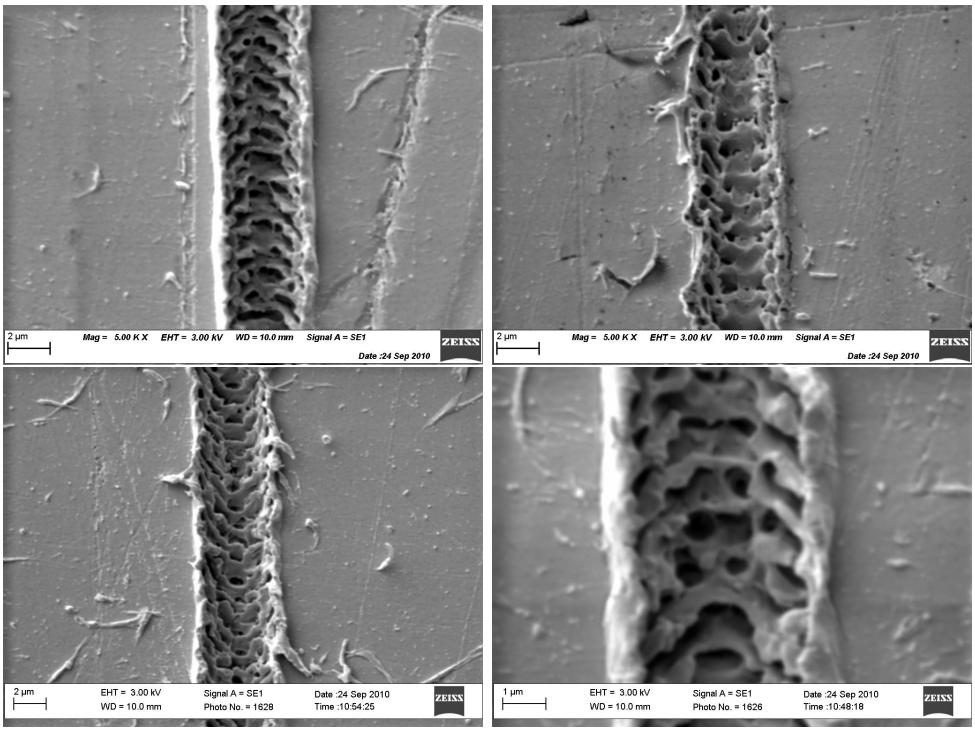

Figure 5.25: Pictures taken with a SEM of the structures remaining at the bottom of the craters following the process of ablation. The linearly polarized light was rotated to make a 45° angle with the motion of the stage. All pictures are taken at a speed of 5 mm/s. With energies of: (top,left) 934 nJ; (top,right) 1.13 μJ; (bottom,left) 1.27 μJ; (bottom,right) 1.33 μJ.

From figure 5.25, the structures found at the bottom of the ablation craters, at first glance, appear to be periodic and evenly spaced with an average distance of ≈ 1 μm (see Figure 5.26). Interestingly the spacing of the structures was observed to be independent of energy, higher than the threshold value, when ablated with same stage velocity.

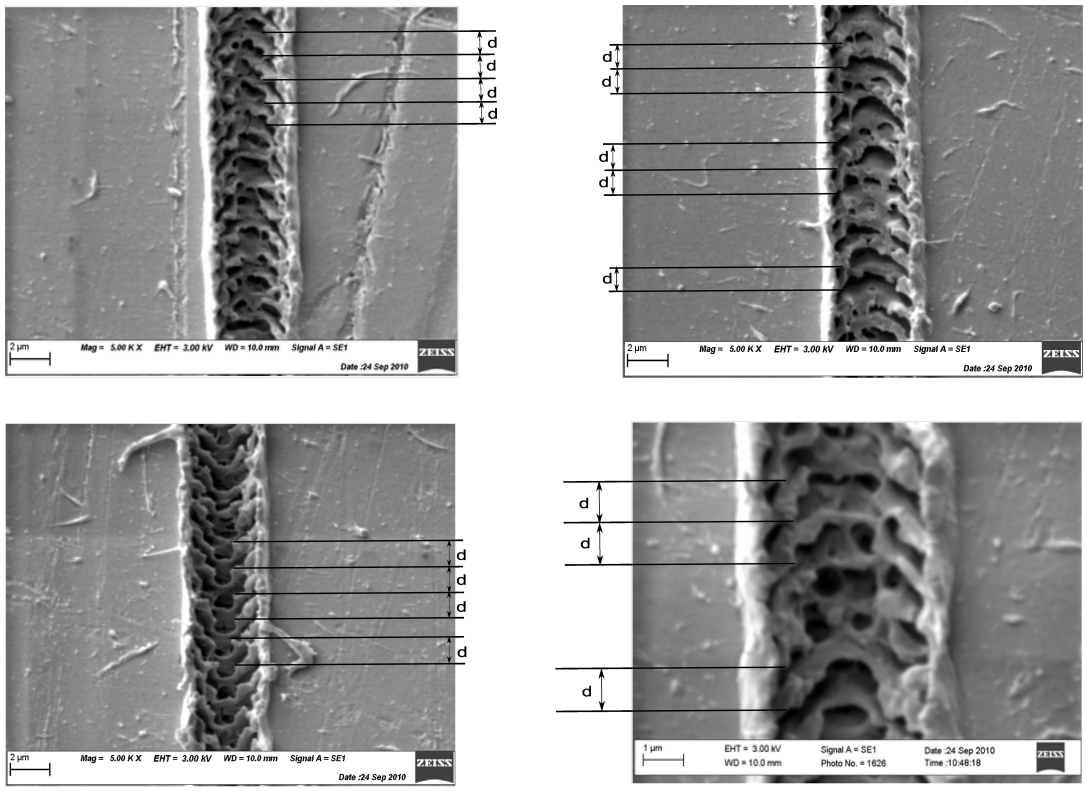

Figure 5.26: For energies higher than threshold, some kind a periodicity can be distinguised within the ablation craters. This periodicity is observed to be indenpendent of the energy used for ablation using the same stage velocity. Using the appropriate software, the average distance, d, between the ripples was found to be ≈ 1 μm. All pictures are taken from ablation craters made with a stage velocity of 5 mm/s. With energies of: (top,left) 934 nJ, (top,right) 1.20 μJ, (bottom,left) 865 nJ and (bottom,right) 1.33 μJ.

However, the ordering and periodicity in the structures are observed to disappear at lower stage velocities where higher numbers of shots are delivered to the region, as seen in figure 5.27. This observation rules out the formation of ripples due to interference effect. Since the structures should not dissapear as the number of laser shots delivered to the interaction region is changed by changing the stage speed. It is, therefore, thought that the ripples could be due to localized ejection of the material and its subsequent resolidification. Such a process would depend on the number of laser shots vis-a-vis

stage speed. However, it is interesting to note that the porosity of the localized ablated region can controlled by altering the number of laser shots. As the speed decreases, the porosity increases.

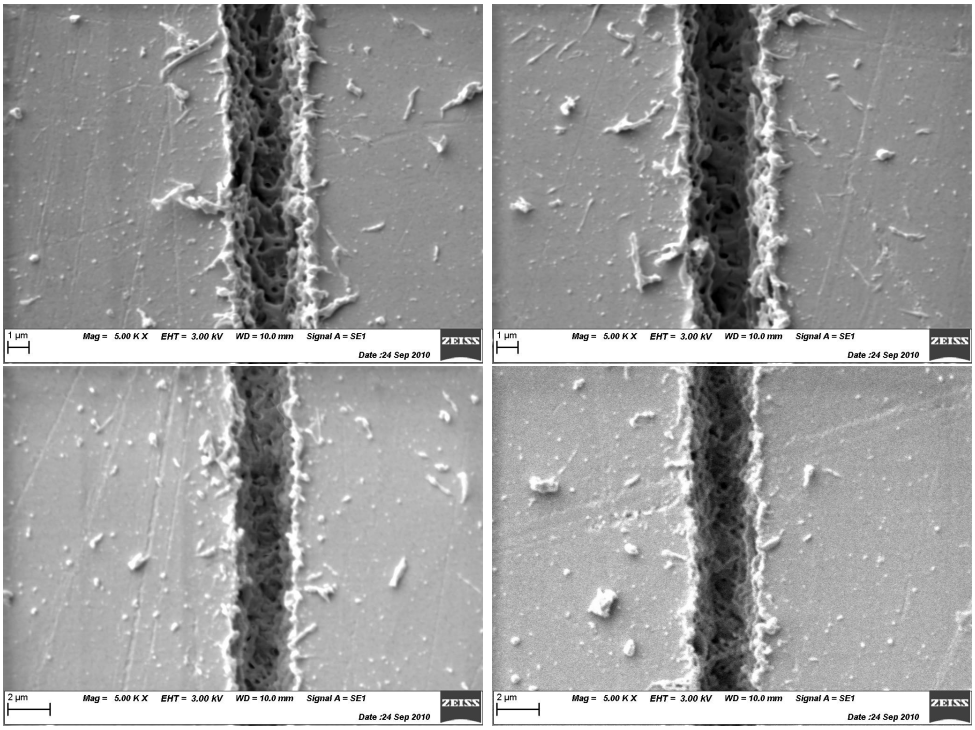

Figure 5.27: Images of the ablation craters made by linearly polarized light rotated to make a 45 ° angle with the motion of the stage. (top) line ablation done with stage velocity of 2.5 mm/s using energies of (left) 1.2 μJ and (right) 1.33 μJ, (bottom) stage velocity of 1 mm/s using energies of (left) 1.2 μJ and (right) 1.33 μJ.

It was also shown that similar structures were observed (see Figure 5.27) in the ablation trails upon using linearly polarized light with an electric field of E (twice the intensity delivered to the interaction region then that delivered in Figures 5.25-26), with a stage velocity of 0.5 mm/s.

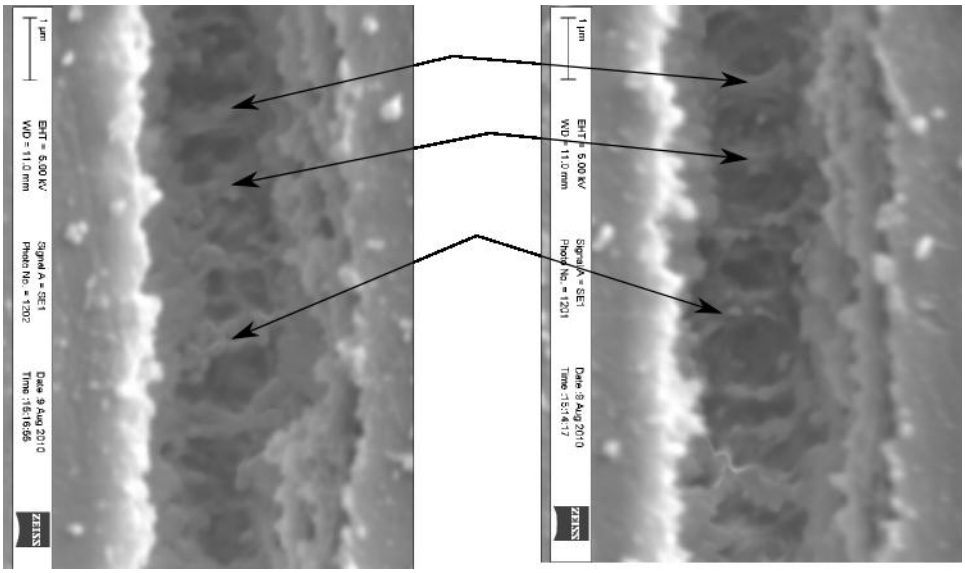

Figure 5.28: Images taken of the ablation trails using linearly polarized light oriented at 45°, energy of 985 nJ and electric field of E. Periodic structures are observed at the bottom of the trails.

5.5 Internal modification of PMMA

The focusing of intense femtosecond pulses inside transparent materials have been known to induce permanent changes within the focused region. One of these changes is the permanent refractive index change of the material within the focus region (interaction volume) [39, 48, 51]. Caused by the creation of a plasma within a confined geometry (observed visually during the experiments) which is followed by a cooldown period and the creation of new chemical bonds. This part of the study is meant to determine the thresholds required for the formation of waveguides within the PMMA sample for a different number of laser shots delivered to the interaction region.

5.5.1 Refractive index change and waveguide creation

The creation of a waveguide within a transparent material can be visualized as artificially implanting a fibre optic-like object within that material. The refractive index change induced by the laser is extremelly small and generally increases after the modification. This difference between the refractive index of the modified region and the surrounding

unaffected regions is ideal for light propagation, meeting the necessary condition for total internal reflection [50]. These changes in the refractive index are energy dependent since they arise from nonlinear interactions. They also exhibit a threshold value beyond which the index value increases rapidly and then saturates.

Threshold values

The experiments were done using the same methods and procedures that were used for surface line ablation with the sole difference being that the light is being focused inside the material instead of at the surface.

The thresholds for the creation of waveguides were obtained by visually inspecting the PMMA samples under a microscope following the experiment, as shown in Figure 5.29.

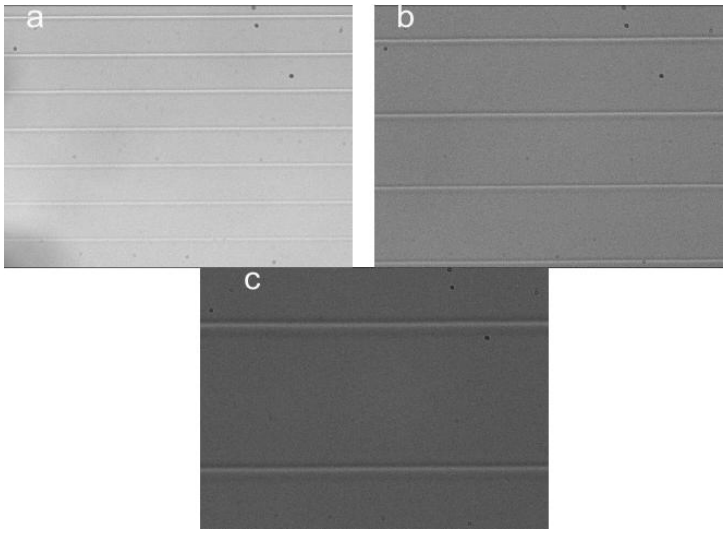

Figure 5.29: Waveguides formed within the PMMA sample. The images were taken with a CCD attached to a microscope using a (a) 10x, (b) 20x and (c) 40x dry objective.

From the threshold values obtained, a graph of energy versus number of shots per micron was plotted.

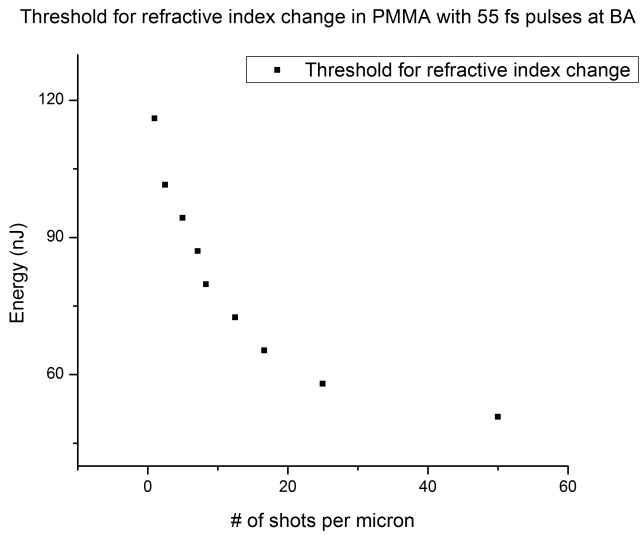

Figure 5.30: Graph of threshold energies for waveguide creation versus number of shots per micron.

From Figure 5.30 it can be observed that the threshold energy required for the formation of waveguides decreases as the number of shots delivered to the interaction region is increased. This decrease in the threshold energy is again due to the shot-to-shot memory effect resulting from the combination of depolymerization and cross-linking within the interaction volume [39, 50]. A saturation is enventually reached where the bandgap energy can no longer be lowered with each following shot and results in a constant energy threshold where the increase in number of laser shots no longer has any effect.

5.5.2 Intraocular lenses

Today, the most common procedure for sight correction and laser eye surgery is LASIK which uses an ultraviolet (UV) excimer laser for the prodecure. The use of a UV source for eye surgery is very troubling due to the long list of known side effects. There is a high probability of irreversible damage to cells by UV light absorption (maximum for DNA and proteins at 200-300 nm). Damage such as: affecting cell division, severe photochemical damage to the eye, heating of the surrounding regions, and photo-cracking of the tissues. Furthermore, UV light in eye surgery, or any other surgery in an aqueous media, causes severe shockwaves and bubble formation.

For this reason, we wished to study light-matter interaction with intraocular lenses (soft-matter) in its native environment using near-IR (800 nm) and IR (1200 nm) wavelengths in order to find new ways of conducting laser eye surgery that are less invasive to the eye thereby greatly reducing the risks.

The intraocular lenses used in these experiments were obtained from Laurier Optical. The chemical composition of the contact lenses is Senofilcon A, composed with the principal monomers: mPDMS, DMA, HEMA, SiGMA, TEGMA, PVP (see glossary for terms).

Surface line ablation of the intraocular lenses

During the experiments, the contact lenses were immersed in a saline solution to maintain their physical integrity. Solution was added throughout the experiment to prevent the drying of the lenses and to maintain a specific thickness of solution on top of the lens to prevent the displacement of the objective's focus along the axial direction. All experiments were done using linearly polarized light with a pulse duration of 55 fs. The light was focused at the sample's surface and the stage moved at a constant velocity.

The study of the ablation process on intraocular lens immersed in the solution was proved to be extremelly difficult and complex. Results obtained from the surface ablation of the intraocular lens have been random at best. From Figure 5.31, it can be clearly seen that the ablation across the sample's surface is not continuous and is instead, randomly composed of ablation craters along the displacement of the objective's focus.

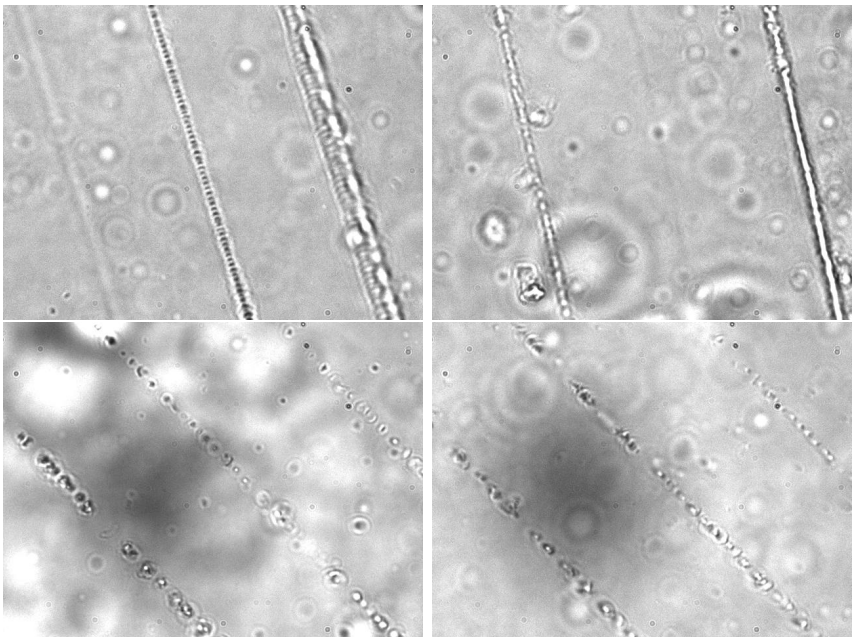

Figure 5.31: Images taken with a CCD camera of the ablation lines made across the contact lens attached to a microscope using a 60x waterdip objective. The lines were done with different stage velocities; (top, left) 5 mm/s; (top, right) 2.5 mm/s; (bottom, left) 1 mm/s; (bottom right) 0.5 mm/s.

On other occasions while using the same parameters, results have shown different events occuring at the surface of the contact lens. It was often observed that the surface of the lens melted (see Figure 5.32) without any sign of ablation.

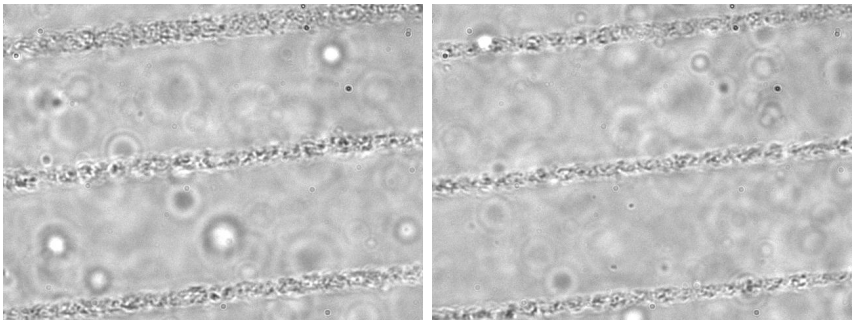

Figure 5.32: Images taken with a CCD camera of the ablation lines made across the contact lens attached to a microscope using a 60x waterdip objective. Melted structures are observed with no sign of any ablation occuring at the surface.

The study of the ablation of an intraocular lens in a saline solution environment has been very complex with no conclusive results. Future experiments should try to understand the breakdown process occuring at the surface. In addition, we will strive to understand the influence of some parameters on the breakdown process such as: cavitation bubble formation and its influence on the incident laser beam and on the sample's surface, cavitation bubble lifetime, displacement of the objective's focus with changing solution depth, turbulence in the solution with the moving stage, change in refractive index of the saline solution with increasing temperature [114], and the expansion of the bubble with each successive shot if its lifetime is longer then the repetition rate of the laser [14, 55, 56, 57] must be carefully studied. Another difficulty has been to accurately find the surface due to the convex shape of the lens.

Chapter 6

Conclusion and Future Work

6.1 Conclusion

This section will summarize the results obtained from the experiments conducted on PMMA and the contact lenses. It will discuss the trends observed and compare the results obtained throughout this part of the research.

The results include the threshold values for the surface ablation and the creation of waveguides inside of PMMA. Two different methods of surface ablation were used: single shot and line ablation.

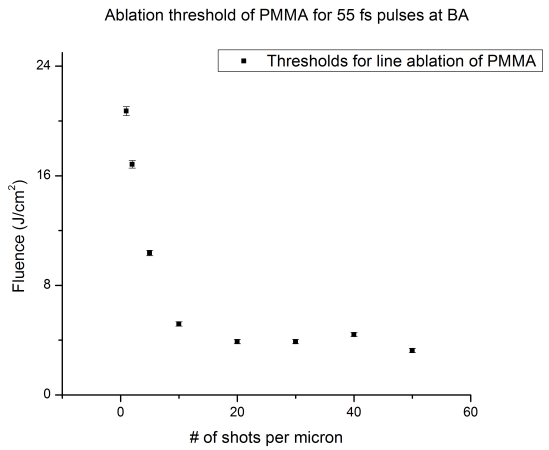

Figure 6.1: Graph of surface line ablation threshold versus number of shots per micron.

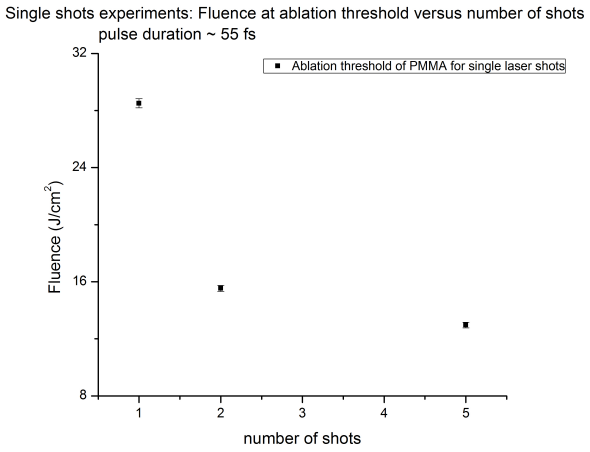

Figure 6.2: Graph of single shot ablation threshold versus number of shots delivered to the region.

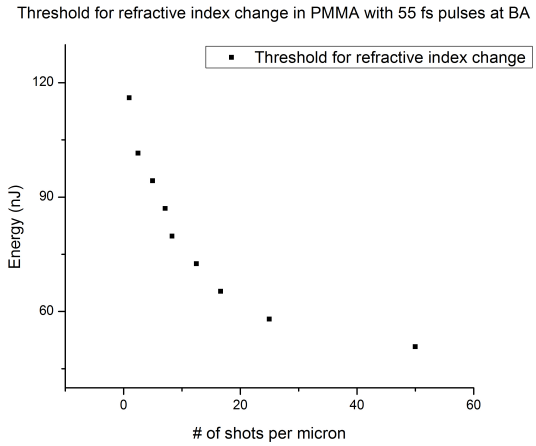

Figure 6.3: Graph of threshold energy versus number of shots per micron (waveguides).

Results obtained for the threshold values have shown a distinctive trend when using high intensities to induce permanent changes to the material. All threshold values were observed to decrease as the number of shots delivered to the region was increased. The decrease in the threshold energy is explained by the shot-to-shot memory induced to the material which lowers the bandgap energy with each successive shot [39]. As shown from the graphs, the lowering of the bandgap is not infinite but eventually reaches a satura-

tion point where the bandgap can no longer be lowered. A constant threshold energy is eventually reached where increasing the number of shots delivered to the region no longer has any effect. These observations are in agreement with theory; all nonlinear interactions with a medium eventually reach a point of saturation.

The analysis of the trails from the surface ablation of PMMA gave interesting results. It was observed that the quality of the ablation trails depended on the orientation of the electric field of linearly polarized light with respect to the motion of the stage. The images show that the damage done from the ablation with a stage velocity of 2.5 mm/s and 2 shots per micron had no significant differences between the trails caused from different orientations. Although as the number of shots delivered to the region was increased, damage to the side of the ablation trails was observed to significantly increase for light oriented differently than from the stage motion. Results show cleaner ablation trails for light oriented parallel to the stage motion. As for the ablation trails from the light oriented at 45° or perpendicular, a pre-dominant wave-pattern damage could be observed to form on the side of the trails (see Figures 5.24-26) which were observed to grow outwards as the number of shots delivered to the region was increased. This observation could indicate a favored direction to the photoionization process along the electric field or a favored direction of the polymers within the bulk.

During the research done on PMMA, the thresholds for single shot ablation and surface line ablation were obtained and compared with each other. The superposition of the thresholds (see Figure 6.4) showed nearly similar values in threshold fluence for the number of shots delivered to the region. As seen from the figure, a slight difference in the threshold values between the two methods was expected and observed. This difference in the threshold values is attributed to the total amount of energy delivered to the region. This comes from the reason that even though the energies delivered to the focal plane are the same, more energy is deposited onto the region when doing line ablation. Compared to single shot ablation, line ablation has its threshold values as a function of the number of shots per micron and not the number of shots delivered to the surface.

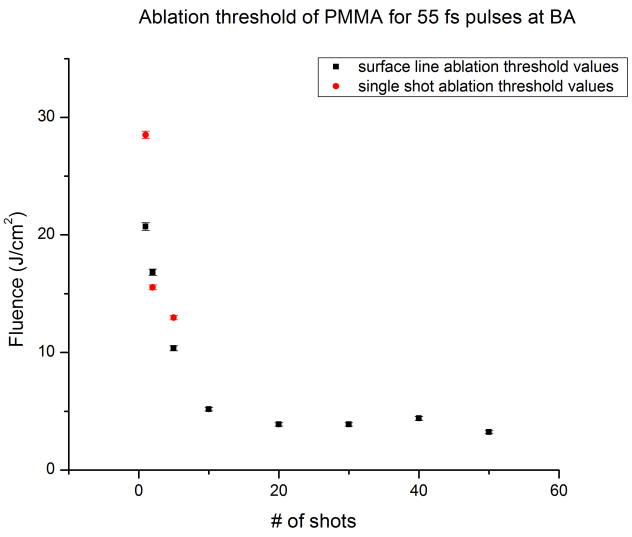

Figure 6.4: Graph of threshold values for single shot and surface line ablation of PMMA versus number of shots delivered to the region

6.2 Future Work

A great amount of data was gathered from the interaction of light with PMMA at 800 nm. More work should be done in investigating the possibility of a preferred direction for photoionization along the electric field of the laser. The data can be obtained by adding more increments in the change of the orientation of the linearly polarized light delivered to the surface. Future work on single shot ablation should be done by finding threshold values for higher numbers of shots delivered to the PMMA surface in order to increase the accuracy of the data. Also, it would be in the best interest of this research to study the structures left in the ablation craters and threshold values using different pulse durations, electric fields, and polarizations. Currently this lab is equipped with an optical parametric amplifier (OPA), capable of producing light at longer wavelengths. Future work should focus on repeating the experiments done throughout this thesis using different laser wavelengths in order to compare it to the results obtained at 800 nm.

Due to time constraints, the nano-structures expected to form within the waveguides from the creation of localized nano-plasma within the bulk [48] were never looked upon. Future experiments will look into cutting the PMMA samples along the direction of

the waveguides or by etching the PMMA samples in order to have access to the nanostructures. Furthermore, work should be done to test the quality of the waveguides made in PMMA samples by sending light through and monitoring the output signal. This test should indicate the best energy and other parameters to be used for the creation of waveguides with the best efficiency. Also, work should be done to look into the quality and efficiency of the waveguides using different light polarizations as well as different beam shapes (eg. using a cylindrical lens to write the waveguide).

The study of the light interaction with contact lenses has proved to be extremely difficult when studying the material as it was immersed in a saline solution. An intermediate step between the study of a hard polymer and a soft polymer immersed in a solution should be approached. One such step would be to study the changes in the breakdown process by immersing a PMMA sample in a saline solution and compare these results with a PMMA sample in air. This should lead to a clear idea of how the immersion medium affects the ablation process.

Future work should concentrate on improving the setup used to study the light interaction with the contact lens. The design of a holder for the lens to ensure that it remains flat throughout the entire experiment would be important. Also, time should be spent on finding new and efficient ways to keep the lens wet in order to maintain its physical integrity without the need to immerse it completely in the saline solution or having to constantly add solution throughout the entire experiment. Adding too much or too little solution can move the focus of the objective off the surface of the lens. A solution would be to design a setup where microfluidic channels could keep the lens wet throughout the experiments.

Appendix A

Glossary of Terms

AFP Actual Focus Position

AR Anti-Reflection

BA Back Aperture

BBO Beta Barium borate

BPAE Bovine Pulmonary Artery Endothelial

CCD Charged-Coupled Device

CM Confocal Microscopy

CW Continuous Wave

DAQ card Data Aquisition card

DMA Dimethylaminoetyl acrylate

FWHM Full Width at Haft Maximum

GDD Group Delay Dispersion

GVD Group Velocity Dispersion

HEMA hydroxyethyl methacrylate

IP Ionizing Potential

IR Infrared

NA Numerical Aperture

ND Neutral Density

NFP Nominal Actual Position

mPDMS methacryloxypropyldimethoxysilane

OPA Optical Parametric Amplifier

PMMA Poly(methyl methacrylate)

PMT Photomultiplier Tube

PSF Point Spread Function

PVP Polyvinylpyrrolidone

SEM Scanning Electron Microscope

SiGMA (Sigma-Aldrich) Poly(methyl methacrylate)

SH Second Harmonic

TEGMA tri-ethylene glycol monomethacrylate

TPM Two-Photon Microscopy

UV Ultra-Violet

Bibliography

[1] A. Einstein, "ber die von der molekularkinetischen Theorie der Wärme geforderte Bewegung von in ruhenden Flüssigkeiten suspendierten Teilchen," *Annalen der Physik*, vol. 322, no. 8, pp. 549–560, 1905.

[2] M. Göppert-Mayer, "ber Elementarakte mit zwei Quantensprüngen," *Annalen der Physik*, vol. 401, no. 3, pp. 273–294, 1931.

[3] T. H. MAIMAN, "Stimulated Optical Radiation in Ruby," *Nature*, vol. 187, no. 4736, pp. 493–494, 1960.

[4] W. Kaiser and C. G. B. Garrett, "Two-Photon Excitation in CaF2: Eu2," *Physical Review Letters*, vol. 7, no. 6, pp. 229–231, 1961.

[5] W. H. Louisell, *Quantum Statistical Properties of Radiation*. Wiley, 1973.

[6] A. Diaspro, *Confocal and Two-photon Microscopy: Foundations*, pp. 39–47. Wiley-Liss, 2002.

[7] D. L. Andrews and P. Allcock, *A quantum electrodynamical foundation for molecular photonics*, pp. 603–643. John Wiley & Sons, second ed., 2001.

[8] H. Sabzyan and M. Vafaee, "Intensity dependence of the H_{2}^{+} ionization rates in Ti:sapphire laser fields above the Coulomb-explosion threshold," *Physical Review A*, vol. 71, pp. 1–6, June 2005.

[9] A. JABOSKI, "Efficiency of Anti-Stokes Fluorescence in Dyes," *Nature*, vol. 131, no. 3319, pp. 839–840, 1933.

[10] C. Soeller and M. B. Cannell, "Two-photon microscopy: imaging in scattering samples and three-dimensionally resolved flash photolysis.," *Microscopy Research and Technique*, vol. 47, no. 3, pp. 182–195, 1999.

[11] C. Xu, R. M. Williams, W. Zipfel, and W. W. Webb, "Multiphoton excitation cross-sections of molecular fluorophores," *Bioimaging*, vol. 4, no. 3, pp. 198–207, 1996.

[12] C. Xu, J. Guild, W. Webb, and W. Denk, "Determination of absolute two-photon excitation cross sections by in situ second-order autocorrelation.," *Optics Letters*, vol. 20, no. 23, p. 2372, 1995.

[13] A. Diaspro, *Confocal and Two-photon Microscopy: Foundations*, pp. 193–233. Wiley-Liss, 2002.

[14] S. Nolte, C. Momma, H. Jacobs, A. Tünnermann, B. N. Chichkov, B. Wellegehausen, and H. Welling, "Ablation of metals by ultrashort laser pulses," *Journal of the Optical Society of America B*, vol. 14, no. 10, p. 2716, 1997.

[15] ANDREWS and DL, "A SIMPLE STATISTICAL TREATMENT OF MULTIPHOTON ABSORPTION," *AMERICAN JOURNAL OF PHYSICS*, vol. 53, no. 10, pp. 1001–1002, 1985.

[16] A. Diaspro, *Confocal and Two-photon Microscopy: Foundations*. Wiley-Liss, 2002.

[17] W. M. McClain and R. A. Harris, *Two-Photon Molecular Spectroscopy in Liquids and Gases*, vol. 3, p. 1. Academic Press, 1977.

[18] L. D. Dickson, "Characteristics of a propagating gaussian beam.," *Applied Optics*, vol. 9, no. 8, pp. 1854–61, 1970.

[19] S. Hell, G. Reiner, C. Cremer, and E. H. K. Stelzer, "Aberrations in confocal fluorescence microscopy induced by mismatches in refractive index," *Handbook of Biological Confocal Microscopy*, vol. 169, no. 3, pp. 391–405, 1993.

[20] M. Born and E. Wolf, *Principles of Optics*, vol. 49. Cambridge University Press, 1999.

[21] M. Gu and C. J. R. Sheppard, "Comparison of three-dimensional imaging properties between two-photon and single-photon fluorescence microscopy," *Journal of Microscopy*, vol. 177, no. 2, pp. 128–137, 1995.

[22] C. Sheppard and M. Gu, "Image formation in two-photon fluorescence microscopy," *OptikStuttgart*, vol. 86, no. 3, pp. 104–106, 1990.

[23] M. Minsky, "Memoir on inventing the confocal microscope," *Scanning*, vol. 10, pp. 128–138, 1988.

[24] M. Minsky, "Microscopy Apparatus," 1961.

[25] T. Wilson and C. Sheppard, *Theory and Practice of Scanning Optical Microscopy*. Academic Press, 1984.

[26] S. Willhelm, B. Grobler, M. Glush, and H. Heinz, *Confocal Laser Scanning Microscopy*. Carl Zeiss: Advanced Imaging Microscopy.

[27] U. Tauer, "Advantages and risks of multiphoton microscopy in physiology.," *Experimental Physiology*, vol. 87, no. 6, pp. 709–714, 2002.

[28] S. M. Potter, "Vital imaging: two photons are better than one.," *Current Biology*, vol. 6, no. 12, pp. 1595–1598, 1996.

[29] P. T. C. So, "Two-photon Fluorescence Light Microscopy," *Encyclopedia of Life Sciences*, pp. 1–5, 2002.

[30] A. K. De and D. Goswami, "Exploring the nature of photo-damage in two-photon excitation by fluorescence intensity modulation.," *Journal of fluorescence*, vol. 19, pp. 381–6, Mar. 2009.

[31] H. G. Cruz and C. Lüscher, "Applications of two-photon microscopy in the neurosciences.," *Frontiers in bioscience a journal and virtual library*, vol. 10, pp. 2263–2278, 2005.

[32] A. C. Bovik, *Handbook of image and video processing*, pp. 1295–1303. Academic Press, 2005.

[33] S.-C. Shen, "Principles and Application, http://abrc.sinica.edu.tw/icm/app_out/main/theorem_F

[34] J. B. Pawley, *Handbook of Biological Confocal Microscopy*. Springer, 2006.

[35] M. E. Dailey, E. Manders, D. R. Soll, and M. Terasaki, "Confocal Microscopy of Living Cells," *Focus*, pp. 381–404, 2006.

[36] A. Diaspro, *Confocal and Two-photon Microscopy: Foundations*, pp. 153–167. Wiley-Liss, 2002.

[37] H. C. Van De Hulst, *Light Scattering by Small Particles*, vol. 41 of *Structure of Matter Series*. Dover, 1957.

[38] L. Keldysh, "Ionization in the field of a strong electromagnetic wave(Multiphonon absorption processes and ionization probability for atoms and solids in strong electromagnetic field)," *Soviet PhysicsJETP*, vol. 20, pp. 1307–1314, 1965.

[39] V. R. Bhardwaj, P. P. Rajeev, P. B. Corkum, and D. M. Rayner, "Strong field ionization inside transparent solids," *Journal of Physics B Atomic Molecular and Optical Physics*, vol. 39, no. 13, pp. S397–S407, 2006.

[40] M. V. Ammosov, N. B. Delone, and V. P. Krainov, "Tunnel ionization of complex atoms and atomic ions in an alternating electromagnetic field," *JETP*, vol. 91, no. 6, pp. 2008–20013, 1986.

[41] R. W. Boyd, *Nonlinear Optics*, vol. 44, ch. 12, pp. 517–518. Academic Press, 2003.

[42] F. H. M. Faisal, *Theory of Multiphoton Ionization*. Physics of Atoms and Molecules, Plenum, 1987.

[43] H. G. Muller and A. Tip, "Multiphoton ionization in strong fields," *Physical Review A*, vol. 30, no. 6, pp. 3039–3050, 1984.

[44] S. Chin, F. Yergeau, and P. Lavigne, "Tunnel ionisation of Xe in an ultra-intense CO2 laser field (1014 W cm-2) with multiple charge creation," *Journal of Physics B: Atomic and Molecular Physics*, vol. 18, p. L213, 1985.

[45] A. Kaiser, B. Rethfeld, M. Vicanek, and G. Simon, "Microscopic processes in dielectrics under irradiation by subpicosecond laser pulses," *Physical Review B*, vol. 61, no. 17, pp. 11437–11450, 2000.

[46] X. Liu, D. Du, and G. Mourou, "Laser ablation and micromachining with ultrashort laser pulses," *IEEE Journal of Quantum Electronics*, vol. 33, no. 10, pp. 1706–1716, 1997.

[47] B. C. Stuart, M. D. Feit, S. Herman, A. M. Rubenchik, B. W. Shore, and M. D. Perry, "Optical ablation by high-power short-pulse lasers," *Journal of the Optical Society of America B*, vol. 13, no. 2, p. 459, 1996.

[48] P. P. Rajeev, M. Gertsvolf, C. Hnatovsky, E. Simova, R. S. Taylor, P. B. Corkum, D. M. Rayner, and V. R. Bhardwaj, "Transient nanoplasmonics inside dielectrics," *Journal of Physics B Atomic Molecular and Optical Physics*, vol. 40, no. 11, pp. S273–S282, 2007.

[49] P. P. Rajeev, M. Gertsvolf, E. Simova, C. Hnatovsky, R. S. Taylor, V. R. Bhardwaj, D. M. Rayner, and P. B. Corkum, "Memory in nonlinear ionization of transparent solids.," *Physical Review Letters*, vol. 97, no. 25, p. 253001, 2006.

[50] D. L. N. Kallepalli, N. R. Desai, and V. R. Soma, "Fabrication and optical characterization of microstructures in poly(methylmethacrylate) and poly(dimethylsiloxane) using femtosecond pulses for photonic and microfluidic applications," *Applied Optics*, vol. 49, no. 13, p. 2475, 2010.

[51] R. FABBRO, J. FOURNIER, P. BALLARD, D. DEVAUX, and J. VIRMONT, "PHYSICAL STUDY OF LASER-PRODUCED PLASMA IN CONFINED GEOMETRY," *Journal of Applied Physics*, vol. 68, no. 2, pp. 775–784, 1990.

[52] J. König, S. Nolte, and A. Tünnermann, "Plasma evolution during metal ablation with ultrashort laser pulses.," *Optics Express*, vol. 13, no. 26, pp. 10597–10607, 2005.

[53] E. G. Gamaly, A. V. Rode, V. T. Tikhonchuk, and B. Luther-Davies, "Ablation of solids by femtosecond lasers: ablation mechanism and ablation thresholds for metals and dielectrics," *Physics of Plasmas*, vol. 9, no. 3, p. 27, 2001.

[54] *Ultra-Short-Pulse Laser Technology and Applications, Lecture 5*, pp. 153–188. No. Lecture 5.

[55] A. Vogel, J. Noack, K. Nahen, D. Theisen, S. Busch, U. Parlitz, D. X. Hammer, G. D. Noojin, B. A. Rockwell, and R. Birngruber, "Energy balance of optical breakdown in water at nanosecond to femtosecond time scales," *Applied Physics B Lasers and Optics*, vol. 68, no. 2, pp. 271–280, 1999.

[56] A. Vogel, S. Busch, and U. Parlitz, "Shock wave emission and cavitation bubble generation by picosecond and nanosecond optical breakdown in water," *Journal of the Acoustical Society of America*, vol. 100, no. 1, p. 148, 1996.

[57] A. Vogel, "Intraocular Nd:YAG Laser Surgery: Light-Tissue Interaction,Damage Range, and Reduction of Collateral Effects," *IEEE J Quantum Electron*, vol. 26, no. 12, pp. 2240–2260, 1990.

[58] P. Barnes and K. Rieckhoff, "LASER INDUCED UNDERWATER SPARKS," *Applied Physics Letters*, vol. 13, no. 8, pp. 1967–1969, 1968.

[59] D. J. Stolarski, J. Hardman, C. M. Bramlette, G. D. Noojin, R. J. Thomas, B. A. Rockwell, and W. P. Roach, "Integrated light spectroscopy of laser induced breakdown in aqueous media," *Library*, vol. 2391, pp. 100–109, 1995.

[60] E. J. Chapyak, "Comparison of numerical simulations and laboratory studies of shock waves and cavitation bubble growth produced by optical breakdown in water," *Proceedings of SPIE*, vol. 2975, pp. 335–342, 1997.

[61] A. Vogel, K. Nahen, D. Theisen, and J. Noack, "Plasma formation in water by picosecond and nanosecond Nd:YAG laser pulses. I. Optical breakdown at threshold and superthreshold irradiance," *IEEE Journal of Selected Topics in Quantum Electronics*, vol. 2, no. 4, pp. 847–860, 1996.

[62] A. Vogel, J. Noack, K. Nahen, D. Theisen, R. Birngruber, D. X. Hammer, G. D. Noojin, and B. A. Rockwell, "Laser-induced breakdown in the eye at pulse durations from 80 ns to 100 fs," in *Applications of Ultrashort-Pulse Lasers in Medicine and Biology* (J. Neev, ed.), vol. 3255, pp. 34–49, SPIE, 1998.

[63] A. Baum, P. J. Scully, W. Perrie, D. Liu, and V. Lucarini, "Mechanisms of femtosecond laser-induced refractive index modification of poly(methyl methacrylate)," *Journal of the Optical Society of America B*, vol. 27, p. 107, Dec. 2009.

[64] W. Denk, J. H. Strickler, and W. W. Webb, "Two-photon laser scanning fluorescence microscopy.," *Science*, vol. 248, no. 4951, pp. 73–76, 1990.

[65] B. Bianco and A. Diaspro, "Analysis of three-dimensional cell imaging obtained with optical microscopy techniques based on defocusing.," *Cell Biophysics*, vol. 15, no. 3, pp. 189–199, 1989.

[66] A. Diaspro, *Confocal and Two-photon Microscopy: Foundations*, pp. 47–53. Wiley-Liss, 2002.

[67] G. J. Brakenhoff, M. Müller, and R. I. Ghauharali, "Analysis of efficiency of two-photon versus single-photon absorption of fluorescence generation in biological objects.," *Journal of Microscopy*, vol. 183, no. Pt 2, pp. 140–144, 1996.

[68] P. T. C. So, C. Dong, B. R. Masters, and K. M. Berland, "Two-photon excitation fluorescence microscopy," *Annual Reviews of Biomedical Engineering*, vol. 02, pp. 399–429, 2000.

[69] A. Diaspro, *Confocal and Two-photon Microscopy: Foundations*, pp. 101–112. Wiley-Liss, 2002.

[70] E. H. K. Stelzer, "Contrast, resolution, pixelation, dynamic range and signal- to-noise ratio: fundamental limits to resolution in uorescence light microscopy," *Microscopy*, vol. 189, no. 1, pp. 15–24, 1998.

[71] E. Hecht, *Optics 4th edition*, p. 472. Addison Wesley, 2001.

[72] A. Diaspro, P. Bianchini, G. Vicidomini, M. Faretta, P. Ramoino, and C. Usai, "BioMedical Engineering OnLine — Full text — Multi-photon excitation microscopy," *Biomedical engineering online*, vol. 5, p. 36, Jan. 2006.

[73] T. Wilson, *The role of the pinhole in cofocal imaging systems*, pp. 167–182. Plenum Press, 1995.

[74] A. Periasamy, P. Skoglund, C. Noakes, and R. Keller, "An Evaluation of Two-Photon Excitation Versus Confocal and Digital Deconvolution Fluorescence Microscopy Imaging in Xenopus Morphogenesis," *Microscopy Research and Technique*, vol. 181, no. August, pp. 172–181, 1999.

[75] F. Helmchen and W. Denk, "Deep tissue two-photon microscopy," *Nature Methods*, vol. 2, no. 12, 2005.

[76] P. T. So, C. Y. Dong, B. R. Masters, and K. M. Berland, "Two-photon excitation fluorescence microscopy.," *Annual Review of Biomedical Engineering*, vol. 2, no. 1, pp. 399–429, 2000.

[77] I. J. Cox, C. J. Sheppard, and T. Wilson, "Improvement in resolution by nearly confocal microscopy.," *Applied Optics*, vol. 21, no. 5, pp. 778–781, 1982.

[78] M. B. Ericson, C. Simonsson, S. Guldbrand, C. Ljungblad, J. Paoli, and M. Smedh, "Two-photon laser-scanning fluorescence microscopy applied for studies of human skin.," *Journal of biophotonics*, vol. 1, no. 4, pp. 320–330, 2008.

[79] M. B. Ericson, "Deep tissue imaging of cell structures," *Biomedical Optics & Medical Imaging*, pp. 2–3, 2007.

[80] H. Jacobsen, P. Hanninen, E. Soini, and S. Hell, "Refractive Index Induced Aberrations in Two-Photon Confocal Fluorescence Microscopy," *Journal of Microscopy*, vol. 176, no. 3, p. 226230, 1994.

[81] M. J. Booth, M. A. A. Neil, and T. Wilson, "Aberration correction for confocal imaging in refractive-index-mismatched media," *Journal of Microscopy*, vol. 192, no. 2, pp. 90–98, 1998.

[82] C. J. De Grauw, J. M. Vroom, H. T. Van Der Voort, and H. C. Gerritsen, "Imaging properties in two-photon excitation microscopy and effects of refractive-index mismatch in thick specimens.," *Applied Optics*, vol. 38, no. 28, pp. 5995–6003, 1999.

[83] R. W. Boyd, *Nonlinear Optics*, vol. 44, ch. 7, pp. 356–363. Academic Press, 2003.

[84] J. C. Diels and W. Rudolph, *Ultrashort Laser Pulse Phenomena*, vol. 36, pp. 30–38. Academic Press, 2006.

[85] D. Anderson, "Lens on Leeuwenhoek: How he made his tiny lenses, http://lensonleeuwenhoek.net/lenses.htm."

[86] A. Powazek, "2008 November Digital Daily Dose."

[87] V. E. Centonze and J. G. White, "Multiphoton excitation provides optical sections from deeper within scattering specimens than confocal imaging.," *Biophysical Journal*, vol. 75, no. 4, pp. 2015–2024, 1998.

[88] G. H. Patterson and D. W. Piston, "Photobleaching in two-photon excitation microscopy.," *Biophysical Journal*, vol. 78, no. 4, pp. 2159–2162, 2000.

[89] S. T. Flock, S. L. Jacques, B. C. Wilson, W. M. Star, and M. J. Van Gemert, "Optical properties of Intralipid: a phantom medium for light propagation studies.," *Lasers in Surgery and Medicine*, vol. 12, no. 5, pp. 510–519, 1992.

[90] A. Hopt and E. Neher, "Highly nonlinear photodamage in two-photon fluorescence microscopy.," *Biophysical Journal*, vol. 80, no. 4, pp. 2029–2036, 2001.

[91] K. König, T. W. Becker, P. Fischer, I. Riemann, and K.-J. Halbhuber, "Pulse-length dependence of cellular response to intense near-infrared laser pulses in multiphoton microscopes," *Optics Letters*, vol. 24, no. 2, pp. 113–115, 1999.

[92] K. König, H. Liang, M. W. Berns, and B. J. Tromberg, "Cell damage by near-IR microbeams.," 1995.

[93] K. König, H. Liang, M. W. Berns, and B. J. Tromberg, "Cell damage in near-infrared multimode optical traps as a result of multiphoton absorption.," *Optics Letters*, vol. 21, no. 14, pp. 1090–1092, 1996.

[94] K. König, P. T. So, W. W. Mantulin, and E. Gratton, "Cellular response to near-infrared femtosecond laser pulses in two-photon microscopes.," *Optics Letters*, vol. 22, no. 2, pp. 135–136, 1997.

[95] H. J. Koester, D. Baur, R. Uhl, and S. W. Hell, "Ca2+ Fluorescence Imaging with Pico- and Femtosecond Two-Photon Excitation: Signal and Photodamage," *Biophysical Journal*, vol. 77, no. 4, pp. 2226–2236, 1999.

[96] Y. Miyamoto, Y. Umebayashi, and T. Nishisaka, "Comparison of phototoxicity mechanism between pulsed and continuous wave irradiation in photodynamic therapy.," *Journal of photochemistry and photobiology. B, Biology*, vol. 53, no. 1-3, pp. 53–9, 1999.

[97] P. S. Tsai, N. Nishimura, E. J. Yoder, A. White, E. Dolnick, and D. Kleinfeld, *Principles, design and construction of a two photon scanning microscope for in vitro and in vivo studies.*, ch. 6, pp. 113–171. CRC Press, 2002.

[98] Q.-T. Nguyen, P. S. Tsai, and D. Kleinfeld, "MPScope: a versatile software suite for multiphoton microscopy.," *Journal of Neuroscience Methods*, vol. 156, no. 1-2, pp. 351–359, 2006.

[99] T. A. Pologruto, B. L. Sabatini, and K. Svoboda, "ScanImage: Flexible software for operating laser scanning microscopes," *BioMedical Engineering Online*, vol. 2, no. 1, p. 13, 2003.

[100] N. J. Durr, T. Larson, D. K. Smith, B. A. Korgel, K. Sokolov, and A. Ben-Yakar, "Two-photon luminescence imaging of cancer cells using molecularly targeted gold nanorods.," *Nano Letters*, vol. 7, no. 4, pp. 941–945, 2007.

[101] S. Inoué and K. R. Spring, *Video Microscopy : The Fundamentals (The Language of Science)*. Springer, 1997.

[102] J. WATERS, "The Principles of Clinical Cytogenetics," *Journal of Clinical Pathology*, vol. 54, no. 3, pp. 255–256, 2005.

[103] E. Stelzer, "Nonlinear absorption extends confocal fluorescence microscopy into the ultra-violet regime and confines the illumination volume," *Optics Communications*, vol. 104, no. 4-6, pp. 223–228, 1994.

[104] W. Denk, "Two-photon excitation in functional biological imaging," *J Biomed Optics*, vol. 1, no. 3, pp. 296–304, 1996.

[105] J. C. Diels and W. Rudolph, *Ultrashort Laser Pulse Phenomena*, vol. 36. Academic Press, 2006.

[106] G. Ghosh, "Sellmeier coefficients and dispersion of thermo-optic coefficients for some optical glasses.," *Applied Optics*, vol. 36, no. 7, pp. 1540–1546, 1997.

[107] R. Paschotta, *Encyclopedia of Laser Physics and Technology*. Wiley-VCH, 2008.

[108] G. J. R. Sheppard and H. J. Matthews, "Imaging in high-aperture optical systems," *Journal of the Optical Society of America A*, vol. 4, no. 8, pp. 1354–1360, 1987.

[109] "Reference for Acrylic glass - Search.com, http://www.search.com/reference/Acrylic_glass."

[110] V. Raja, A. K. Sarma, and V. V. R. N. Rao, "Optical properties of pure and doped PMMA-CO-P4VPNO polymer films," *Materials Letters*, vol. 57, pp. 4678 – 4683, 2003.

[111] S. Baudach, J. Bonse, J. Kruger, and W. Kautek, "Ultrashort pulse laser ablation of polycarbonate and polymethylmethacrylate," *Applied Surface Science*, pp. 3–8, 2000.

[112] J. Jandeleit, G. Urbasch, H. D. Hoffmann, H.-G. Treusch, and E. W. Kreutz, "Picosecond laser ablation of thin copper films," *Applied Physics A: Materials Science & Processing*, vol. 63, no. 2, pp. 117–121–121, 1996.

[113] V. Bhardwaj, E. Simova, P. Rajeev, C. Hnatovsky, R. Taylor, D. Rayner, and P. Corkum, "Optically Produced Arrays of Planar Nanostructures inside Fused Silica," *Physical Review Letters*, vol. 96, pp. 1–4, Feb. 2006.

[114] K. M. Aly and E. Esmail, "Refractive index of salt water: effect of temperature," *Optical Materials*, vol. 2, pp. 195–199, 1993.